Univerzita Karlova v Praze

Matematicko-fyzikální fakulta

DIPLOMOVÁ PRÁCE

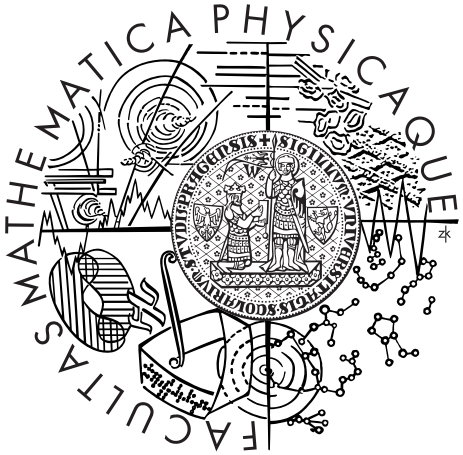

Michal Vraštil

Určování parametrů temné energie a modifikované gravitace v rámci projektu LSST

Astronomický ústav Univerzity Karlovy

Vedoucí diplomové práce:	RNDr. Michael Prouza, Ph.D.
Studijní program:	Fyzika
Studijní obor:	Teoretická fyzika

Praha 2015

Charles University in Prague
Faculty of Mathematics and Physics

MASTER THESIS

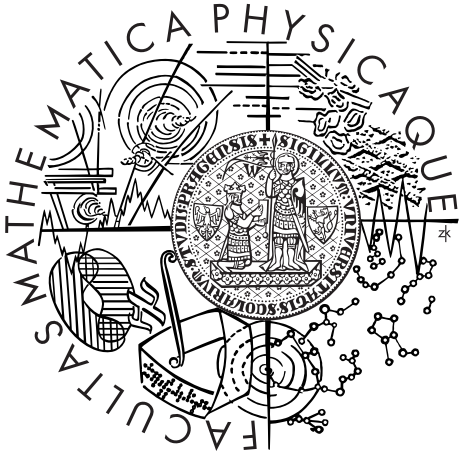

Michal Vraštil

Determination of parameters of dark energy and modified gravity in the LSST project

Astronomical Institute of Charles University

Supervisor of the master thesis:	RNDr. Michael Prouza, Ph.D.
Study programme:	Physics
Specialization:	Theoretical Physics

Prague 2015

I would like to start with thanking my supervisor Michael Prouza, for introducing me to the LSST Project and for his help and support in getting involved in activities in DESC. I also want to thank Salman Habib who stood at the beginning of our project and who introduced me to the exciting field of the chameleon gravity. My great thank belongs to Amol Upadhye who gave me valuable advices and helped me overcome many difficulties regarding the chameleon field. And last but not least I would like to thank my family and friends for their support during studies and that they made this time very pleasant.

I declare that I carried out this master thesis independently, and only with the cited sources, literature and other professional sources.

I understand that my work relates to the rights and obligations under the Act No. 121/2000 Coll., the Copyright Act, as amended, in particular the fact that the Charles University in Prague has the right to conclude a license agreement on the use of this work as a school work pursuant to Section 60 paragraph 1 of the Copyright Act.

In Prague 15/07/2015 .....

Název práce: Určování parametrů temné energie a modifikované gravitace v rámci projektu LSST

Autor: Michal Vraštil

Ústav: Astronomický ústav UK

Vedoucí diplomové práce: RNDr. Michael Prouza, Ph.D., Fyzikální ústav AV ČR

Abstrakt: Temná energie tvořící přibližně 70% hmoty vesmíru zůstává jednou z největších záhad moderní fyziky. K pochopení její podstaty jsou potřeba přesná kosmologická měření. Jedním z projektů zkoumající tuto exotickou formu hmoty bude i Large Synoptic Survey Telescope, který pomůže potvrdit či vyvrátit standardní kosmologický model (ΛCDM). Pro úspěch projektu je potřeba prozkoumat různé teorie temné energie. Jednou z alternativních teorií vysvětlujících urychlenou expanzi vesmíru je tzv. chameleoní gravitace. Chameleon je nové skalární pole s hmotou závisející na okolní hustotě. V hustých prostředích jako je například Sluneční soustava získává pole velkou hmotu a propaguje se pouze na malých vzdálenostech díky čemuž může uniknout standardním testům gravitace. V práci mimo jiné studujeme chování chameleoního pole v okolí hvězd a v galaxiích. Ukazujeme také za jakých okolností je toto pole možné detekovat pomocí spektroskopických měření a slabého čočkování.

Klíčová slova: LSST, DESC, temná energie, modifikovaná gravitace, chameleonní gravitace, simulace, kosmologie

Title: Determination of parameters of dark energy and modified gravity in the LSST project

Author: Michal Vraštil

Department: Astronomical Institute of Charles University

Supervisor: RNDr. Michael Prouza, Ph.D., Institute of Physics CAS

Abstract: Dark energy constitutes roughly 70% of energy density of the Universe and remains one of the greatest mysteries of modern physics. In order to properly undestand its nature we need precise cosmological measurements. One of projects exploring this exotic form of a matter will be the Large Synoptic Survey Telescope which will help confirm or disprove the standard comoslogical model (ΛCDM). For success of the project, various theories of dark energy need to be explored. One of alternative theories explaining accelerated expansion of the Universe is the so called chameleon gravity. The chameleon is a new scalar field with a mass depending on surrounding density. In dense environments such as the Solar system the field acquires large mass and propagates only over small distances and can pass standard tests of gravity. In the thesis we study behavior of the chameleon field near stars and in galaxies. We show on which circumstances this field can be detected through spectroscopic and weak lensing measurements.

Keywords: LSST, DESC, dark energy, modified gravity, chameleon gravity, simulation, cosmology

Contents

1 Introduction **3**

2 Surveys for Constraining Dark Energy **5**
2.1 Large Synoptic Survey Telescope 5
2.1.1 Overview of LSST System Design 5
2.1.2 Survey requirements 13
2.1.3 Dark Energy Science Collaboration 19
2.1.4 Cosmological Probes of Dark Energy 20
2.2 Euclid mission 24
2.2.1 Overview of Euclid System Design 25
2.2.2 Survey Requirements 27
2.2.3 Science Goals 28
2.2.4 Additional Cosmological Probes 29
2.2.5 Comparison and Synergy with LSST 30
2.3 Other Surveys 31
2.3.1 Baryon Oscillation Spectroscopic Survey 31
2.3.2 Dark Energy Survey 32
2.3.3 Wide-Field Infrared Survey Telescope 32

3 Modified Gravity and Dark Energy **34**
3.1 Problems with Cosmological Constant 34
3.2 Beyond ΛCDM 36
3.2.1 Jordan vs. Einstein Frame 38
3.2.2 Screening Mechanisms 39
3.3 Quintessence 40
3.3.1 Thawing or Freezing 41
3.3.2 Tracker Solutions 41
3.4 K-essence 42
3.4.1 Attractor Solutions 43
3.5 Coupled Dark Energy 44
3.6 Chameleon Gravity 45
3.6.1 Chameleon Force 47
3.6.2 Chameleon mechanism 47
3.6.3 Chameleon Profile 48
3.7 Unified Dark Energy and Dark Matter 51
3.7.1 Generalized Chaplygin Gas Model 51
3.7.2 K-essence 52
3.8 $f(R)$ Gravity 53
3.9 Other Models of Modified Gravity 55
3.9.1 Gauss-Bonnet Dark Energy Models 55
3.9.2 Braneworld Models 55
3.9.3 Massive Gravity 56
3.9.4 Acceleration without Dark Energy 57
3.10 Summary 58

4 Numerical Solutions to Chameleon Field **59**
4.1 Hu-Sawicki $f(R)$ Models . . . 59
4.2 Numerical Solutions . . . 61
4.2.1 Runge-Kutta Method with Adaptive Stepsize . . . 62
4.2.2 Shooting Method . . . 63
4.3 Planar Slab in Vacuum . . . 64
4.3.1 Configuration . . . 64
4.3.2 Numerical Results . . . 65
4.4 Stars . . . 67
4.4.1 Expected Behavior . . . 68
4.4.2 Boundary Conditions . . . 69
4.4.3 Numerical Results . . . 70
4.5 NFW Halo . . . 72
4.5.1 Expected Behavior . . . 72
4.5.2 Boundary Condition . . . 73
4.5.3 Numerical Results . . . 74
4.6 N-Body Simulations . . . 78
4.6.1 Introduction . . . 78
4.6.2 Force computing . . . 79
4.6.3 Mesh Force Calculation . . . 82
4.6.4 Particle-Particle Particle-Mesh Algorithm . . . 83
4.6.5 Solution to the Chameleon Field . . . 83
4.7 Discussion and Outlook . . . 85

5 Conclusion **87**

A Standard Cosmological Model **89**
A.1 Introduction . . . 89
A.1.1 Assumptions . . . 89
A.1.2 FLRW metric . . . 90
A.2 Perturbed Universe . . . 91
A.2.1 Newtonian Gauge . . . 91
A.2.2 Kinematics . . . 92
A.3 Methods to Measure the Potentials . . . 93
A.3.1 Growth of Structure . . . 94
A.3.2 Gravitational Lensing . . . 94
A.3.3 Current Limits . . . 95
A.4 Action Principle . . . 95

B C++ Implementation **98**
B.1 Runge-Kutta Method with Adaptive Stepsize . . . 98
B.2 Shooting Method . . . 101
B.3 Planar Slab . . . 103
B.4 Stars . . . 106
B.5 NFW Halo . . . 111
B.6 N-body simulations . . . 113

Bibliography **120**

1. Introduction

Since twentieth century, astronomers have accumulated conclusive evidence that the matter in the Universe is mostly non-baryonic and the Universe‘s expansion is accelerating [3]. Within the framework of the standard cosmological model this implies that roughly 70% of the Universe is composed of a dark energy, whereas 25% is in a form of a dark matter, leaving only 5% in a form of standard matter. Dark energy ranks as one of the most important discoveries in cosmology, with profound implications for astronomy and fundamental physics. Many experiments were, and are trying to discover the nature of these dark sectors of the Universe while other projects are planned for the future.

The Large Synoptic Survey Telescope (LSST) is a ground-based telescope being built in northern Chile [77]. Thanks to a large aperture, wide field survey telescope and 3200 Megapixel camera it will image faint astronomical objects across the sky. The LSST will rapidly scan the sky, charting objects that change or move: from exploding supernovae to potentially hazardous near-Earth asteroids. The LSST will produce very deep survey and its images will trace billions of remote galaxies, providing multiple probes of the mysterious dark matter and dark energy.

ESA‘s Euclid mission is a high-precision space mission designed to map the geometry of the dark Universe [75]. Its primary goal is to place high accuracy constraints on dark energy, dark matter, gravity and cosmic initial conditions. By measuring shapes and redshifts of galaxies and clusters of galaxies up to ten billion years ago, Euclid will cover the entire period over which dark energy played a significant role.

Chapter 2 describes current and future dark energy surveys. We focus especially on the LSST Project. We describe the system design (telescope and camera design, survey strategies or data management), survey requirements for meeting its objectives and various probes of dark energy, which will be used. Some basic information about the Dark Energy Science Collaboration (DESC) are presented [40]. Similar information about the Euclid, i.e. the system design, science goals and its requirements and Euclid‘s probes of dark energy, is also described here. Basic information about other surveys are presented at the end of the chapter.

For success of these surveys, dark energy theories need to be explored – both analytical solutions and numerical simulations. In Chapter 3 we explain currently known problems with the cosmological constant and why it is worth probing alternatives to General Relativity (GR). We present the most studied alternative theories such as extra scalar fields (quintessence [27], k-essence [13]) or $f(R)$ theories [111]. Special attention is given to chameleon gravities [118] which are of our main interest in this work.

We study the chameleon field in the context of Hu-Sawicki $f(R)$ models [66] and present our new results in Chapter 4. Here we present chameleon behavior for non-standard potentials that are not of the usual runaway form which are in most existing chameleon models. We are interested mainly in numerical solutions as the analytical solutions are rare in nature. We examine the behavior of the chameleon field inside and near a surface of stars in the non-linear, but not so deeply screened regime. This regime is not well studied in the literature even

Symbol	Description
c	Speed of light; $c = 1$
$\hbar$	Reduced Planck constant; $\hbar = 1$
G	Bare gravitational constant; $G = 6.71 \cdot 10^{-57}$ (eV)$^{-2}$
M_{pl}	Reduced Planck mass; $M_{pl} \equiv (8\pi G)^{-1/2} = 2.44 \cdot 10^{27}$ eV
Λ	Cosmological constant; $\Lambda = 1.41 \cdot 10^{-120}\ M_{pl}^2$
a	Scale factor; $a_0 \equiv 1$
z	Redshift; $1 + z = a^{-1}$
H	Hubble parameter; $H \equiv \dot{a}/a$; $H_0 = 5.92 \cdot 10^{-61}\ M_{pl}$
h	Dimensionless Hubble parameter; $H \equiv h \times 100$ km$\cdot$ s^{-1} Mpc^{-1}
w	Equation of state parameter; $w \equiv p/\rho$
c_s	Sound speed; $c_s^2 \equiv \mathrm{d}p/\mathrm{d}\rho$
∂	Partial derivative
$\omega_{,X}$	Partial derivative with respect to the quantity X
∇	Covariant derivative
$\Box$	d'Alembertian; $\Box \equiv \nabla^2$
Δ	Laplace operator; $\Delta \equiv \partial_i \partial^i$

Table 1.1: List of symbols. When enumerating constants a value in the natural units is specified.

for standard potentials as analytical solutions do not exist here and experiments usually take place outside the body. But understanding this regime inside the body is key in our next task where we study the behavior of the chameleon field in galaxies described by the NFW halo. We predict a change of the effective mass distribution and a way to detect this effect through combine probes of weak lensing and spectroscopic measurements of satellites of galaxies.

Some basics of the standard cosmological model are described in Appendix A – fundamental principles, description of the FLRW metric and its kinematics, and an introduction into the perturbation theory on the FLRW metric. The action principle and its application to the modified gravity theories is also described here. In Appendix B we then present important parts of the code that has been used in numerical computation in Chapter 4.

Units and conventions

Throughout this work we use natural units such that $c = \hbar = 1$, where c is the speed of light and $\hbar$ is the reduced Planck constant. Used symbols are summarized in Table 1.1. The metric with signature $(-,+,+,+)$ is used. We also use the Einstein summation convention. Unless stated otherwise Greek indices run from 0 to 3, whereas Latin indices run from 1 to 3.

For various combinations of covariant derivatives we use following notation

$$\begin{aligned}
\Box\phi \equiv& \nabla_\mu \nabla^\mu \phi \\
(\nabla\phi)^2 \equiv& (\nabla_\mu \phi)^2 \equiv (\nabla_\mu \phi)(\nabla^\mu \phi) \\
(\nabla\nabla\phi)^2 \equiv& (\nabla_\mu \nabla_\nu \phi)^2 \equiv (\nabla_\mu \nabla^\nu \phi)(\nabla_\nu \nabla^\mu \phi) \\
(\nabla\nabla\phi)^3 \equiv& (\nabla_\mu \nabla_\nu \phi)^3 \equiv (\nabla_\mu \nabla^\nu \phi)(\nabla_\nu \nabla^\rho \phi)(\nabla_\rho \nabla^\mu \phi)
\end{aligned}$$

Similar relations hold for partial derivatives ∂.

2. Surveys for Constraining Dark Energy

In this chapter we describe various dark energy surveys. As the Institute of Physics is an affiliate member of the LSST and the supervisor of the thesis is a full member of the DESC, while the author is an associate member, our description of surveys focus mainly on the LSST. We describe the system design, survey requirements and various probes of dark energy. Next we present similar information about the Euclid as the next mission with great potential of discovering the nature of dark energy. At the end of the chapter we briefly mention several other dark energy surveys – Baryon Oscillation Spectroscopic Survey (BOSS), Dark Energy Survey (DES), and Wide-Field Infrared Survey Telescope (WFIRST).

2.1 Large Synoptic Survey Telescope

The Large Synoptic Survey Telescope (LSST) is a ground-based telescope being built in northern Chile on the Cerro Pachón mountain. The system will produce a 6-band (300 – 1100 nm) wide-field deep astronomical survey over 20,000 deg^2 of the southern sky. Combining the wide field of view with short exposures, the LSST will take more than 800 images each night and cover the whole observable sky twice each week. Each patch of the sky will be visited about 1000 times during ten years. The LSST will provide an unprecedented depth (single-visit 24.5 mag, co-added 27.5 mag) and unique details of the Universe while producing 30 terabytes of data nightly. This data will be used for locating dark matter and to characterize the properties of the dark energy. Other major tasks for the LSST will be detecting and tracking potentially hazardous asteroids or studying the structure of the Milky Way. The project is in the construction phase and will begin regular survey operations by 2022 (the LSST's timeline in Figure 2.1). For overview of the LSST design and science drivers see e.g. [69].

2.1.1 Overview of LSST System Design

The current baseline design allows to obtain sequential images covering over half the sky every three nights. This design involves a 3-mirror system with an 8.4-m primary mirror, which feeds three refractive correcting elements inside a camera, thus providing a 10 deg^2 field of view sampled by a 3.2 Gigapixel focal plane array. The important characteristic that determines the speed at which a system can survey the sky is called étendue (or grasp). It is the product of its primary mirror area (in square meters) and the area of its field of view (in square degrees). The total effective system étendue for LSST will be 319 m^{2}deg^2, which is more than an order of magnitude larger than that of any existing facility.

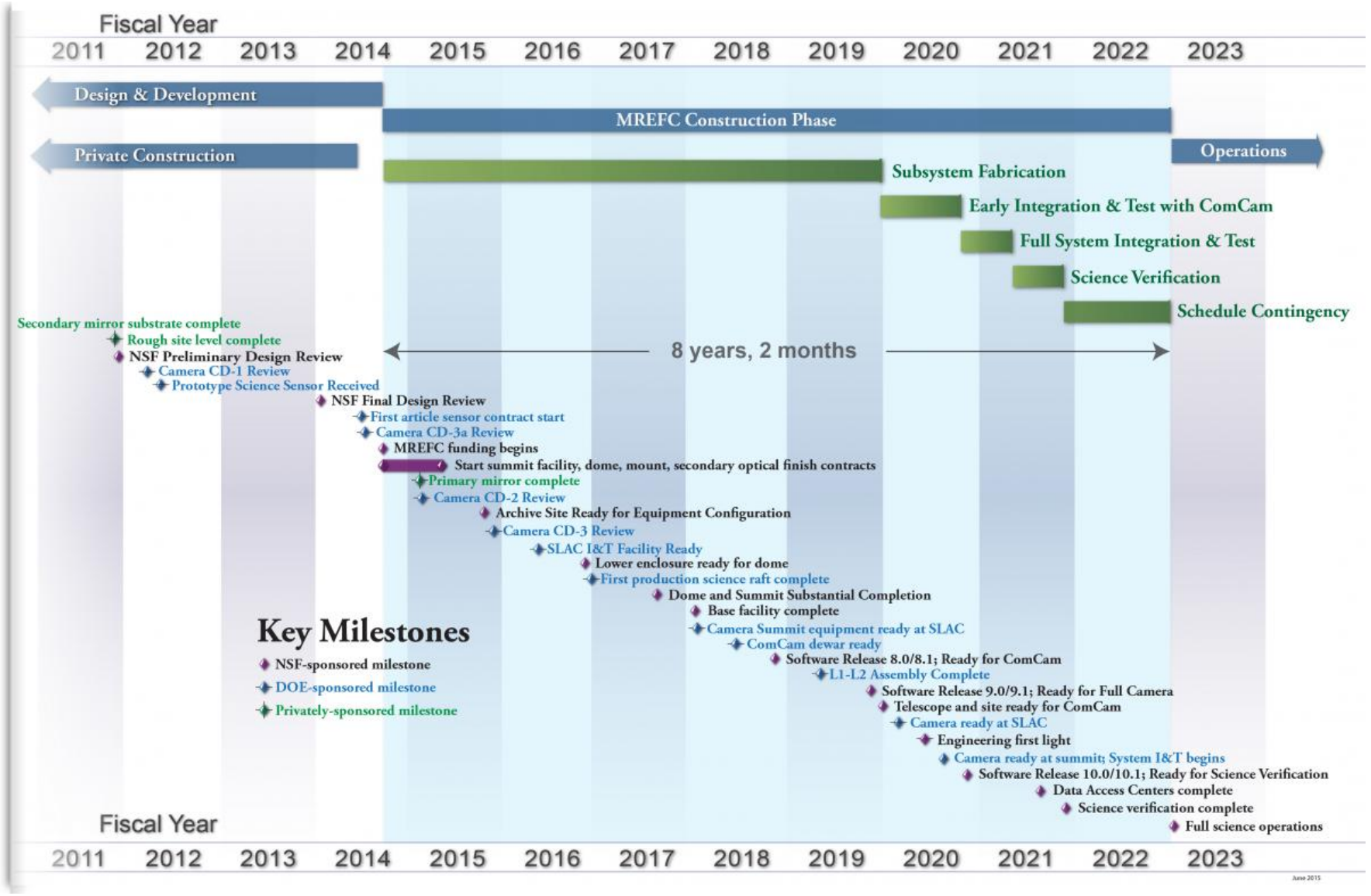

Figure 2.1: The LSST Project Schedule (Last Update: June 2015). From [78].

The basic characteristics of the LSST observing system follow directly from science programs described in § 2.1.2. The location of the telescope should be a site with a very high percentage of usable nights which are distributed uniformly as much as possible throughout the year. The telescope must have a wide field of view in order to obtain several hundred images of each area of the sky. The aperture must be large in order to achieve the sensitivity required to observe faint objects. The wavelength coverage must be broad in order to derive photometric redshifts and to characterize ages and metallicities of stellar populations. Terabytes of data must be obtained every observing night and reduced in near-real time in order to keep pace with the data flow and to send out alerts within a minute or so after detections of interesting brightness changes. The raw images must be converted to well-calibrated data products that can be used by a broad community.

Observatory site

The LSST will be constructed on El Peñón Peak (Figure 2.2) of Cerro Pachón in the northern Chilean Andes. This site was chosen after an extensive study comparing seeing conditions, cloud cover and other weather patterns, and infrastructure issues at a variety of potential candidate sites around the world. Cerro Pachón is located ten kilometers away from Cerro Tololo Inter-American Observatory (CTIO) for which over ten years of detailed weather data have been accumulated, and thus confirmed excellent atmospheric conditions with more than 80% of the nights usable. The expected mean delivered image quality is 0.67″ in g-band as measured by differential image motion monitoring (DIMM) on Cerro Tololo (Figure 2.3). The excellent image quality have been confirmed also by nearby 8.2-m diameter Gemini-South and 4.3-m diameter Southern Astrophysical Research (SOAR) telescopes. In addition, LSST will benefit from the extensive infrastructure that has been created on Cerro Pachón and La Serena to support these other facilities.

The LSST Observatory as a whole will be distributed over four sites: the Summit Facility on El Peñón, the Base Facility, the Archive Center, and the Data Centers. The Base Facility will be at the AURA compound in the town of La Serena, 57 km away from the mountain. The Archive Center will be at the National Center for Supercomputing Applications (NCSA) on the campus of the University of Illinois at Urbana-Champaign. One of the two Data Centers will be located with the Archive Center at NCSA and the other one at the Base Facility in La Serena. All these facilities will be connected via dedicated high-bandwidth fiber optic links.

Telescope

The LSST telescope consists of three aspheric mirrors – an 8.4-m primary M1, a 3.4-m convex secondary M2 (the largest convex mirror ever made), and a 5.0-m tertiary M3 (Figure 2.4). The primary mirror is highly annular having an outer clear aperture of 8.36 m and an inner diameter of 5.12 m, giving an effective collecting area of a 6.67-m filled aperture. The camera body and its associated readout electronics are located in the 1.8-m diameter hole in the secondary mirror. The hole in the tertiary mirror is used to mount equipment for the maintenance of

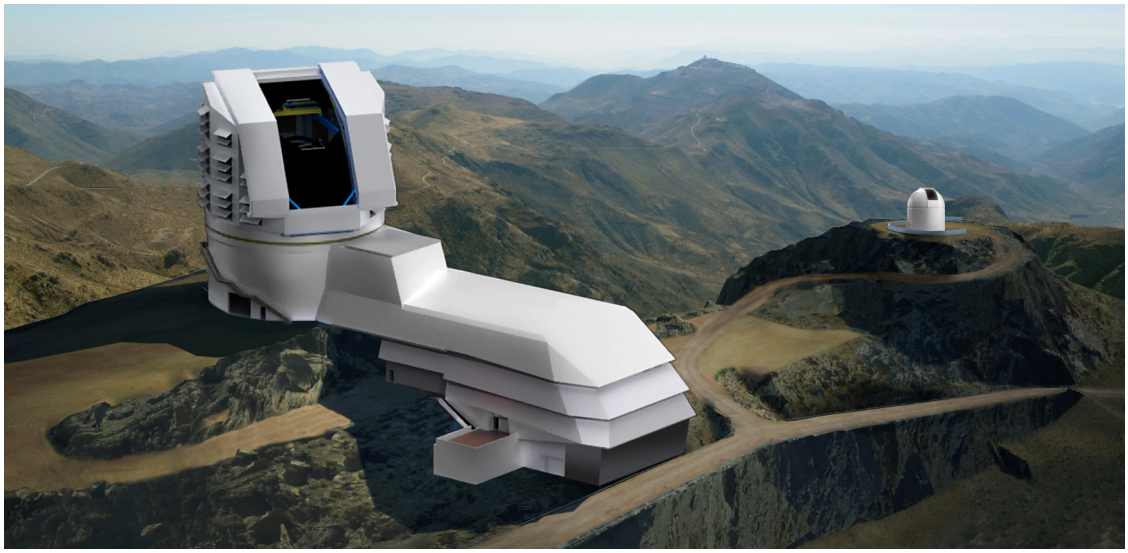

Figure 2.2: Two renderings combine to create this image of the LSST summit facility and Calypso, the small adjacent atmospheric telescope, atop Cerro Pachón in Chile. From [78].

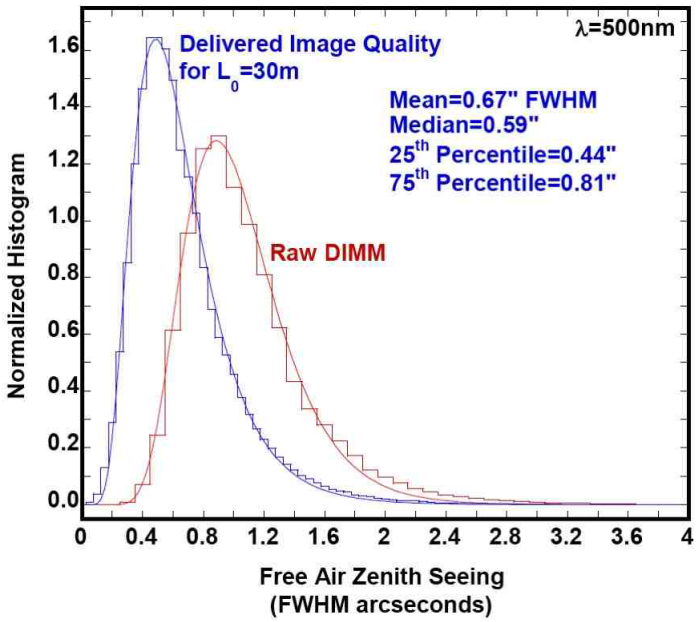

Figure 2.3: The distribution of "seeing" (FWHM of the image of a point source) at 500 nm based on ten years of measurements from CTIO (10 km from the LSST site). The red curve shows results from a DIMM, while the blue curve shows the delivered image quality. The mean is 0.67″, and the median is 0.59″. From [77].

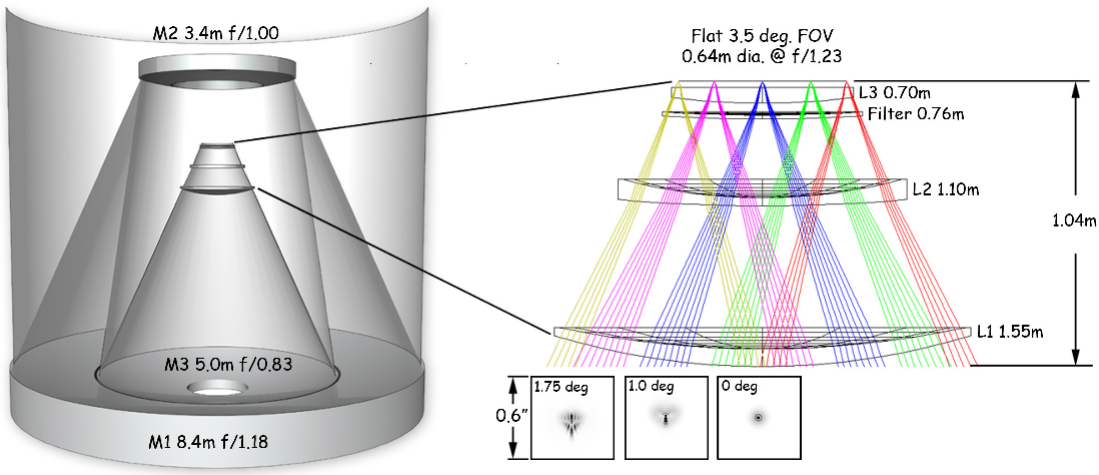

Figure 2.4: The optical design configuration showing the telescope (left) and camera (right) layouts. Diffraction images in r for three field radii, 0, 1.0, and 1.75 degrees, are shown in boxes 0.6 arcseconds square (3×3 pixels). From [77].

the LSST optical alignment. The primary and tertiary mirrors form a continuous surface without any vertical discontinuities. Proposed design makes it possible to fabricate both of them from a single monolithic substrate. The M1-M3 monolith blank was formed in February 2015 from Ohara E6 low expansion glass using the spin casting process developed at Steward Observatory Mirror Lab. The secondary mirror will be made of a low expansion glass (e.g. ULE or Zerodur) using a 100 mm thick solid meniscus blank.

The proposed LSST telescope is a compact, stiff structure with a powerful set of drives, which makes it very accurate and agile. The telescope structure is a welded and bolted steel system designed to be a stiff metering structure for the optics and a stable platform for observing. The primary and tertiary mirrors are supported in a single cell below the elevation ring, the camera and secondary mirror are supported above it.

This construction makes it possible to reorient the telescope very quickly – the motion time for a nominal 3.5° elevation move and a 7° azimuth move is only five seconds. In two seconds, a shaped control profile will move the telescope, which will then settle down to less than 0.1" pointing error in three seconds. There are four motors per axis configured in two sets of opposing pairs to eliminate hysteresis in the system. All-sky pointing performance will be better than 2", which is important for trailing and imaging systematics.

Camera

The LSST camera (Figure 2.5) with size of 1.6 meters by 3 meters and weight of 2800 kilograms will be the largest digital camera ever constructed. It will produce data of extremely high quality with minimal downtime and maintenance. It is a large-aperture, wide-field optical (0.3–1 μm) imager designed to provide a 3.5° field of view with sampling better than 0.2 arcsecond. The image surface is flat with a diameter of approximately 64 cm. Used detectors are 16 Mpixel silicon detectors providing a total of approximately 3.2 Gpixels with read out in

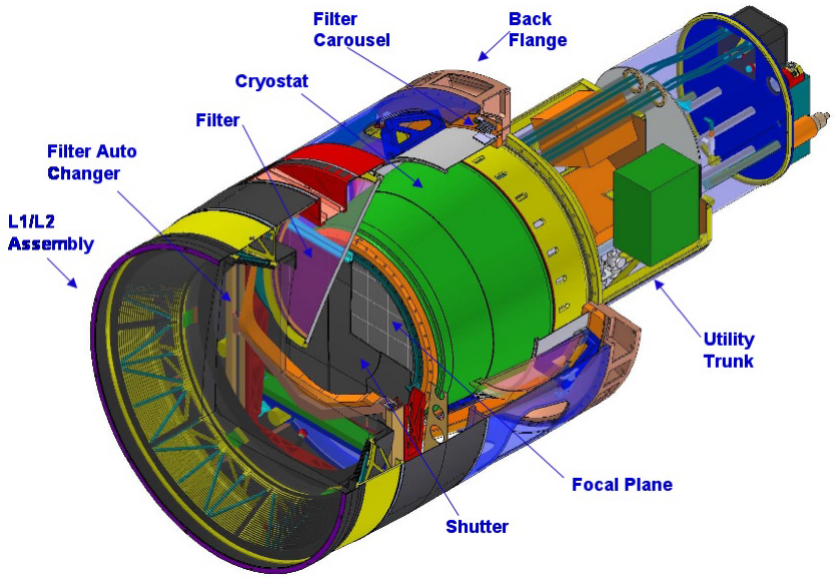

Figure 2.5: Cutaway drawing of the LSST camera. The camera body is approximately 1.6 m in diameter and 3.5 m in length. The optic, L1, is 1.57 m in diameter. From [77].

2 sec (15 sec integration). The camera has 6 filters (*ugrizy*) – ideal filter curves and specifications are in Figure 2.6. The camera is located in the middle of the telescope.

Heat dissipation will be be controlled to limit thermal gradients in the optical beam. In order to achieve the desired detector performance, the focal plane array will operates at a temperature of approximately -100°C . The focal plane array, detector front-end electronics and thermal control are mounted on a silicon carbide grid inside a vacuum cryostat. The cryostat lens serves as an entrance window and vacuum seal for the cryostat. The camera housing is filled with dry nitrogen gas to provide the operating environment for the shutter and filter change mechanisms. The filter carousel can accommodate 5 filters, each 75 cm in diameter, for rapid exchange without external intervention (the sixth filter can replace any of the five via an automated procedure accomplished during daylight hours).

The focal plane consists of 189 arrays ($\sim$16 cm^2 each, 3200 cm^2 focal plane) of 4k×4k CCDs which should ensure wide field of view while filling the focal plane without any large gaps (less than few hundred μm) – the fill factor is 93%. High resistivity silicon substrate and high applied voltages with small pixel size will produce low point spread function (PSF $\ll$ 0.7 arcseconds). Other focal plane requirements include high quantum efficiency (QE) from 320 to 1080 nm, fast f/1.23 focal ratio, high throughput fast readout (2 sec) or low read noise.

Sky survey strategies

Fundamental basis of the LSST observing strategy is to scan the sky deep, wide and fast, and to obtain a dataset that simultaneously satisfies the majority of the science goals. This is done by minimizing slew and other downtime and by making

Filter	Blue Side	Red Side	Comments
u	320	400	Blue side cut-off depends on AR coating
g	400	552	Balmer break at 400 nm
r	552	691	Matches SDSS
i	691	818	Red side short of sky emission at 826 nm
z	818	922	Red side stop before H_2O bands
y	950	1080	Red cut-off before detector cut-off

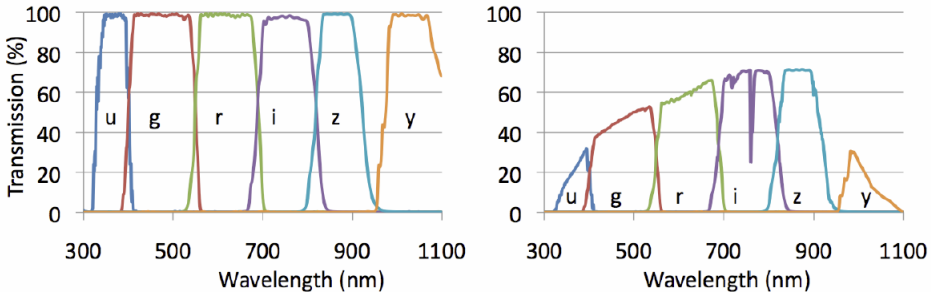

Figure 2.6: Design of filters with transmission points in nanometers (top). The left bottom panel shows the transmission efficiency of the *ugrizy* filters by themselves as calculated from models of the filter performance. The total throughput, accounting for the transmission through the atmosphere at the zenith, the reflectivity of the reflective optics, the transmissivity of the refractive optics, and the quantum efficiency of the sensors is displayed in the bottom panel on the right. From [77].

appropriate choices of the filter bands given the real-time weather conditions.

The LSST Operations Simulator (OpSim) was developed to study and to analyze various science tradeoffs described in § 2.1.2. It contains detailed models of site conditions, hardware and software performance, and an algorithm for scheduling observations which will drive the largely robotic observatory. Observing conditions include a model based on measurements obtained during the site selection. Weather data are taken from ten years of hourly measurements.

For each observation, the signal-to-noise ratio is determined using a detailed sky background model. The time taken to move from one observation to the next is given by a model of the camera, telescope, and dome. After a given exposure, the best option based on a set of scientific requirements modified by observing conditions is selected from all possible next observations. The result of a simulator run is a detailed history of which locations on the sky were observed when, in what filter, and with what sky background, seeing and other observing conditions.

The cadence plan described here (the "universal cadence") based on OpSim is still not definite while there are many variants and alternatives that enhances various specific science programs. However, this plan shows that it is indeed possible to design a universal cadence which addresses a wide variety of science goals in a nearly optimal way.

The main deep-wide-fast survey ($r \sim 24.5$) will use about 90% of the observing time. The remaining 10% of the observing time will be used to obtain improved coverage of parameter space such as very deep ($r \sim 26$) observations, observations with very short revisit times (~1 minute), and observations of "special" regions

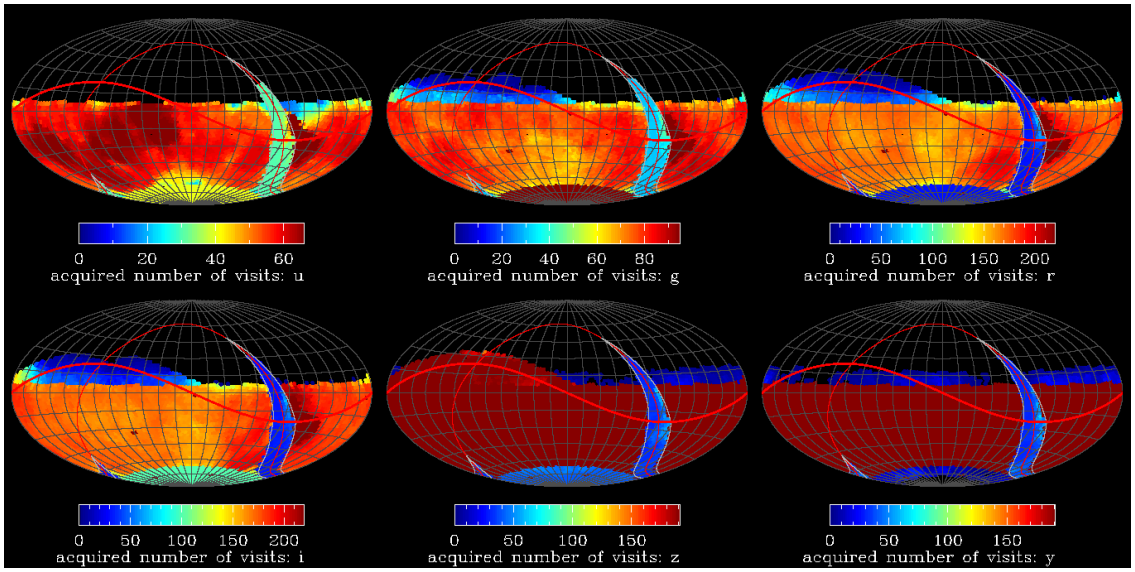

Figure 2.7: The number of visits in one realization of a simulated ten-year survey in all six LSST filters, shown in Equatorial coordinates. The project goals are to have 56, 80, 180, 180, 164, and 164 visits in the u, g, r, i, z, y filters, respectively, over 20,000 deg^{2}of sky. From [77].

such as the Ecliptic, Galactic plane, and the Large and Small Magellanic Clouds. A third type of survey, micro-surveys, that would use about 1% of the time, may also be considered. An example of visit distributions from OpSim over ten years of the survey is showed in Figure 2.7.

The main **Wide-Fast-Deep** mode will focus on the homogeneity of depth and number of visits. In times of good seeing and at low airmass, preference is given to r and i band observations. Observations will be performed by two 15 seconds exposures. Each field will be observed twice with visits separated by 15–60 minutes as often as possible. This strategy will provide motion vectors to link detections of moving objects in the Solar System and thus fulfill the requirement for detecting Near Earth Objects (NEOs) larger than $\sim$ 140 m in diameter. The anticipated total number of visits for a ten-year LSST survey is about 2.8 million ($\sim$5.6 million 15-second long exposures). **North Ecliptic Spur** extends the main survey to 4,000 deg^{2}of the northern ecliptic beyond the airmass limit of the main survey.

The mini-surveys (using roughly 10% of the time) aim to extend the parameter space accessible to the main survey by going deeper (by coadding images up to $r \sim 28$) or by employing different time/filter sampling. The LSST has already selected four distant extragalactic survey fields (Elias S1, XMM-LSS, Extended Chandra Deep Field-South, and COSMOS) that the project guarantees to observe as **Deep Drilling** mode with a deeper coverage and more frequent temporal sampling while more such fields will be chosen. Deep Drilling mode allocates ten minutes of exposure time distributed among filters on a five-day cycle so as to provide high-quality type-Ia supernova light curves at redshifts to $z \sim 1.2$. **Galactic Plane** mode allocates thirty observations in each of six filters in a region of 1000 deg^{2}around the galactic center where a high stellar density leads to a confusion limit at much brighter magnitudes than those attained in the rest

of the survey. **South Celestial Pole** mode allocates thirty observations in each of six filters in a region of $\sim$1700 deg^{2}around the south celestial pole to provide data on the Magellanic Clouds and transients in the southern sky.

Data Management System

The LSST Data Management System (DMS) is required to generate and process a set of data products and to make them available to scientists and the public. DMS creates once per year (more often during the first year of the survey) and archives a Data Release (DR), which is a static selfconsistent collection of data products generated from all survey data. There exist three groups of data, based largely on where and when they are produced.

Level 1 products are continuously generated and/or updated every observing night. These data include alerts, i.e. announcements that the flux or position of a given object has changed significantly. The alerts will be released within 60 seconds of the closing of the shutter at the end of a visit and thus the processing of these data must be highly automated with absolutely minimal human interaction.

Level 2 products are generated as a part of the yearly Data Release. Level 2 products use Level 1 products as input and include data products which require extensive computation. Generation of Level 2 products will be automated, however, significant human interaction may be required.

Level 3 data products are derived from Level 1 and Level 2 data products to support particular science goals. The DMS will provide an interface for programs and an computing infrastructure. These data will not be created by the DMS but rather externally using software written by science collaborations, e.g. DESC (see § 2.1.3).

Level 1 and Level 2 data products will be accessible to the public without restriction altogether with the source code used to generate them.

2.1.2 Survey requirements

The range of scientific investigations which would be enabled by the LSST is extremely broad. Members of the LSST collaboration have identified the four main science programs: Taking an Inventory of the Solar System, Mapping the Milky Way, Exploring the Transient Optical Sky, and Probing Dark Energy and Dark Matter. These science requirements are made in the context of what is expected for the scientific landscape by the end of this decade. The LSST missions and their requirements are summarized in Table 2.1. More information about these goals are described below while detailed description can be found in [68].

Science Mission	Observing Program and Experimental Design	Analytic Methods and Techniques	Survey Requirements
Dark Energy/ Dark Matter	Strong Lensing	Source shape	PSF concentration
	Weak Lensing	Photometric redshifts	PSF shape systematics
	Supernovae	Image differencing	Survey area
	Cluster counting	Precision photometry	Filter definition
	Growth of structure	Photometric variability	Single exposure depth
	BAO	Deep image stack	Photometric precision and accuracy
			Exposures per filter
			Survey cadence (time between revisits)
			Spectral coverage
Solar System Census	NEOs	Image position	Astrometric precision and accuracy
	TNOs	Image differencing	Survey cadence
	MBAs	Moving object linkage	Survey area
	Comets	Time series analysis	
Time Domain/ Transient Discovery	Micro-lensing	Image differencing	Photometric precision and accuracy
	Gamma ray bursts	Photometric variability	Survey cadence
	Active galactic nuclei	Time series analysis	Data processing delay
	Periodic variable stars	Precision photometry	
	Planet transits		
	Unknown events		
Milky Way science	Galactic structure	Image position	Astrometric precision and accuracy
	Accretion streams	Precision photometry	Photometric precision and accuracy
	Density structure	Precision astrometry	Survey cadence
	Solar neighborhood census	Photometric variability	Survey area
			Spectral coverage

Table 2.1: Primary LSST Science Missions, Related Observing Programs, Analytic Methods, and Survey Requirements. From [77].

The single visit depth should reach $r \sim 24.5$ in r-band. This limit is driven by the search for Near-Earth-Objects (NEOs), variable sources (e.g. supernovae, RR Lyrae stars), by proper motion and trigonometric parallax measurements for stars, by coadded survey depth and the minimum number of exposures required by WL science. Single visits will be split into two exposures of equal length to identify and remove cosmic rays.

The coadded survey depth should reach $r \sim 27.5$ in r-band with a sufficient signal-to-noise ratio in other bands to address both extragalactic and Galactic science drivers for cosmological studies.

Image quality should maintain the limit set by the atmosphere – the median free-air seeing is 0.65 arcsec in the r-band. This constraint comes mostly from weak lensing (WL), but also from the required survey depth for point sources and from differencing techniques. The pixel size must be smaller than 0.22 to enable sampling of the point spread function properly in the delivered images.

Photometric repeatability should achieve 5 milimag precision (g, r, i bands) at the bright end, with spatial uniformity of photometric zeropoints across the sky of 10 milimag and band-to-band calibration errors not larger than 5 milimag. These requirements come from the need for high photometric redshift accuracy, the separation of stellar populations, detection of low-amplitude variable objects and the search for systematic effects in type Ia supernova light curves.

Astrometric precision should maintain the limit set by the atmosphere, of about 10 mas for a single image at the bright end (on scales below 20 arcmin). This precision is driven by the desire to achieve a proper motion accuracy of 0.2 mas/yr and parallax accuracy of 1.0 mas over the course of the 10-year survey. A weaker constraint is also placed by the need for a positional cross-correlation with external catalogs.

The single visit exposure time should be less than about a minute to prevent trailing of fast moving objects and to aid control of various systematic effects induced by the atmosphere. It should be longer than ∼20 seconds to avoid significant efficiency losses due to finite readout, slew time, and read noise. The selected optimal value of 2×15 s satisfies both the required final coadded depth, single visit depth, and the revisit time if the effective primary mirror diameter is 6.5m. For various special programs, where fast temporal changes in brightness and position are studied, a shorter exposure time is needed. The minimal exposure time for these goals will be three times shorter than the nominal exposure time (i.e. 5 s).

The filter complement is modeled after the Sloan Digital Sky Survey (SDSS). It includes six filters (*ugrizy*) in the wavelength range 320–1050 nm. Five filters will be used at the same time while the last one can be changed during day. Switching between active filters should take less than two minutes (one minute goal). Accurate photometric redshifts and stellar typing require no large gaps in the coverage. The u- band (330 – 403 nm) is important for separating low-redshift quasars from hot stars, and for estimating the metallicities of F/G main sequence stars. A bandpass with an effective wavelength of about 1 micron would enable studies of sub-stellar objects, high-redshift quasars and regions of the Galaxy that are obscured by interstellar dust.

The revisit time distribution should enable determination of orbits of Solar System objects and sample supernova light curves every few days, while accom-

modating constraints set by proper motion and trigonometric parallax measurements. The LSST will be capable of observing 20,000 deg^2 of the sky in two bands every three nights, but it is desirable to explore much shorter scales, down to 1 minute. This can be achieved with frequent revisits to the same field, or by utilizing field overlap.

The total number of visits of any given area of sky should be of the order of 1,000 to enable WL science, the search for NEOs, proper motion and trigonometric parallax measurements and studies of transient sources.

The distribution of visits per filter should enable accurate photometric redshifts, separation of stellar populations, and sufficient depth to enable detection of faint extremely red sources. An approximately flat distribution of visits among bandpasses will be used. The r and i-bands should be preferentially selected over other bands because they will be used for shape measurements. Other bands cannot be neglected, because a broad wavelength coverage is required to achieve desired photometric redshift accuracy for galaxies and needed color information on transients such as supernovae.

The distribution of visits on the sky should extend over at least $\sim$20,000 deg^2 to obtain the required number of galaxies for WL studies, with attention paid to include "special" regions such as the Ecliptic and Galactic planes, and the Large and Small Magellanic Clouds.

Data processing, data products and data access should result in data products that approach the statistical uncertainties in the raw data. To enable fast and efficient response to transient sources, the processing latency for variable sources should be less than a minute.

These requirements for the scientific goals specified by the system design and other LSST properties are summarized in Table 2.2.

Dark energy and dark matter

Current cosmological models require huge amount of dark matter and some sort of exotic dark energy to be able to fit observations. The nature of this dark matter and dark energy remains unexplained and is one of the primary challenges for fundamental physics. The LSST will create an unique map of a dark matter structure and probe dark energy in multiple ways, providing cross checks and removal of important degeneracies. Primary probes for studying this dark sector are: 1) two and three point weak lensing cosmic shear tomography analyses coupled with galaxy power spectrum, 2) baryon acoustic oscillation (BAO) in the power spectrum of the galaxy distribution, 3) evolution of the mass function of clusters of galaxies, as measured via peaks in the weak lensing shear field and 4) measuring of supernovae of type Ia as standard candles (redshifts and distances measurements). LSST's measurements will be done in moderate redshift, i.e. the epoch at which the dark energy began to dominate the cosmic expansion. When combined with Planck CMB data or other future project's data, the synergy between these probes breaks degeneracies and allows cosmological models to be sharply tested.

The goal in constraining the dark energy is measuring the lowest six eigenmodes of the dark energy equation of state as a function of redshift, and any directional dependence. Combining these probes will allow to measure the growth of cosmic structures and the comoving distance as a function of redshift in the

Field of View	3.5 deg (9.6 $\deg^2$)
Étendue	319 $m^2 deg^2$
Effective clear aperture	6.68 m
Final f-ratio	f/1.234
Primary mirror aperture	8.4 m
Pixel count	3.2 Gpixels
Readout time	2 sec
Dynamic range	16 bits
Plate scale	50.9 μm /arcsec
Filter set (FWHM points – nm)	
–u	330 nm to 403 nm
–g	403 nm to 552 nm
–r	552 nm to 691 nm
–i	691 nm to 818 nm
–z	818 nm to 922 nm
–y	950 nm to 1070 nm
Number of active filters	5
Real-time alert latency	60 s
Fiducial number of visits per point in the main survey	825
Fiducial main survey area	18,000 $\deg^2$
Estimated total covered area, including special programs	25,000 $\deg^2$
Number of	
–visits collected over 10 years	2.75 million
–images collected over 10 years	5.5 million
–visits per night	$\sim$1000
–calibration exposures	450/day
–data collected per 24 hr period	$\sim$15 TB
Standard visit exposure duration	15 s
Time to take a single exposure	18 s
Median slew time between visits	5 s
Time to take one visit in normal survey mode	
–Median	39 s
–Mean	44 s
Estimated number of objects (total)	37 billion
Estimated number of single-epoch sources (total)	7 trillion
Estimated number of forced measurements (total)	30 trillion
Average number of alerts per night	$\sim$10 million
Network bandwidths	
–Summit (Pachón) to Base (La Serena)	2 x 100 Gbps
–Base (La Serena) to Archive (NCSA)	2 x 40 Gbps
Data and compute sizes	
–Final image collection	0.5 Exabytes
–Final database size	15 PB
–Final disk storage	0.4 Exabytes
–Peak number of nodes	1750 nodes
–Peak compute power in LSST data centers	1.8 PFLOPS

Table 2.2: LSST System and Survey Key Numbers. From [78].

range $0.3 < z < 3.0$ with an accuracy of 1–2%. Sufficient number of galaxies with very accurate photometric redshift are crucial for obtaining this accuracy. Combining BAO with weak lensing of galaxies can significantly reduce sensitivity to bias systematics.

Solar system

Small bodies of the Solar System – their orbital elements, sizes, and color distributions – provide a unique insight into its early stages. The LSST will measure orbital parameters for several million moving objects, which represents an increase of factors of ten to one hundred over the numbers of objects with documented orbits, colors, and variability information now. This will enable testing of various theories for the formation and evolution of our planetary system.

The LSST will make huge advance in studying objects beyond Neptune (trans-Neptunian Objects, TNOs). The LSST will survey for asteroids, get superb orbits, go tremendously faint, and measure precise colors, allowing measurement of light curves for thousands of trans-Neptunian Objects, producing rotation periods and phase curves, yielding shape and spin properties, and providing clues to the early environment in the outer Solar System. The LSST will also catalog 90% of all potentially hazardous asteroids larger than 140 meters in diameter that travel in Earth-crossing orbits.

Galactic Structure

The structure and stellar content of the Milky Way encode a history of its formation. The LSST will enable studies of the distribution of numerous main sequence stars beyond the presumed edge of the Galaxy's halo, their metallicity distribution throughout most of the halo, and their kinematics beyond the thick disk/halo boundary, and will obtain direct distance measurements below the hydrogenburning limit for a representative thin-disk sample. The LSST will enable precise studying of the structure and accretion history of the Milky Way and will measure the fundamental properties of all the stars within 300 pc of the Sun.

The LSST will produce a massive and exquisitely accurate photometric and astrometric data set – about 10^{10} stars will be detected, with sufficient signal-to-noise ratio to enable accurate light curves, geometric parallax, and proper motion measurements for about billion stars. The accurate multi-color photometry can be used for source classification, and measurements of detailed stellar properties such as effective temperatures to a rms accuracy of 100 K and metallicity to a rms accuracy of 0.3 dex (decimal exponent).

Transient objects

The LSST will open a new window on the variable sky. The LSST, with its repeated, wide-area coverage to deep limiting magnitudes will enable the discovery and analysis of rare and exotic objects such as neutron star and black hole binaries, gamma-ray bursts and X-ray flashes, active galactic nuclei (AGN) and blazars, and very possibly new classes of transients, such as binary mergers and stellar disruptions by black holes. Numerous microlensing events in the Local Group are also expected. With its large aperture, the LSST is well suited to conducting a

Deep Supernova Search in selected areas. The LSST will also provide a powerful new capability for monitoring periodic variables, such as RR Lyrae stars, which can be used to map the Galactic halo.

Other science themes

It is anticipated that the LSST will enable far more diverse science than encompassed by the four themes described above that drive the system design. Among many other scientific programs the LSST will enable for example:

- detailed studies of galaxy formation and evolution using their distribution in luminosity-colormorphology space as a function of redshift for an unprecedentedly large number of galaxies,
- testing evolutionary cosmic downsizing scenarios and much clearer understanding of black hole growth during the first Gyr by discovering ∼1000 AGNs with very faint luminosities and large redshifts ($z \sim 6 - 7.5$),
- first wide field survey of ultra low surface brightness galaxies, with photometric redshift information,
- search for strong gravitational lenses to a faint surface brightness limit, which can be used to explore the dark matter profiles of galaxies.

Synergy with other projects

The LSST will cooperate with other projects and benefit from their data and multiple wavelengths, depth, and timescales. SDSS [104], SkyMapper [103] or the Gaia [48] survey will cover most of the celestial sphere to a limit several magnitudes fainter than the LSST. The Pan-STARRS [90] surveys will provide multi-epoch data deeper than SDSS in the northern sky, and the DES (more in § 2.3.2) in the southern sky. The Gaia survey will provide calibration checks at the bright end for proper motions and trigonometric parallax measurements by LSST. Other surveys will provide in addition to LSST data temporal, spectral and spatial resolution coverage as well as cross-correlation of their data. Collaboration with other projects will be necessary to provide calibration of photometric redshifts.

2.1.3 Dark Energy Science Collaboration

The LSST Project Team has been assembled to design and build the telescope, camera, and data management systems but it is not a scientific collaboration in the usual sense. While scientists working on the LSST Project are interested in the scientific questions that LSST data can address, they are not officially involved in the scientific analyses of those data. Therefore, a number of quasi-independent scientific collaborations, which provided advices on technical issues and helped articulate the scientific case for the LSST, have created the LSST Dark Energy Science Collaboration (DESC) in 2012 during a meeting at the University of Pennsylvania.

DESC prepares variety of cosmological analyses for the LSST survey. In advance of LSST's first observations, the DESC helps prepare for the LSST science

analysis, make synergistic connections with ongoing cosmological surveys and provide the dark energy community with state of the art analysis tools. Primary goal of the DESC is the study of dark energy and related topics in fundamental physics with data from the LSST. For more information see the DESC's white paper [1].

Analysis working groups cover five key probes of dark energy: weak lensing, large scale structure, galaxy clusters, Type Ia supernovae, and strong lensing. The DESC will identify and work to minimize the most significant systematic uncertainties that limit the sensitivity of each probe. In addition to these primary goals the DESC will also address joint tasks: calibration strategies for photometric redshifts, cosmological simulations, simulated catalogs, photon-level simulations, cross working group tools, technical coordination (instrument model, calibration and survey operations), and theory and framework for combining and jointly interpreting the dark energy probes.

2.1.4 Cosmological Probes of Dark Energy

Here we present a brief description of cosmological probes which will be used when constraining dark energy. For more details see e.g. [119] or [70].

Supernovae

Supernovae (SNe) are the most straightforward tool for studying cosmic acceleration, as they directly discovered the acceleration in the first place [99]. Type Ia supernovae (SNe Ia) are exploding stars defined by the lack of hydrogen and the presence of silicon in their early-time spectra [58], and are a product of a thermonuclear explosion of a C/O white dwarf. Observations show that SNe Ia have a luminosity peak that is tightly correlated with the shape of their light curves – supernovae that rise and fall more slowly have higher peak luminosity (first quantified by [92]). From observations of (multiband) light curve shapes and colors the luminosity at a brightness peak can be predicted.

To measure cosmic expansion with Type Ia SNe, the observed flux and predicted luminosity are compared. From that the supernova's luminosity distance can be measured. An accurate redshift is obtained by measuring the host galaxy (calibrator). Since the distances to the local calibrators are usually determined from the Hubble expansion, this method gives the luminosity distance D_L in units of h^{-1} Mpc. Measured relation is used to constraint dark energy parameters.

Long-term task of the SN working group within DESC is *Develop theoretical/numerical/empirical SN models to better describe or improve the distance indicator.*

Baryonic acoustic oscillations

Baryonic acoustic oscillations (BAO) provide an entirely independent way of measuring cosmic distance. Sound waves propagating before recombination imprint a characteristic scale on matter clustering. The acoustic length scale can be computed as

$$r_s = \int_0^{t_*} \frac{c_s(t)}{a(t)} \mathrm{d}t = \int_{z_*}^{\infty} \frac{c_s(z)}{H(z)} \mathrm{d}z, \tag{2.1}$$

where asterisk denotes time (redshift) at recombination and c_s is the sound speed. The behavior of $H(z)$ depends on the ratio of the matter density to radiation density and the sound speed depends on the ratio of radiation pressure to the energy density of the baryon-photon fluid, determined by the baryon-to-photon ratio. Both the matter-to-radiation ratio and the baryon-to-photon ratio can be measured from the CMB anisotropy power spectrum. This gives $r_s \sim 150$ Mpc. The scale of the acoustic feature is stable to better than 1% accuracy, making it an excellent standard ruler.

This effect can be detected in the angular clustering of galaxies in bins of photometric redshift, yielding the angular diameter distance. Furthermore, measuring the BAO scale in a velocity separation allows a direct determination of $H(z)$. The BAO method measures $D(z)$ in absolute units – Mpc not h^{-1} Mpc like SNe measurements, and thus BAO measurements to the same redshift carry different information. At low redshift ($z \lesssim 0.5$), the BAO method strongly complements SN measurements, while at higher redshift ($z \gtrsim 0.5$) the BAO method is an powerful probe of dark energy and cosmic geometry.

Weak lensing

Gravitational lensing is the deflection of light from distant sources due to the bending of space-time by baryonic and dark matter (lenses) along the line of sight (more about lensing in § A.3.2). It is a very useful cosmological probe because it is sensitive to all matter regardless of its nature. In the limit of very small deflection angles it is called weak lensing (WL). WL causes tiny distortions ($\sim 0.5\%$), or "shear", in galaxy sizes and shapes – see Figure 2.8. Intrinsic size or shape of a given galaxy are unknown, but normally, galaxy orientations are assumed to be random ($\sim 30\%$ dispersion), so they should not exhibit statistically significant and coherent alignments. In the presence of lensing, small but coherent shears in background galaxy images are induced. This means that WL is statistically detectable by averaging shapes over many lensed galaxies. In principle either the shearing of galaxies (shape distortion) or their magnification (size distortion) can be measured. However, in practice the shape distortions is used much more widely, since the scatter in shapes of galaxies is less than the scatter in their sizes.

Weak lensing provides a direct measure of the distribution of matter, independent of any assumptions about galaxy biasing[1]. Since this distribution can be predicted theoretically, and its amplitude can be directly used to constrain cosmology, weak lensing has great potential as a cosmological probe. The correlation of the density field of nearby galaxies with the lensing shear measured on more distant galaxies is called *galaxy-galaxy lensing*. Most lens systems involve sources (and lenses) at moderate or high redshift, and thus can lensing probe the geometry of the Universe – the measurement of the shear correlation function as a function of the redshifts of observed galaxies is called *tomography*. The scaling of the galaxy-galaxy lensing signal as a function of the source redshift, known as *cosmography*, depends purely on geometric factors and hence can be used to construct a distance-redshift relation.

[1]Galaxy bias is the difference in the distribution of galaxies and that of the underlying dark matter. The biasing factor b is defined such that the relative fluctuations in the spatial number density of galaxies are b times the relative density fluctuations.

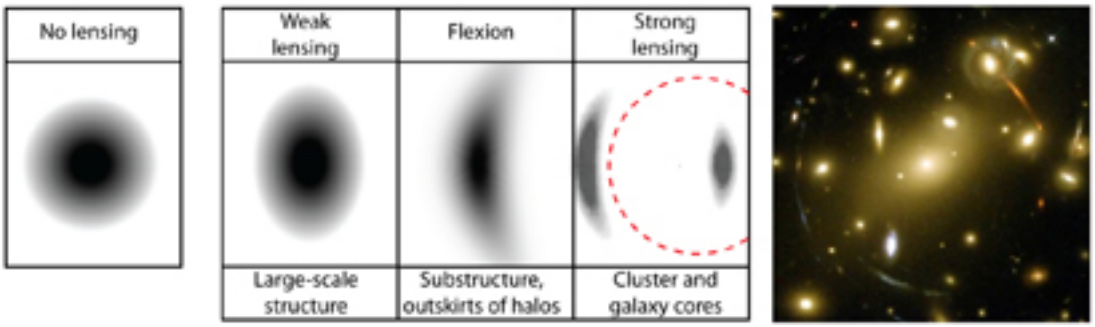

Figure 2.8: (Left) Illustrations of the effect of a lensing mass on a circularly symmetric image. Weak lensing elliptically distorts the image, flexion provides an arc-ness and strong lensing creates large arcs and multiple images. (Right) Galaxy cluster Abell 2218, strongly lensed arcs can be seen in around the cluster. Every background galaxy is weakly lensed. From NASA, ESA, and Johan Richard (Caltech, USA).

Long-term tasks of the WL working group within DESC are *Develop non-canonical WL statistics that have the potential to improve dark energy constraints* and *Extend WL data analysis methods from Stage III surveys to LSST.*

Large-scale structure

Studying the large-scale structures (LSS) of the Universe is of a great importance for the cosmology. Since the clustering of matter on scales from galaxies to superclusters came from quantum fluctuations in the very early Universe with important modification by radiation and baryons, the LSS encode critical information about the contents of the Universe, the origin of the fluctuations, and the cosmic expansion background in which the structures evolved.

Measurements of large-scale power spectrum for the spatial distribution of matter as a function of redshift constrain the cosmic expansion history, the cosmological distance scale, the growth rate of structures, the mass of the neutrinos and the abundance of dark matter. This includes BAO measurement of the distance-redshift relation (as a standard ruler). The BAO with the growth of the LSS in the Universe form two robust probes of dark energy, and a potential discriminator between dark energy and modified gravity models. Beyond the dark energy, the large scale power spectrum is a probe of both neutrino mass and primordial non-gaussianity.

Long-term task of the LSS working group within DESC is *Scalable optimal LSS analysis software development.*

Galaxy clusters

The observed number density and clustering of galaxy clusters as a function of mass and redshift provides a powerful toolset to constraining cosmology. Galaxy clusters provided the first line of evidence for the existence of dark matter [125] and cluster mass-to-light ratio measurements suggested that the matter density in the universe was sub-critical [67]. Galaxy clusters measurements are sensitive to both the expansion history and the growth of structure in the Universe en-

abling to distinguish between dark energy and modified gravity models for cosmic acceleration. Additional probes are measurements of the baryonic mass fraction in clusters, and of the tomographic lensing signatures through clusters.

The basic idea of cluster abundance studies is to compare the predicted space density of massive halos to the observed space density of clusters. The basic observables are the richness, the number of galaxies in a specified luminosity and color range. Halo abundance is sensitive to the amplitude of the matter power-spectrum σ_8[2] and the matter density Ω_m, more precisely a combination of a form $\sigma_8\Omega_m^q$, with $q \approx 0.4$ [121]. The degeneracy between σ_8 and Ω_m can be broken by measuring abundances at a variety of masses.

Long-term task of the Cl working group within DESC is *Optimizing magnification-based cluster mass calibration.*

Strong lensing

Strong gravitational lensing (SL) refers to the multiple imaging of a background object due to a massive foreground object (typically clusters of galaxies) – see Figure 2.8. The resulting angular displacement, morphological distortion, and time delay can be used to measure dark energy parameters. Strong gravitational lensing time delays measure a combination of distances that combining with other dark energy probes can further constraint cosmological parameters. The time delays is also expected to test gravity on scales where the screening mechanisms is becoming active (more about screening mechanisms of modified gravities in § 3.2.2).

Another independent way to measure dark energy parameters with SL is the analysis of systems with multiple sets of multiple images [72]. The positions of these multiple images depend strongly on the detailed properties of the lens mass distribution and on the angular diameter distance ratios between the lens, source and observer, they encapsulate information about the underlying cosmology. This dependence on the geometry can be used to derive constraints on the cosmological parameters.

Long-term task of the SN working group within DESC is *Explore multiple source plane cosmography as a competitive DE probe.*

Redshift-space distortions

When we observe distant galaxies, two features determine their redshifts – the Hubble expansion and their peculiar velocities. The peculiar velocities of galaxies thus cause them to appear displaced along the line of sight in redshift space. These displacements lead to redshift distortions in the pattern of clustering of galaxies in redshift space and make large scale galaxy clustering anisotropic. Redshift-space distortions (RSD) have the tremendous advantage of bearing information about the dynamics of galaxies. The strength of the anisotropy is governed by distortion parameter $\beta = f(z)/b(z)$, where $f(z)$ is the logarithmic growth rate of fluctuations. By modeling the full redshift-space galaxy power spectrum one can obtain combination of the product of the matter clustering amplitude and the growth rate.

[2] σ_8 is a linear fluctuation in the mass distribution on scales of $8h^{-1}$ Mpc

Anisotropy of galaxy clustering offers an alternative to weak lensing and cluster abundances as a tool for measuring the growth of structures. RSD directly measure the rate at which structure is growing at the redshift of observation unlike WL and galaxy cluster measurements which measure the rate of growth at multiple redshifts. RSD measurements can improve constraints on dark energy models and they can be used to constrain departures from GR by testing consistency of the growth and expansion histories. The key challenge in modeling RSD is accounting for nonlinear effects, including nonlinear or scale-dependent bias between galaxies and matter, at the level of accuracy demanded by the LSST's precision.

2.2 Euclid mission

Euclid is an ESA (European Space Agency) high-precision space mission designed to map the geometry and evolution of the universe and to study properties of dark matter and dark energy. Its primary goal is to place high accuracy constraints on dark energy, dark matter, gravity and cosmic initial conditions using two independent cosmological probes – weak gravitational lensing and baryonic acoustic oscillation – out to redshift $z \sim 2$. Galaxy clusters and the Integrated Sachs-Wolfe effect will be used as secondary cosmological probes. Along with these tasks will Euclid's visible and near infrared imaging and spectroscopy of the entire extragalactic sky produce legacy science for various fields of astronomy, e.g. galaxy evolution, large-scale structures or the search for high-redshift objects. The Euclid mission has been adopted with launch planned for 2020. Overview of the Euclid system design and scientific requirements can be found in [75].

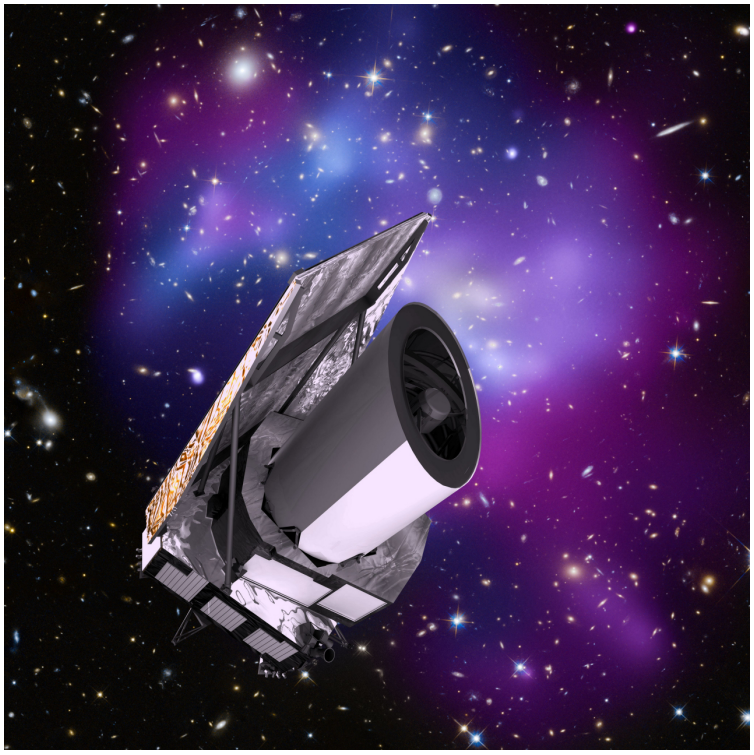

Figure 2.9: Artist's impression of Euclid. From ESA-C. Carreau.

Instrument	Field of view (deg^2)	Band	Wavelength (nm)	Limiting AB mag	Resolution
VIS	0.787×0.709	R+I+Z	550 – 920	24.5	0.1" pixel
NIP	0.763×0.722	Y	920 – 1146	24.0	0.3" pixel
		J	1146 – 1372	24.0	0.3" pixel
		Hp	1372 – 2000	24.0	0.3" pixel
NIS slitless	0.763×0.722	Hs	1000 – 2000	19.5	$R = 500 \pm 20$

Table 2.3: Instrument bands. From [12].

2.2.1 Overview of Euclid System Design

The mission is based on a telescope with a primary mirror of 1.2 m diameter. The Euclid payload consist of a wide-field (0.5 deg^2) imager comprising visible and near infrared (NIR) and a NIR spectrometer. The shapes of galaxies for weak lensing will be measured via the visible channel, with a resolution of 0.18 arcsec in a wide visible red band (R+I+Z, 0.55 – 0.92 μm). The visual imager consists of 36 arrays of 4k×4k CCDs. The NIR photometric channel provides three NIR bands (Y, J, H, spanning 1.0 – 1.6 μm) with a resolution of 0.3 arcsec. The baseline for the NIR spectroscopic channel operates in the wavelength range 1.0 – 2.0 μm in slitless mode at a spectral resolution $R = \lambda/\Delta\lambda \sim 500$, employing 0.5" pixels. The NIR spectrometer and photometer consists of 16 arrays of 2k×2k near-infrared sensitive HgCdTe detectors. The optional spectroscopic implementation is slit spectroscopy using digital micro-mirror devices. Instruments characteristics are summarized in Table 2.3

The mission will survey 20 000 deg^2 of the extragalactic sky in the regions of the North and South galactic poles (Galactic latitude |b|$>$ 30°). in the visible channel down to AB = 24.5 mag. Two types of redshift will be collected. For all galaxies, photometric redshifts will be obtained from the broad band visible and near-IR measurements. For the sub-sample of galaxies brighter than H(AB) = 19.5 mag, redshifts will be measured directly with the NIR slitless spectroscopic channel. Along with the *wide* extragalactic survey, a *deep* survey of roughly 40 deg^2 will be performed by multiple visits in the vicinity of the ecliptic poles. The deep survey will provide the calibration of the photometric redshifts of the wide survey, as well as additional science. The sky survey is accomplished by collecting daily strips made up of contiguous, partly overlapping fields.

The Euclid system is driven by the diverse dark energy probes, each with its own specific requirements – by the width and speed of the envisaged sky survey; by the survey depth and signal-to-noise ratios; and, by programmatic constraints.

Spacecraft

The Euclid spacecraft will have a launch mass of around 2100 kg. It will be about 4.5 m tall and 3.1 m in diameter. The Euclid spacecraft will be made up of two major assemblies – payload module and service module. The payload consists of a 1.2-m aperture telescope with two instruments: the visual imager and the near-infrared spectrometer and photometer.

The Euclid telescope is a three mirror Korsch configuration with a 0.45 deg off-axis field and an aperture stop at the primary mirror. The entrance pupil

diameter is 1.2 m, the optically corrected and unvigneted field of view is 0.79×1.16 deg^2, and the focal length is 24.5 m. In order to meet the scientific performance requirements the telescope must operate at a reduced temperature – a maximum operating temperature of about 240 K.

The service module hosts most of the spacecraft subsystems that are needed to operate the payload, including telemetry, power, thermal control, and attitude and orbit control. The service module provides X and K band communications, with a K band science data rate of 55 Mbit/s during the daily telecommanding. To store the large data volume that will be accumulated during observations, Euclid will have a mass memory of at least 2.6 Tbit. To meet the high precision imaging requirements, the Euclid control provides an extremely stable pointing with a dispersion of less than 35 milli-arcseconds per visual exposure. At those accuracies, a high thermal stability is also required to protect the telescope assembly from optical misalignments.

Mission operations

Euclid will depart from Europe's Spaceport in French Guiana and be carried by a Soyuz ST 2-1b launch vehicle. A free-insertion launch opportunities can be found almost through the whole year. Approximately in 30 days will Euclid reach the second Sun-Earth Lagrange point L2. Then it will rotate in an orbit around L2 with large amplitude about million kilometers. This orbit provides optimal conditions for Euclid – a benign radiation environment and very stable observing conditions. An instability inherent in the motion about L2 requires periodic corrections. Every 30 days throughout the operation will be performed station-keeping manoeuvres and take less than one day.

The Euclid mission will deliver large volume of data – about 850 Gbit of compressed data per day that will be transfered at the rate of 55 Mbit/s. This data will be handled by the Euclid ground segment. The ground station network for Euclid will be composed of the 15-m antenna at Kourou and the 35-m antennas at New Norcia and Cebreros (see Figure 2.10) at the beginning of the mission (the Lunch and Early Operations Phase) with almost 24-hour coverage of the spacecraft during this period. For the rest of the time will be used 35-m antennas at the Cebreros ground station in Spain or the Malargue ground station in Argentina with 4-hour time for the daily telecommanding and communications. The rest of the day the spacecraft will be operating without ground contact. The Mission Operations Centre will be set up at ESA's European Space Operations Centre in Darmstadt, Germany.

Sky survey strategies

In order to bring the wide extragalactic survey to less than four years (requirement of 4.5 yr maximum), many variants of strategies were studied. The basic strategy of the sky mapping consists in performing sequential observations by rotating about the spacecraft X-axis, nominally pointed at the sun, each day covering a strip along the intersection of a great circle perpendicular to the sun line with the extragalactic caps. However, int this basic strategy the complete coverage is achieved in six years. This occurs because of a lesser efficiency in the vicinity of

Figure 2.10: ESA's 35 m-diameter deep-space dish antenna, DSA-2, is located at Cebreros, near Avila, Spain, as part of the ESTRACK network. From [47].

the ecliptic poles, due to a strip overlapping, as well as a dead time around the equinoxes.

Modified strategy was introduced in order to overcome these difficulties. In this variant, the X-axis is allowed to make an angle of up to 30° with the direction of the sun, by rotating the spacecraft around Y-axis. This allows observing sky areas at longitudes different from those in the basic strategy. As a consequence one can now explore the dead zones of the basic strategy by tilting the spacecraft around its Y-axis while the standard scanning sequence is used for zones where no loss of efficiency occurs due to excessive strip overlaps. The modified strategy has also a drawback – there appears an unreachable zone in each of the galactic caps. Imaging that zone would require extending the mission beyond four years. Simulation of the visits after four years of the mission is shown in Figure 2.11.

2.2.2 Survey Requirements

The requirements on size reconstruction and stability of the PSF lead to high image quality and thus large data rates.

Weak lensing requires a high image quality for the shear measurements, near-infrared imaging capabilities to measure photometric redshifts for galaxies at redshifts $z > 1$, a very high degree of system stability to minimize systematic effects, and the ability to survey the entire extra-galactic sky.

The survey speed is guaranteed by the combination of a large field of view an optimized sky mapping strategy, and minimized dead times such as attitude transitions, leading to a requirement for fast slews.The survey depth and signal-

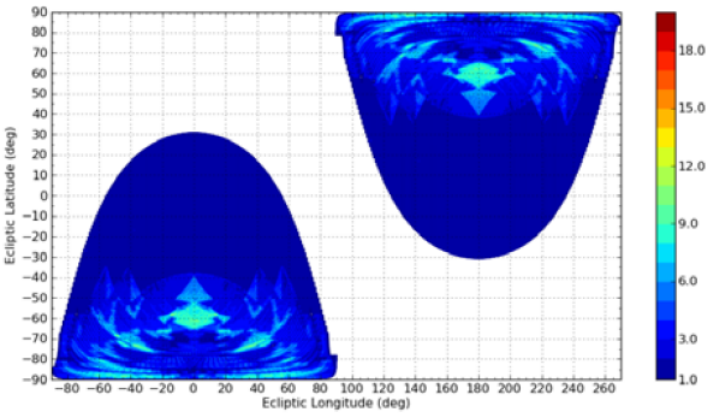

Figure 2.11: Visit count after 4 yars. From [12].

to-noise ratio requirements lead to a well baffled design, low temperature optics and detectors, and, driven by the NIR instruments NIP and NIS, a cold telescope for low thermal IR background, and extensive on- board data processing for noise limitation.

2.2.3 Science Goals

The Euclid imaging instrument is optimized for the weak gravitational lensing as the main cosmological probe. The Euclid imaging surveys will also make use of several secondary cosmological probes such as the Integrated Sachs-Wolfe Effect (ISW), galaxy clusters to provide additional measurements of the cosmic geometry and structure growth (some of these probes were described in § 2.1.4).

Euclid's four primary science objectives in fundamental cosmology are: 1) to measure the dark energy equation of state parameters[3] w_0 and w_a to a precision of 2% and 10% from the geometry and structure growth of the Universe; 2) to test the validity of General Relativity against modified gravity theories, and measure the growth factor exponent γ to an accuracy of 2%; 3) to study the properties of dark matter by mapping its distribution, testing the Cold Dark Matter paradigm and measuring the sum of the neutrino masses to a few 0.01eV in combination with Planck; and 4) to improve the constraints on the initial condition parameters by a factor of 2–30 compared to Planck alone.

Euclid is therefore poised to uncover new physics by challenging all sectors of the cosmological model. The Euclid survey can thus be thought as the low-redshift, 3-dimensional analogue and complement to the map of the high-redshift universe provided by CMB experiments. More about the primary and legacy science which will be achieved with the Euclid in [98].

Legacy science

Beyond these objectives in fundamental cosmology, the Euclid imaging surveys will provide legacy science in various fields of astrophysics. Euclid will deliver high quality morphologies and masses for billions of galaxies out to $z \sim 2$, over the entire extra-galactic sky, with a resolution four times better and three

[3]Dark energy equation of state is commonly parametrized as $w = w_0 + (1 - a)w_a$.

NIR magnitudes deeper than ground based surveys which will enhance studies of galaxy evolution. The Euclid deep survey will probe ages of galaxy formation ($z > 6$) and the era of reionisation of the Universe ($z > 10$). Euclid will also augment the Gaia survey of our Milky Way, taking it several magnitudes deeper and adding infrared colors for every Gaia star it observes. Euclid will detect nearby extremely low surface brightness tidal streams of stars thus allowing us to probe the formation and evolution of the Milky Way. The Euclid imaging surveys will also provide key measurements of the mass function of galaxy clusters and of over 10^5 strong lensing systems. Through the microlensing technique Euclid will undertake a programme to detect Earth-mass planets in the habitable zone.

2.2.4 Additional Cosmological Probes

The two main cosmological probes of the Euclid – weak gravitational lensing and baryonic acoustic oscillation – have been introduce in § 2.1.4. Here we briefly describe additional cosmological probes.

Integrated Sachs-Wolfe effect

The Integrated Sachs-Wolfe (ISW) effect is an independent probe of dark energy, curvature and deviations from General Relativity on large scales. It can be measured using correlations of the CMB with tracers of LSS. The ISW effect arises from the time-variation of the scalar metric perturbations. There exists an early- and a late-time ISW effect. The early effect is important around recombination when anisotropies can start growing and the radiation energy density is still dynamically important. The late ISW effect (which is of more importance here) originates much later after the onset of matter domination from the time derivative of the gravitational potential.

The late-time ISW effect can be due to dark energy domination at low redshift, curvature, or modifications to the growth of structure on large scales. In flat universe with no modifications to gravity, detection of the ISW is a direct signature of the presence of dark energy.

The observed temperature fluctuation at the angular position $\hat{\mathbf{n}}$ on the sky in is [87]

$$\frac{\delta T}{T} = \frac{\delta T}{T}(\eta_*) - \Phi(\eta_0) + \Phi(\eta_*,\ \hat{\mathbf{n}}) + [\mathbf{v}\cdot\mathbf{e}]_{\eta_0}^{\eta_*} - 2\int_{\eta_0}^{\eta_*} \mathrm{d}\eta \frac{\partial \Phi}{\partial \eta}, \tag{2.2}$$

where Φ is the gravitational potential[4], η_* denotes the conformal time of the recombination time, and η_0 today.

The first term is the intrinsic photon fluctuation at the last scattering surface other than those induced by the metric perturbations. The second term is the gravitational redshift due to our gravitational potential which is the monopole contribution and cannot be observed. The third term represents the temperature anisotropy caused by the gravitational redshift due to the potential fluctuations at the recombination epoch (early-time ISW). The fourth term is the Doppler effect that is induced by the relative motion between the observer and the CMB last

[4]In GR, the gravitational potential equals the curvature potential Ψ. More generally, in the integral in (2.2) should be a sum of these potentials $\Phi + \Psi$ instead of a factor of two. More detailed derivation of the ISW with general scalar perturbations is in § A.2.

scattering surface. The final integral term represents the temperature anisotropy caused by the time variation of gravitational potential integrated along the line of sight (late-time ISW).

Galaxy correlations

The statistical distribution of galaxies is a very powerful tool with which to probe the composition of the Universe. One of them is e.g. the BAOs. However, the full statistic of the three-dimensional distribution contains much more information. On linear scales there are three main features in the galaxy power spectrum [98]:

- The broad-band power: Information is contained in the shape, normalization and time evolution of the power spectrum.
- The Baryon Acoustic Oscillations: Information is contained in the tangential and radial wavelengths, as well as the wiggles amplitude.
- The linear redshift space distortions: Even when considering the projected power spectrum, this radial information is partially present.

The Euclid will provide a photometric galaxy survey over the redshift range $z \sim 0 - 2$. The measurement of the statistical distribution of galaxies can be done in real space ($\xi(r)$), configuration space ($w(\theta)$), Fourier space ($P(k)$) or in Spherical Harmonic space ($C(l)$). The Euclid will concentrate on a Fourier space wiggles-only method [102] as well as a projected spherical harmonic method which is ideal to study tangential modes on a sphere.

2.2.5 Comparison and Synergy with LSST

Both Euclid and the LSST have the same scientific goal(s) – reduce errors on dark energy equation of state and constrain modified gravity. Both of them want to achieve this by deep (AB $\sim 24 - 27$) and large sky survey. Also the main probes are the same – weak lensing and baryonic acoustic oscillation. The main difference is their approach to systematic errors. The LSST will observe the same patch of sky thousand times to get rid of instrumental and atmospheric distortion, while Euclid, in space, will avoid the atmospheric distortion and plan a stable observation.

The other difference is in the observable spectrum – the LSST will cover six visible bands (*ugrizy*, 300 – 1100 nm) while Euclid will cover visible red band (550 – 900 nm) and three near-infrared bands (YJH, 1000 – 1600 nm). Both Euclid and the LSST will cover ∼20,000 deg^2 with overlap area ∼11,000 deg^2. It is estimated that at least one billion of galaxies will have measurable NIR colors from Euclid while the LSST will provide multicolor visible band photometry required for the weak lensing. The LSST will be premier facility to provide such measurements in the southern hemisphere. While the combined ground-based visible and space-based NIR photometry is essential for Euclid, it is also useful for the LSST. The use of YJH photometry from Euclid does yield a modest but significant improvement in photo-z determination over what the LSST can provide alone with its six-color photometry. Euclid spectroscopic data may also play a significant role in helping to calibrate photo-z determination, especially at

higher redshifts. Finally, comparison of Euclid and LSST shear determination for common fields will be helpful in understanding shape measurement systematics for weak lensing investigations with both facilities.

2.3 Other Surveys

There are many other projects and mission which study properties of the dark energy, either as a main scientific goal, or as a complementary program. Among the big surveys are e.g. Sloan Digital Sky Surveys (SDSS, official site [104]) – from the beginning of regular surveys in 2000 till 2014 there were seven finished surveys in total (SDSS-I/II results [74], SDSS-III results [14]), while there are three ongoing surveys from 2014 (SDSS-IV). Other surveys are e.g. Wilkinson Microwave Anisotropy Probe (WMAP, official site [122], results [61]); Planck (official site [49], results [3]); Hobby-Eberly Telescope Dark Energy Experiment (HETDEX, official site [59]); or Wide field Multi-Object Spectrograph (WFMOS, Gemini study report [16]). In this section we just briefly introduce three further examples – finished BOSS, ongoing DES, and future WFIRST.

2.3.1 Baryon Oscillation Spectroscopic Survey

The Sloan Digital Sky Survey's (SDSS-III) Baryon Oscillation Spectroscopic Survey (BOSS) is a six-year program (Fall 2009 – Spring 2014) that uses the wide-field 2.5-m telescope at Apache Point Observatory. The BOSS is designed to measure the scale of BAO in the clustering of matter over a larger volume than the combined efforts of all previous spectroscopic surveys of large-scale structures. BOSS uses 1.5 million luminous galaxies to measure BAO to redshifts $z < 0.7$. Observations of neutral hydrogen in the Lyα forest in more than 150,000 quasar spectra constrain BAO over the redshift range $2.15 < z < 3.5$ [41].

There are two double spectrographs, each covering the wavelength range 361 nm – 1014 nm with resolution $R = \lambda/\Delta\lambda$ ranging from 1300 at the blue end to 2600 at the red end. Both spectrographs have a red channel with a 4k $\times$ 4k, 15μm pixel CCD from Lawrence Berkeley National Laboratory (LBNL). Both spectrographs have a blue channel with a 4k $\times$ 4k, 15μm pixel CCD from e2v. The instrument is fed by 1000 optical fibers (500 per spectrograph), each subtending 2" on the sky.

Using the acoustic scale as a physically calibrated ruler, BOSS determines the angular diameter distance with a precision of 1% at redshifts $z = 0.3$ and $z = 0.57$ using the distribution of galaxies and measurements of $H(z)$ to 1.8% and 1.7% at the same redshifts. At redshifts $z \sim 2.5$ the angular diameter distance and $H^{-1}(z)$ is measured to an accuracy of 1.9% using Lyα forest.

BAO measurements with the CMB-calibrated physical scale of the sound horizon and SN data yields of $H_0 = (67.3 \pm 1.1)$ km$\cdot$ s^{-1} Mpc^{-1} with 1.7% precision [14]. This measurement assumes standard pre-recombination physics but is insensitive to assumptions about dark energy or space curvature. When we allow more general forms of evolving dark energy, the BAO+SN+CMB parameter constraints are always consistent with flat ΛCDM values at 1σ. While the overal χ^2 of model fits is satisfactory, the Lyα forest BAO measurements are in moderate $(2 - 2.5\sigma)$ tension with model predictions. Models with early dark energy

that tracks the dominant energy component at high redshift remain consistent with expansion history constraints, and they yield a higher H_0 and lower matter clustering amplitude, improving agreement with some low-redshift observations.

2.3.2 Dark Energy Survey

The Dark Energy Survey (DES) is designed to probe the origin of the accelerating universe and to help uncover the nature of dark energy by measuring the 14-billion-year history of cosmic expansion with high precision. DES is an optical near infrared survey of 5000 deg^2 of the South Galactic Cap to $r \sim 24$ in *grizy* spectrum. DES's instrument consists primarily of a new camera, Dark Energy Camera (DECam), specifically designed to be sensitive to the highly redshifted light from distant galaxies. DECam is mounted on a classic telescope, the Blanco 4-m telescope at the Cerro Tololo Inter-American Observatory (CTIO) in La Serena, Chile. The imaging system is supported by a combination of microwave and optical data links that will provide the recorded data to the survey members. Starting in August of 2013 and continuing for five years, DES has begun to survey a large swath of the southern sky out to vast distances in order to provide new clues to this most fundamental questions [2].

The survey data allow to measure the dark energy and dark matter densities and the dark energy equation of state through four independent methods: galaxy clusters (counts and spatial distributions at $0.1 < z < 1.3$), weak gravitational lensing tomography (on several redshift shells to $z \sim 1$), galaxy angular clustering, and supernova distances (at $0.3 < z < 0.8$).

The main tool is the DECam, 74 2k $\times$ 4k 570 Mpx digital camera built at Fermilab in Batavia. It provides a 2.2° field of view image at 0.27"/pixel. It covers wavelength range 400–1100 nm with five filters (*grizy*). The electronics will allow an entire digital image to be read out and recorded in 17 seconds, time that it takes the telescope to move to its next viewing position.

From the first two years of observation a mass map from weak gravitational lensing shear measurements over 139 deg^2 has been reconstructed [35]. There is a good agreement between the mass map and the distribution of massive galaxy clusters identified using a red-sequence cluster finder. These measurements are consistent with simulated galaxy catalogs based on ΛCDM N-body simulations, suggesting low systematics uncertainties in the map.

2.3.3 Wide-Field Infrared Survey Telescope

The Wide-Field Infrared Survey Telescope (WFIRST) is a NASA large space mission designed to settle essential questions in dark energy, exoplanets, and infrared astrophysics. It is designed to perform wide-field imaging and slitless spectroscopic surveys of the near infrared sky. The current Astrophysics Focused Telescope Assets (AFTA) design of the mission makes use of an existing 2.4-m telescope to enhance sensitivity and imaging performance. It is the top-ranked large space mission in the New Worlds, New Horizon (NWNH) Decadal Survey of Astronomy and Astrophysics. The main instrument is a wide-field multi-filter NIR imager and spectrometer. With the 2.4-m telescope, a coronagraph instrument has been added to the payload for direct imaging of exoplanets and

debris disks. If authorized for a mission start in 2017, WFIRST-AFTA would launch in the early 2020s [115].

The mission will feature strategic key science programs plus a large program of guest observations (see Appendix A of [106]). The main focus is on the dark energy and fundamental cosmology (determine the expansion history of the Universe and the growth history of its largest structures). The next scientific goal is discovering of exoplanets – by microlensing photometric survey of the Galactic bulge and by a direct high-contrast imaging and spectroscopic survey of the nearest stars. Data for general astrophysics science will be gathered by surveys at high Galactic latitudes and Galactic bulge. Relatively huge priority is assigned to the guest observer science program.

The payload features a 2.4-m telescope, which feeds the wide-field instrument (wide-field channel and an integral field unit spectrograph channel) and the coronagraph instrument. The wide-field channel covers a wavelength range 0.76–2.0 μm and a spectroscopy mode covering 1.35–1.89 μm . The wide-field focal plane uses 18 4k $\times$ 4k HgCdTe detector arrays. The integral field unit channel uses an image slicer and spectrograph to provide individual spectra of each slice covering the 0.6–2.0 μm spectral range. The coronagraph instrument provides high-contrast imaging and spectroscopy. Direct imaging is provided over a bandpass of 430–970 nm, while spectroscopy is provided by the spectrograph over the spectral range of 0.6–0.97 μm with a spectral resolution of $R \sim 70$ [106].

As WFIRST will be a NIR mission it will require visible band photometry for photo-z determination. LSST will be the premier ground-based facility to provide those data. As for Euclid, the baryon acoustic oscillation spectroscopic survey will be helpful for calibrating photo-z determinations for LSST. The comparison of shear determinations between WFIRST and LSST measurements will be useful for understanding shape measurement systematics with both facilities.

3. Modified Gravity and Dark Energy

If the surveys described above are to be successful in interpreting their results, many different theories of gravity need to be explored. This chapter serves as a brief review of the various models of modified gravity and dark energy. At first, we present problems with the cosmological constant as an explanation of the acceleration of the Universe. Next we introduce general properties of modifications of gravity and then we deal with the most studied theories – quintessence, k-essence, models with coupled dark energy with special attention to the chameleon gravity, two models of unified dark energy and dark matter, and $f(R)$ theories.

3.1 Problems with Cosmological Constant

Standard cosmological ΛCDM model is in a good agreement with all measurements of CMB [3], type Ia supernovae [4], or BAO [14]. So why we want to study physics beyond this concordance cosmology? Why are we not satisfied with the cosmological constant as an explanation of the acceleration of the Universe?

First of all, let me stress that the cosmological constant Λ is itself a modification of GR, and not a nice or elegant one, just the simplest. One adds into the action of GR a constant of unknown origin and ridiculously small value right next to the curvature with the clear purpose. There are two major problems with the cosmological constant referred to as the *fine-tuning problem* and the *coincidence problem*.

Fine-Tuning Problem

The first problem could be phrased as the question: *Why is the observed value of* Λ *so small in Planck units?* In order to realize the cosmic acceleration today, we require that the cosmological constant Λ is of the order of the square of the present Hubble parameter H_0. If we interpret this as an energy density, it is equivalent to

$$\rho_\Lambda = \Lambda M_{pl}^2 \approx 10^{-120} M_{pl}^4 \approx 10^{-47}\ \mathrm{GeV}^4. \tag{3.1}$$

Suppose that this energy density comes from the vacuum energy. The zero-point energy of some field of mass m with momentum k is

$$E_0 = \langle 0\,|H|\,0\rangle = V \int \frac{\mathrm{d}^3 k}{(2\pi)^3} \frac{1}{2} \sqrt{k^2 + m^2}, \tag{3.2}$$

where $V = (2\pi)^3 \delta^3(0)$ is the volume of space. If we trust our theory up to some cut-off scale $\Lambda_{UV} \gg m$, we obtain the vacuum energy density

$$\rho_{vac} = \int_0^{\Lambda_{UV}} \frac{4\pi k^2 \mathrm{d}k}{(2\pi)^3} \frac{1}{2} \sqrt{k^2 + m^2} \approx \frac{\Lambda_{UV}^4}{16\pi^2}. \tag{3.3}$$

If we take the cut-off scale to be order of the Planck scale $M_{pl} \approx 10^{18}$ GeV, we get a value of about 120 orders of magnitude larger than the observed value. This

situation is not better for different scales in particle physics. For the SUSY[1] scale $\Lambda_{SUSY} \approx 10^3$ GeV, even for the QCD scale $\Lambda_{QCD} \approx 0.1$ GeV, is ρ_{vac} still much larger than ρ_Λ. Even if the value of Λ does not originate from the vacuum energy there is no such a small scale in known physics – not in GR nor in quantum physics. This huge discrepancy between theoretical predictions and observed value of Λ is a major issue in physics and cosmology.

Coincidence Problem

The second problem could be phrased as the question: *Why is the energy density ρ_Λ so close to the present matter density?* While the energy density of the cosmological constant (vacuum energy) remains constant in time and was completely negligible in most of the past, the energy density of matter evolves like $\rho_m \propto (1+z)^3$ and will be entirely negligible in the future. According to the Copernican principle [46] we do not live in a special place **nor time**. Thus it is very unlikely that these two components will have densities of the same order of magnitude in the present. If $\rho_\Lambda^{(0)}/\rho_m^{(0)}$ was just 10 or 100 times smaller, we would not see any accelerated expansion. If it were a few orders of magnitude larger than one, the transition to the accelerated universe would occur at a large redshift.

The so-called anthropic principle can seemingly give us the explanation for both of the two cosmological constant problems, why it is small and why the acceleration starts now. Because if the vacuum energy has been big and dominant from the earlier epoch, there would be no chance to form structures in the Universe, like galaxies, stars, planets and us, intelligent lives. But this anthropic explanation of the value ρ_Λ makes sense only if there is a multiverse with a lot different realizations of ρ_Λ. But we live only in our realization of the Universe and therefore we cannot verify whether the anthropic principle solves the cosmological constant problem or not.

Beside these two problems concerning the cosmological constant, the observations of coherent acoustic oscillations in the CMB [3] has turned the notion of accelerated expansion in the very early universe (inflation) into an integral part of the cosmic standard model. This early accelerated expansion was not due to the cosmological constant, because in that case the inflation would not stop and today's universe would not be possible. Therefore, we have to postulate some new scalar field (inflaton) [36] that we know so little about. If we do not properly understand the past dynamics of the universe how can we accept the cosmological constant as an explanation of the present acceleration without doubt?

[1] In some supersymmetric theories, the number of fermionic and bosonic degrees of freedom are equal. The energy of the vacuum fluctuations per degree of freedom is the same in magnitude but opposite in sign for fermions and bosons of the same mass. Therefore the fermion and boson contributions cancel each other and the total vacuum energy density (and consequently Λ) vanishes. As the supersymmetry has to be broken today (we do not observe supersymetry in nature) supersymmetric partners can have different masses of order $\Lambda_{SUSY} \approx 10^3$ GeV.

3.2 Beyond ΛCDM

If extensions of the standard model prove the vacuum energy to be exactly zero or we are not satisfied with the cosmological constant and its problems we need to find alternative models of dark energy. Since general relativity is an unique theory of a massless spin 2 degree of freedom, modifying gravity means changing its degrees of freedom – usually adding a scalar degree of freedom[2] [62]. Theories of modified gravity (and dark energy) are obtained by modifying the classical Einstein-Hilbert action of general relativity (with the cosmological constant Λ)

$$S = \frac{M_{pl}^2}{2} \int \mathrm{d}^4x\sqrt{-g}\,[R - 2\Lambda] + S_m[\psi_m; g_{\mu\nu}], \tag{3.4}$$

where R is the Ricci scalar and S_m is the matter action with matter fields Ψ_m which are minimally coupled to gravity[3]. This action can be modified basically in two ways. The first approach is based on modified matter models in which we add additional fields of an exotic matter – *dark energy* with a negative pressure, and thus modifying right hand side of the Einstein equations – the energy momentum tensor $T_{\mu\nu}$. The second approach is based on *modified gravity* models in which we modify gravity part of the action and thus modifying the left hand side of the Einstein equations – the Einstein tensor $G_{\mu\nu}$. We can also mix gravity and matter parts of the action together, i.e. involve in the action fields with non-minimal coupling.

Note that within GR one cannot distinguish between models of modified gravity and dark energy – gravity modifications can be absorbed in the matter part of the action and vice versa. By a conformal transformation one can directly assign new fields to any modifications of gravity (see § 3.2.1). By using only gravitational interactions there is no way how to distinguish between these two approaches. In the particle physic and quantum field theory there is of course the difference and it is up to them to distinguish what can cause these modifications.

We cannot modified action (3.4) arbitrary if we want to involve in equations of motion only second derivatives of the fields. This requirement comes from the Ostrogradski‘s theorem which basically claims that such theories are unstable and involve ghosts[4][123]. However, we can still involve in equations of motion higher order derivatives by violating assumption of the Ostrogradski‘s theorem, i.e. the nondegenerancy of a conjugate momentum.

General scalar-tensor theories defined by the Horndeski extension[65] leads to

[2]Extra scalar degrees of freedom are the most preferable modifications of gravity. Quintessence or k-essence contains these fields directly; $f(R)$ gravity through the presence of higher derivatives; a massive graviton has more degrees of freedom than a massless one and one of these behaves like an additional scalar mode; or in many brane world models there is an extra scalar mode corresponding to the position of the brane in the extra dimension.

[3]By minimally coupled matter fields are meant fields that are coupled to gravity only through the determinant of the metric $\sqrt{-g}$ and the canonical kinetic term $-\frac{1}{2}g^{\mu\nu}\partial_\mu\phi\partial_\nu\phi$.

[4]*Ghost* is a state of a negative norm or a field with the kinetic term of the wrong sign. Ghosts in quantum physics break the unitarity and generally implies classical instabilities either at the background or at the perturbed level [53].

the action

$$\begin{aligned} S =& \frac{M_{pl}^2}{2}\int \mathrm{d}^4x\sqrt{-g}\Big\{G_2(\varphi,X) - G_3(\varphi,X)\Box\varphi + G_4(\varphi,X)R \\ &+ \frac{\partial G_4}{\partial X}\left[(\Box\varphi)^2 - (\nabla\nabla\varphi)^2\right] + G_5(\varphi,X)G_{\mu\nu}\nabla^\mu\nabla^\nu\varphi \\ &- \frac{1}{6}\frac{\partial G_5}{\partial X}\left[(\Box\varphi)^3 - 3\Box\varphi(\nabla\nabla\varphi)^2 + 2(\nabla\nabla\varphi)^3\right]\Big\} + S_m[\psi_m; g_{\mu\nu}], \end{aligned} \tag{3.5}$$

where $X \equiv -\frac{1}{2}(\partial\varphi)^2$ is the canonical kinetic energy and $G_{\mu\nu}$ is the Einstein tensor. The scalar field φ is coupled with gravity via the covariant derivatives, R and $G_{\mu\nu}$. Functions G_i are arbitrary functions of φ and X. This action defines the most general scalar-tensor theory with at most second order derivatives of the fields in equations of motion.

The Horndeski action incorporates many models of modified gravity, e.g. Chameleon gravity, $f(R)$ gravity or Galileon models. Classical ΛCDM model is recovered by

$$\begin{aligned} G_2(\varphi,X) =& -2\Lambda, \\ G_3(\varphi,X) =& \, G_5(\varphi,X) = 0, \\ G_4(\varphi,X) =& \, 1. \end{aligned} \tag{3.6}$$

K-essence – dark energy described by a single, real scalar field φ, minimally coupled to gravity but with a non-canonical kinetic term – we get by

$$\begin{aligned} G_2(\varphi,X) =& \frac{2}{M_{pl}^2}K(\varphi,X), \\ G_3(\varphi,X) =& \, G_5(\varphi,X) = 0, \\ G_4(\varphi,X) =& \, 1. \end{aligned} \tag{3.7}$$

Special case of k-essence, the quintessence – scalar field with a canonical kinetic term rolling in a potential – is obtained from (3.7) by choice $K(\varphi,X) = X - V(\varphi))$.

Another broad subclass of the Horndeski action – the Jordan-Brans-Dicke models [24] – can be obtained by choice

$$\begin{aligned} G_2(\varphi,X) =& -2\left[U(\varphi) - \frac{\omega(\varphi)}{\varphi}X\right], \\ G_3(\varphi,X) =& \, G_5(\varphi,X) = 0, \\ G_4(\varphi,X) =& \, \varphi, \end{aligned} \tag{3.8}$$

where $U(\varphi)$ is the scalar field potential and $\omega(\varphi)$ is the Brans-Dicke parameter determining the kinetic coupling. This leads to an action (in the Jordan frame)

$$S = \frac{M_{pl}^2}{2}\int \mathrm{d}^4x\sqrt{-g}\Big\{\varphi R - \frac{\omega(\varphi)}{\varphi}(\partial\varphi)^2 - 2U(\varphi)\Big\} + S_m[\psi_m; g_{\mu\nu}]. \tag{3.9}$$

Although the Brans-Dicke parameter ω is generally a function of the field φ many models assume ω to be constant while the condition $\omega > -3/2$ guarantees the theory to be ghost-free.

The so called $f(R)$ gravity models, where the Einstein-Hilbert action (3.4) is supplemented with a free nonlinear function of the Ricci scalar, replacing $R \to R + f(R)$, can be embedded in the Jordan-Brans-Dicke subclass of the Horndeski action with

$$\begin{aligned} \omega &= 0, \\ \varphi &= 1 + f_{,R}, \\ U(\varphi) &= \frac{R f_{,R} - f}{2}. \end{aligned} \tag{3.10}$$

3.2.1 Jordan vs. Einstein Frame

The action (3.9) is described in the so-called Jordan frame, where the matter fields are minimally coupled to the metric and follow geodesics. We can also describe this in the so-called Einstein frame, where "standard" gravity is restored. Using the conformal transformations

$$\begin{aligned} \tilde{g}_{\mu\nu} &\equiv \varphi g_{\mu\nu} \\ \left(\frac{\mathrm{d}\phi}{\mathrm{d}\varphi}\right)^2 &\equiv \frac{M_{pl}^2}{2}\frac{3+2\omega}{\varphi^2} \\ A(\phi) &\equiv \varphi^{-1/2} \\ V(\phi) &\equiv M_{pl}^2 \frac{U(\varphi)}{\varphi^2} \end{aligned} \tag{3.11}$$

which leads to

$$S = \int \mathrm{d}^4x\sqrt{-\tilde{g}}\left[\frac{M_{pl}^2}{2}\tilde{R} - \frac{1}{2}(\partial\phi)^2 - V(\phi)\right] + S_m[\psi_m; A^2(\phi)\tilde{g}_{\mu\nu}], \tag{3.12}$$

where tildes denote quantities in the Einstein frame. This action looks like the Einstein-Hilbert action with minimally coupled scalar but now the matter fields are also coupled with the scalar field via the factor $A(\phi)$.

There is a difference whether one takes action (3.9) or (3.12) to be the fundamental action defining the modified gravity. In the former one there is only one coupling constant β, defined by $A(\phi) = \exp(\beta\phi/M_{pl})$, for all matter fields. If one takes the action in the Einstein frame to be the fundamental one the matter action is replaced by $S_m[\psi_m; A^2(\phi)\tilde{g}_{\mu\nu}] \to S_i[\psi_i; A_i^2(\phi)\tilde{g}_{\mu\nu}]$ where one can define the coupling strengths β_i to the different matter components to be different. This is very important for tests of modified gravity. For instance, if there is minimal coupling to the baryonic matter – $\beta_b = 0$, Solar System or astrophysical tests do not constraint coupling strength to the cold matter β_c whereas the cosmological observation do.

Also other theories than Jordan-Brans-Dicke theory, e.g. Kaluza-Klein theories and higher derivative theories of gravity, can be formulated in two different ways [51].

What does it mean that two frames are conformally related? Are these frames equivalent? And how is this equivality defined? It has been shown in [79] that these two frames are *mathematically* equivalent, i.e. every solution in one frame implies an existence of a solution in the other frame and can be mapped into this frame. But this does not necessary mean that they are *physically* equivalent and

quantities defined in the individual frames are those we observe. There has been many debates about the (in)equivalence of these frames ([94]) and whether which one is the physical ([52]). Many contradictory arguments (sometimes incorrect) of both sides result into confusion and ambiguous viewpoints.

Both frames have some issues with fundamental principles. In the Jordan frame the weak energy condition can be violated and hence states with the negative energy are possible. Moreover, there is no guarantee of stability of ground state. All *classical* fields are believed to satisfy the energy condition but no so in quantum theories. On the other hand in the Einstein frame the weak energy condition is satisfied but due to the non-universal coupling of the matter fields the equivalence principle is violated. However this violation is only weak and can pass the Solar system tests.

So far it has not been definitely decided which frame is the physically correct one or whether they are equivalent and a complete agreement has not been reached in the community on this issue. For more information see e.g. [31][30].

3.2.2 Screening Mechanisms

We know that general relativity with the cosmological constant and assumptions about cold dark matter can describe our universe very well. That means that any modified cosmology must be able to recover ΛCDM cosmology to a high accuracy. This is not normally an issue. However, since modifications of GR typically involve extra scalar degree of freedom there are interactions with matter that are unavoidable – no symmetry can prevent all couplings to the standard model. This coupling to matter means that there should be a fifth force. Because we do not see any fifth forces or modifications of gravity in the laboratory or in the Solar System we need to suppress these fifth forces – we need some sort of a *screening mechanism*.

A nature of the screening mechanisms can be different. Let us start from (3.12) with generalized kinetic term $-\frac{1}{2}Z(\phi, \partial\phi, ...)(\partial\phi)^2$. We can solve the equations of motion for the background in a minimum of a potential $V(\phi)$ and write $\phi = \phi_0 + \delta\phi$, where ϕ_0 is a background solution and $\delta\phi$ is a fluctuation. The Lagrangian density for the fluctuations to the second order (first order vanishes) is

$$\mathcal{L} \propto -\frac{1}{2}Z(\phi_0)(\partial\delta\phi)^2 + \frac{1}{2}m^2(\phi_0)\delta\phi^2 + \frac{\beta(\phi_0)}{M_p}\delta\phi\delta T, \tag{3.13}$$

where $m^2(\phi) \equiv V_{,\phi\phi}(\phi)$. Now, any of these three terms can serve as a screening term:

- *Large inertia* – a large Z makes it hard for the scalar to propagate and leads to the kinetic type of the screening, where first or second derivatives being important (Galileons [86], massive gravity [62], Vainshtein mechanism [15]);
- *Large mass* – a large m means the scalar propagates only over short distances and leads to the chameleon type of the screening, where in regions of high density, such as on the Earth, the field acquires a large mass (Chameleon mechanism [118]);

- *Weak coupling* – a small β in regions of high density makes the interaction with matter fields weaker and leads to symmetron ([63]) or varying dilaton ([39][25]) theories.

3.3 Quintessence

Quintessence, from the Latin "fifth element", is according to ancient and medieval philosophy the fifth element, or ether, supposed to be the constituent matter of the heavenly bodies after air, fire, earth, and water. The name quintessence, or the Q component, was first used by [27] for canonical scalar field ϕ evolving along a potential $V(\phi)$. Such a dynamical field can reproduce the late-time acceleration with the equation of state $w = w(t) \approx 1$. Although quintessence can alleviate the coincidence problem of dark energy via the so-called tracker solution, it still suffers by the fine-tunning problem as the potential needs to be flat enough to lead to the slow-roll inflation today with an energy scale $\rho_{DE} \simeq 10^{-120} M_{pl}^4$ and a mass scale $m_\phi \lesssim 10^{-33}$ eV. However, such fine-tunned potentials can be constructed within the framework of particle physics.

Quintessence is one of the simple models of dark energy as it is a canonical scalar field that interacts with all the other components only through standard gravity. The lagrangian density for the quintessence field is

$$\mathcal{L}_\phi = -\frac{1}{2}(\partial\phi)^2 - V(\phi) \tag{3.14}$$

We can compute the stress-energy tensor as

$$T^\phi_{\mu\nu} \equiv \frac{-2}{\sqrt{-g}} \frac{\delta(\sqrt{-g}\mathcal{L}_\phi)}{\delta g^{\mu\nu}} = \partial_\mu\phi\partial_\nu\phi - g^{\mu\nu}\left(\frac{1}{2}(\partial\phi)^2 + V(\phi)\right). \tag{3.15}$$

Now, the energy density and pressure is given by components of the stress-energy tensor. For FLRW background and ϕ only time-dependent we get

$$\rho_\phi = -T^0_0 = \frac{1}{2}\dot{\phi}^2 + V(\phi) \qquad p_\phi = \frac{1}{3}T^i_i = \frac{1}{2}\dot{\phi}^2 - V(\phi). \tag{3.16}$$

Equation of state for the quintessence is then

$$w \equiv \frac{p}{\rho} = \frac{\dot{\phi}^2 - 2V(\phi)}{\dot{\phi}^2 + 2V(\phi)}. \tag{3.17}$$

We require the condition $w < -1/3$ to realize the late-time cosmic acceleration, which translates into the condition $\dot{\phi}^2 < V(\phi)$, i.e. the potential needs to be shallow enough for the field to evolve slowly along the potential. For a slow-rolling field such as $\dot{\phi} \ll V(\phi)$ equation of state (3.17) reduce to $w \approx -1$ as indicated by cosmological measurements.

The variation of (3.14) with respect to ϕ gives us the equation of motion for the scalar field ϕ

$$\ddot{\phi} + 3H\dot{\phi}^2 + V_{,\phi} = 0. \tag{3.18}$$

3.3.1 Thawing or Freezing

Depending on which term and when determines the evolution of the field, the quintessence models has been dynamically classified into *freezing* models and *thawing* models [28]. In the freezing models the field was rolling along the potential in the past, but the movement gradually slows down as the field approaches the minimum of the potential ($\dot{\phi} \to 0$) and the system enters the phase of the cosmic acceleration ($w \to -1$). In the thawing models the field was initially frozen ($\dot{\phi} \approx 0$) in the early matter era because of the Hubble friction (the term $H\dot{\phi}$) until recently and then it begins to evolve once H drops below m_ϕ and w evolves from -1.

A potential of the freezing models is for example

$$V(\phi) = M^{4+n}\phi^{-n} \ (n > 0), \tag{3.19}$$

which appears in the fermion condensate model as a dynamical supersymmetry breaking [21]. This potential does not possess a minimum and hence the field rolls down the potential toward infinity. Another example of a potential in the freezing models is

$$V(\phi) = M^{4+n}\phi^{-n} \exp\left(\alpha\phi^2/M_{pl}^2\right), \tag{3.20}$$

which can be constructed in the framework of supergravity [26]. This potential has a minimum at which the field is eventually trapped (corresponding to $\dot{\phi} = 0$ and hence $w = -1$).

Broader class of potentials belonging to the thawing models are so-called hilltop quintessence models [43], in which the scalar field is rolling near a local **maximum** in the potential but it begins to roll down around the present. A particularly example that is well-described by this model is the pseudo-Nambu-Goldstone Boson (PNGB) model [55], for which the potential is given by

$$V(\phi) = M^4 \left[\cos\left(\phi/f\right) + 1\right]. \tag{3.21}$$

3.3.2 Tracker Solutions

In the tracker solution the quintessence component tracks the dominant background density for most of the history of the Universe, then only recently grows to dominate the energy density and drives the Universe into a period of an accelerated expansion [116]. The simplest form of the tracker solution is obtained from the potential (3.19).

One takes into account both radiation and non-relativistic matter together (characterized by one energy density $\rho_M = \rho_m + \rho_r$ and equation of state w_M) with the quintessence field. In radiation and matter dominant epochs the equation of state of quintessence in the tracking regime is given by [11]

$$w_\phi \approx \frac{nw_M - 2}{n + 2}, \tag{3.22}$$

which is valid as long as $\rho_\phi \ll \rho_M$. A remarkable feature is that w_ϕ decreases to a negative value after the transition from the radiation dominated epoch to the matter dominated epoch ($w_M \approx 0$) regardless of the initial value of w_ϕ – the initial ratio of the quintessence energy density ρ_ϕ to the matter density ρ_m can

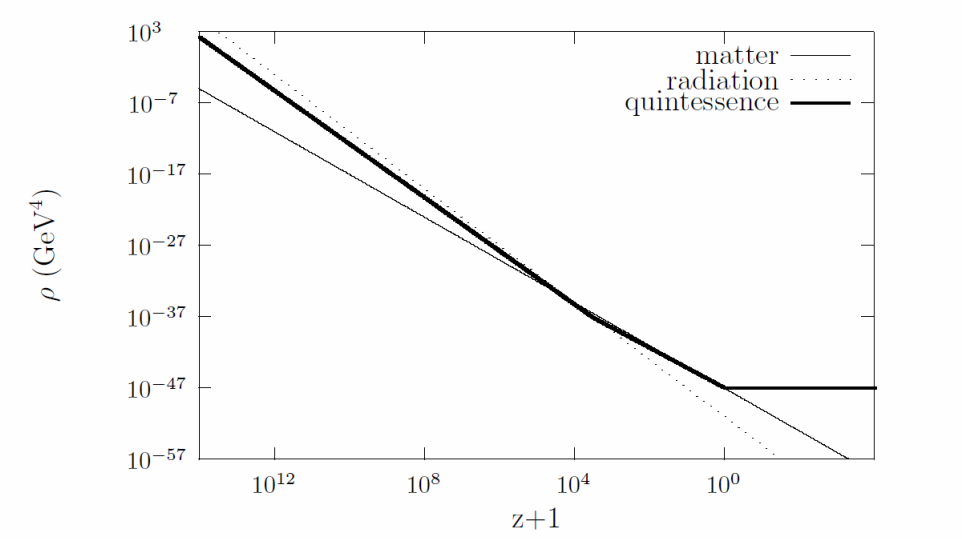

Figure 3.1: A plot of energy density vs. redshift using the equation of state for a tracker solution. For an illustration, $n = 30$ in the (3.19) is plotted. The dotted line is for radiation, the solid line is for matter, and the thick solid line is for quintessence. From [116].

vary by nearly 100 orders of magnitude and does not affect the cosmic history [124].

Since ρ_ϕ decreases more slowly than ρ_M, in later epoch ρ_ϕ becomes relatively large and at some time catches up with ρ_M and start to dominate the Universe. In that epoch $w_\phi \approx -1$ and the quintessence field drives the late time accelerated expansion of the Universe. The evolution of the energy density is showed in Figure 3.1.

The fact that the evolution of ρ_ϕ does not depend on initial conditions partially solves the cosmological constant problems. However, the value of M in the potential (3.19) still needs to be fine-tunned and the quintessence theory gives no explanation of this value.

3.4 K-essence

Quintessence models are based on a scalar field with a canonical kinetic term and a slowly varying potential. However, in the context of particle physics there appear scalar fields with non-canonical kinetic terms. In [13] it is shown that a large class of scalar fields with non-canonical kinetic terms can, without the help of potential terms, drive an inflationary evolution starting from rather generic initial conditions. The Lagrangian density for the k-essence is

$$\mathcal{L}_K = P(\phi, X), \tag{3.23}$$

where $X = -\frac{1}{2}(\partial\phi)^2$ is the canonical kinetic energy and the function $P(\phi, X)$ must vanish for $X \to 0$ (otherwise there would be some potential term).

The energy-momentum tensor of the k-essence is given by

$$T^K_{\mu\nu} \equiv \frac{-2}{\sqrt{-g}} \frac{\delta(\sqrt{-g}\mathcal{L}_K)}{\delta g^{\mu\nu}} = P_{,X}\partial_\mu\phi\partial_\nu\phi + g^{\mu\nu}P, \tag{3.24}$$

which is of the form of a perfect fluid, $T_{\mu\nu} = (\rho+p)u_\mu u_\nu + g_{\mu\nu}p$, with a four-velocity $u_\mu = \partial_\mu\phi/\sqrt{2X}$, pressure $p_K = P$ and energy density

$$\rho_K = 2XP_{,X} - P. \tag{3.25}$$

The equation of state of the k-essence is then

$$w_K = \frac{p_K}{\rho_K} = \frac{P}{2XP_{,X} - P}, \tag{3.26}$$

which is $w_K \approx -1$, as long as the condition $XP_{,X} \ll P$ is satisfied.

In the low-energy effective string theory appear higher-order derivative terms coming from α and loop corrections to the tree-level action [56]. The k-essence action for these theories is for example

$$P = K(\phi)X + L(\phi)X^2. \tag{3.27}$$

Phantom or ghost scalar fields with a negative kinetic energy $-X$ and $w \lesssim -1$ can also fit the current observations. These ghost fields generally suffer from a quantum instability problem unless higher-order terms in X or ϕ are taken into account in the Lagrangian density [11]. The action of so-called dilatonic ghost condensate model is [93]

$$P = -X + e^{\kappa\lambda\phi}X^2/M^4. \tag{3.28}$$

3.4.1 Attractor Solutions

As an example, the cosmological evolution of the dilatonic ghost condensate model with $\lambda = 0.2$ in the flat FLRW background (with both matter and radiation fluids) is shown in Figure 3.2. During radiation and most matter eras, the equation of state w_ϕ is close to -1 and the energy density of the field ρ_ϕ is negligibly small relative to the background fluid density. Once the field energy density begins to dominate over the background fluid density, w_ϕ starts to evolve from -1. Since the deviation from $w_\phi = -1$ appears around the present epoch, the dilatonic ghost condensate model corresponds to the thawing model of k-essence. Unlike thawing models of quintessence the field acquires a nearly constant energy by its kinetic term.

In addition to these types of solutions, where k-essence is attracted to an equation of state which is different from matter or radiation, there are also tracker solutions in which k-essence mimics the equation of state of the background component in the Universe [116].

As in the case of the quintessence, the cosmic evolution in the presence of the k-essence is insensitive to initial conditions and the field is attracted to the attractor solution wherever it started. In addition to solving the coincidence problem the k-essence does not need a potential energy term thus it is free from fine-tuning that arose in quintessence models. However, the k-essence does not solve the vacuum energy problem and, in some era, the field can travel with superluminal speeds.

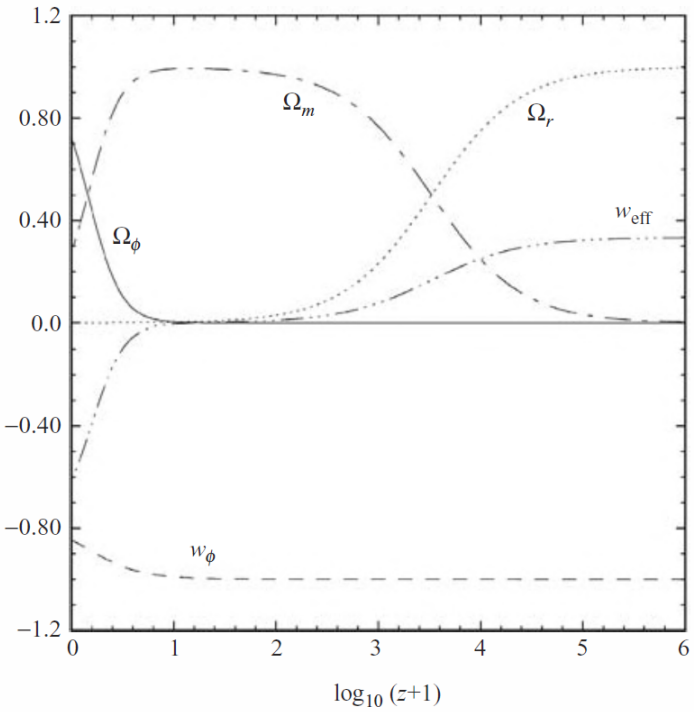

Figure 3.2: Evolution of Ω_ϕ, Ω_m, Ω_r, and w_ϕ for the dilatonic ghost condensate model with $\lambda = 0.2$ versus the redshift z. Initially the equation of state w_ϕ is close to -1 but deviates from -1 in the low-redshift regime. From [11].

3.5 Coupled Dark Energy

Because the energy density of the (dark) matter and the dark energy are of the same order in the present Universe there may be some relation between them. The coupling between dark matter and scalar field is described via modified energy conservation equations. This coupling is of the form, for instance [7]

$$\begin{aligned} \nabla_\mu T^\mu_{\nu(\phi)} &= +CT_M \nabla_\nu \phi, \\ \nabla_\mu T^\mu_{\nu(M)} &= -CT_M \nabla_\nu \phi, \end{aligned} \tag{3.29}$$

with coupling C and trace of the energy-momentum tensor $T_M = -\rho_M + 3p_M$. Since the radiation is traceless, the coupling term with radiation vanishes and the scalar field couples only to non-relativistic matter such as dark matter and baryons. Generally the coupling strength C is different for baryons and dark matter, but since baryons are subdominant component of the Universe, their coupling to dark energy makes only a small difference. Therefore for simplicity it is discussed here the case with only a single fluid with universal coupling.

Dark energy with interactions of the form of (3.29) with a constant coupling C arises in Brans-Dicke theory after a conformal transformation to the Einstein frame.

In the flat FLRW background the field ϕ, non-relativistic matter and radiation

with interaction (3.29) obey the equations of motion

$$\begin{aligned} \dot{\rho}_m + 3H\rho_m &= +C\rho_m\dot{\phi}, \\ \dot{\rho}_\phi + 3H(\rho_\phi + p_\phi) &= -C\rho_m\dot{\phi}, \\ \dot{r}_m + 4H\rho_r &= 0, \end{aligned} \tag{3.30}$$

which can be rewritten for the scalar field with potential $V(\phi)$ as

$$\ddot{\phi} + 3H\dot{\phi} + V_{,\phi} = -C\rho_m. \tag{3.31}$$

For the exponential field potential $V(\phi)$

$$V(\phi) = V_0 e^{-\lambda\phi} \tag{3.32}$$

with $\lambda^2 < 2$ an attractor causing accelerated expansion of the Universe can be found. During the matter dominated era the scalar field has a finite and almost constant energy density. This field-matter-dominated era between the radiation era and the accelerated era is called ϕMDE. The ϕMDE is responsible for most of the differences with respect to the uncoupled quintessence model – e.g. the evolution of the Hubble parameter (and hence different sound horizon) or equations for perturbations (which lead to a larger growth rate of matter perturbations). The ϕMDE is characterized by

$$\begin{aligned} \Omega_\phi &= \frac{2M_{pl}^2 C^2}{3}, \\ w_\phi &= 1, \\ w_{\text{eff}} &= \frac{2M_{pl}^2 C}{3}. \end{aligned} \tag{3.33}$$

Once the the attractor is reached, matter density becomes zero and the Universe is characterized by

$$\begin{aligned} \Omega_\phi &= 1, \\ w_\phi &= \frac{\lambda^2}{3} - 1, \\ w_{\text{eff}} &= \frac{\lambda^2}{3} - 1. \end{aligned} \tag{3.34}$$

The CMB data constrain the coupling constant to be $|C| < 0.1 M_{pl}^{-1}$ [10]

3.6 Chameleon Gravity

If there is a scalar field coupled to a non-relativistic matter with the interaction as strong as gravity, the coupling must be tuned to a small value to satisfy tests of the equivalence principle in Solar System which exclude any fifth forces. However, this fine-tunning can be avoided and the coupling can be of order of unity with the so called *chameleon mechanism*.

The action of a chameleon scalar field ϕ is given by the action (3.12) in the Einstein frame

$$S = \int \mathrm{d}^4x\sqrt{-g}\left[\frac{M_{pl}^2}{2}R - \frac{1}{2}(\partial\phi)^2 - V(\phi)\right] + S_m[\psi_m^{(i)}; g_{\mu\nu}^{(i)}]. \tag{3.35}$$

It is the same action as for the normal quintessence but now the matter fields are coupled to a metric $g^{(i)}_{\mu\nu}$, which is related to the Einstein frame metric $g_{\mu\nu}$ by a conformal transformation

$$g^{(i)}_{\mu\nu} = e^{2\beta_i\phi/M_{pl}} g_{\mu\nu}. \tag{3.36}$$

Varying the action (3.35) with respect to the field ϕ one can obtain the equation of motion

$$\Box\phi = V_{,\phi} - \sum_i \frac{\beta_i}{M_{pl}} e^{4\beta_i\phi/M_{pl}} g^{\mu\nu}_{(i)} T^{(i)}_{\mu\nu}, \tag{3.37}$$

where

$$T^{(i)}_{\mu\nu} \equiv \frac{-2}{\sqrt{-g}} \frac{\delta(\sqrt{-g}\mathcal{L}_m)}{\delta g^{\mu\nu}_{(i)}} \tag{3.38}$$

is the stress-energy tensor for the i-th matter component. Note that the stress-energy tensor defined in this way is **not** conserved in the Einstein frame, but rather in the Jordan frame, i.e.

$$\tilde{\nabla}_\mu T^{\mu\nu}_{(i)} = 0, \tag{3.39}$$

where $\tilde{\nabla}_\mu$ is the covariant derivative corresponding to the Jordan frame metric and we are assuming that the individual matter species do not interact with each other. The trace (not a scalar in the Einstein frame) of the i-th component is defined as $T^{(i)} \equiv g^{\mu\nu}_{(i)} T^{(i)}_{\mu\nu}$. For a perfect isentropic fluid is $T^{(i)} = -(1-3w_i)\tilde{\rho}_i$ with $\tilde{\rho}_i$ the energy density in the Jordan frame. The energy density defined as

$$\rho_i \equiv \tilde{\rho}_i e^{3(1+w_i)\beta_i\phi/M_{pl}}, \tag{3.40}$$

is conserved in the Einstein frame [118].

Equation of motion (3.37) is then

$$\Box\phi = V_{,\phi} + \sum_i (1-3w_i) \frac{\beta_i}{M_{pl}} \rho_i e^{(1-3w_i)\beta_i\phi/M_{pl}}. \tag{3.41}$$

This equation could be read as

$$\Box\phi = V_{\text{eff},\phi}\left(\phi\right), \tag{3.42}$$

where the effective potential V_{eff} is defined by

$$V_{\text{eff}}\left(\phi\right) \equiv V(\phi) + \sum_i \rho_i e^{(1-3w_i)\beta_i\phi/M_{pl}}. \tag{3.43}$$

If the couplings β_i are the same for each matter component with the same w (we can omit the radiation in the sum) and the overall density is $\rho = \sum_i \rho_i$, then the effective potential reads

$$V_{\text{eff}}\left(\phi\right) \equiv V(\phi) + \rho e^{(1-3w)\beta\phi/M_{pl}}. \tag{3.44}$$

For the quasi-static and weak ($\beta\phi/M_{pl} \ll 1$) field in a weak gravity background (the Minkowski background) with non-relativistic matter, the equation further simplifies as

$$\Delta\phi = \frac{\beta}{M_{pl}}\rho + V_{,\phi}, \tag{3.45}$$

which looks like the normal Poisson equation but with an extra non-linear term.

3.6.1 Chameleon Force

The interaction of the chameleon field with matter is described by the conformal coupling (3.36). As the matter fields $\psi_m^{(i)}$ couple to the metric $g_{\mu\nu}^{(i)}$ instead of $g_{\mu\nu}$, free test particles follow geodesics of $g_{\mu\nu}^{(i)}$

$$\frac{\mathrm{d}^2 x^\mu}{\mathrm{d}\tilde{\tau}^2} + \tilde{\Gamma}^\mu_{\alpha\beta}\frac{\mathrm{d}x^\alpha}{\mathrm{d}\tilde{\tau}}\frac{\mathrm{d}x^\beta}{\mathrm{d}\tilde{\tau}} = 0, \tag{3.46}$$

where $\tilde{\Gamma}^\mu_{\alpha\beta}$ are the Christoffel symbols of the metric $g_{\mu\nu}^{(i)}$. In the Einstein frame metric this gives [118]

$$\frac{\mathrm{d}^2 x^\mu}{\mathrm{d}\tau^2} + \Gamma^\mu_{\alpha\beta}\frac{\mathrm{d}x^\alpha}{\mathrm{d}\tau}\frac{\mathrm{d}x^\beta}{\mathrm{d}\tau} = -\frac{\beta_i}{M_{pl}}\left(2\phi_{,\alpha}\frac{\mathrm{d}x^\alpha}{\mathrm{d}\tau}\frac{\mathrm{d}x^\mu}{\mathrm{d}\tau} + g^{\beta\mu}\phi_{,\beta}\right). \tag{3.47}$$

Note that the chameleon force violates the weak Equivalence Principle only if there exist two matter species with differing values of β_i. In the non-relativistic limit, a test particle of mass m of species i in a static chameleon field ϕ is moving under a force $\vec{F}_\phi$ given by

$$\frac{\vec{F}_\phi}{m} = -\frac{\beta_i}{M_{pl}}\vec{\nabla}\phi \tag{3.48}$$

3.6.2 Chameleon mechanism

As discussed in § 3.2.2 we need some sort of a screening mechanism to avoid Solar System tests of GR. It means as seen from (3.48) that the chameleon potential needs to approach some constant value in dense regions.

Suppose we have a background solution ϕ_∞ which minimizes the effective potential with $\rho = \rho_\infty$. For small fluctuations $\phi = \phi_\infty + \delta\phi$ and $\rho = \rho_\infty + \delta\rho$ we can linearized (3.45) to obain

$$\Delta\delta\phi = \frac{\beta}{M_{pl}}\delta\rho + m_\infty^2\delta\phi, \tag{3.49}$$

where

$$m_\infty^2 \equiv V_{,\phi\phi}(\phi_\infty). \tag{3.50}$$

Except for the screening term, which often could be neglected, the equation (3.49) has the same behavior as the Poisson equation for the Newtonian potential Φ_N. For a spherically symmetric density profile this gives solution

$$\phi = \phi_\infty + 2\beta M_{pl}\Phi_N(r)\, e^{-m_\infty r}. \tag{3.51}$$

As the objects in the background become more massive (larger and/or denser) the Newtonian potential grows larger (in magnitude) and so the deviation of ϕ from background solution ϕ_∞. At some point this deviation is no longer small and the potential term in (3.45) cannot be treated perturbatively. It starts canceling the first source term and eventually the field ϕ posses a new (constant) value which minimizes the effective potential inside an object.

This is the essence of the chameleon mechanism. Let us derive the mechanism in a more proper and exact way.

3.6.3 Chameleon Profile

To obtain the cosmic acceleration and chameleon behavior described above we need to choose a chameleon potential $V(\phi)$ with the right properties. As in the case of the quintessence field we need the slow-roll mechanism to provide the acceleration and therefore we need the potential where the field rolls down in a potential slope. To have a screening mechanism in (3.45) we need $V_{,\phi} < 0$ and so field rolls down in the positive direction. And finally to have a screening behavior of the field as in the case of the Yukawa potential we need a real mass of the field, i.e. $V_{,\phi\phi} > 0$.

These properties of the potential are commonly referred to as the potential of the *runaway* form:

1. $\lim_{\phi\to 0} V(\phi) = \infty$;
2. $V(\phi)$ is C^∞, bounded below;
3. $V_{,\phi} < 0$ and increasing;
4. $V_{,\phi\phi} > 0$ and decreasing.

Although the item 1. and boundedness from 2. are usually assumed as these kinds of potentials arise in in supersymmetric models, there are not necessary as we will see in the Chapter 4 where we will study the chameleon gravity in context of Hu-Sawicki $f(R)$ models.

Example of this runaway potential we have already seen in the quintessence models – the inverse power-law potential (3.19)

$$V(\phi) = M^{4+n}\phi^{-n} \ (n > 0). \tag{3.52}$$

Another example is the exponential potential

$$V(\phi) = M^4 \exp\frac{M^n}{\phi^n} \ (n > 0). \tag{3.53}$$

We wish to find a solution for spherically symmetric matter distributions of a single species of pressureless matter such that

$$\rho(r) = \begin{cases} \rho_c & r < R_c \\ \rho_\infty & r > R_c, \end{cases}$$

where $\rho_c > \rho_\infty$. Further we define ϕ_c and ϕ_∞ with their masses m_c and m_∞ (the masses of small fluctuations about ϕ_c and ϕ_∞) such as

$$\begin{aligned} V_{\text{eff},\phi}(\phi_c)_{|\rho=\rho_c} &\equiv 0 & m_c^2 &\equiv V_{\text{eff},\phi\phi}(\phi_c) \\ V_{\text{eff},\phi}(\phi_\infty)_{|\rho=\rho_\infty} &\equiv 0 & m_\infty^2 &\equiv V_{\text{eff},\phi\phi}(\phi_\infty). \end{aligned}$$

The effective chameleon potential for this configuration is shown in Figure 3.3. In the background with low density, the curvature of the potential is much shallower, corresponding to a light scalar that mediates a long range force. Inside the object of high density, the scalar acquires a large mass, and the force shuts off.

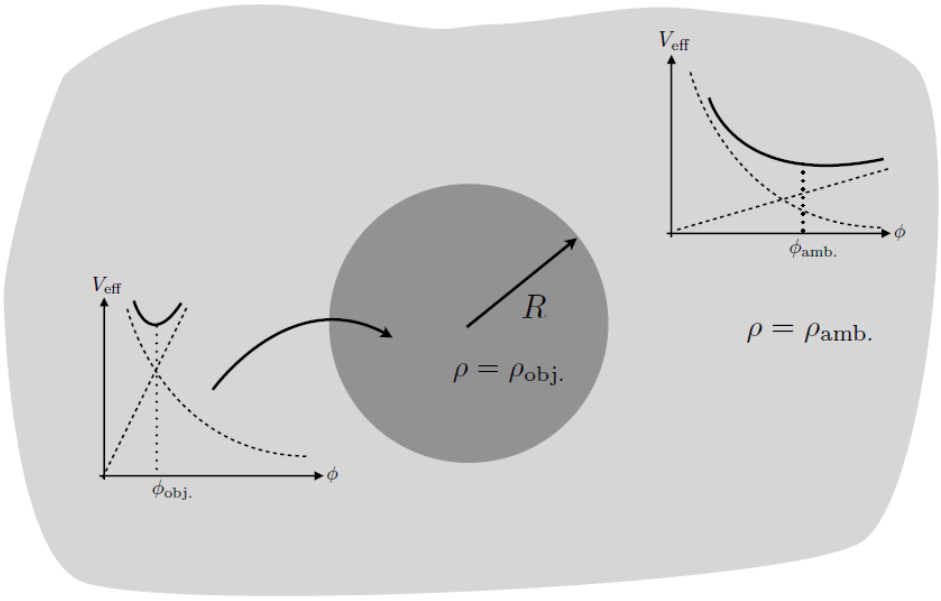

Figure 3.3: The effective chameleon potential for a massive spherical object of density $\rho_{\rm obj.}$ surrounded by the background with density $\rho_{\rm amb.}$. From [71].

In spherical coordinates assuming spherical symmetry, equation (3.45) becomes

$$\frac{\mathrm{d}^2\phi}{\mathrm{d}r^2} + \frac{2}{r}\frac{\mathrm{d}\phi}{\mathrm{d}r} = \frac{1}{r}\frac{\mathrm{d}^2\left(r\phi\right)}{\mathrm{d}r^2} = V_{,\phi}\left(\phi(r)\right) + \frac{\beta}{M_{pl}}\rho(r). \tag{3.54}$$

We must impose two boundary conditions which are

$$\frac{\mathrm{d}\phi}{\mathrm{d}r}(r=0) = 0$$
$$\phi(r\to\infty) = \phi_\infty.$$

The first one corresponds to a non-singularity of the solution at the origin while the later one ensures that the chameleon force vanishes at the infinity (as $\mathrm{d}\phi/\mathrm{d}r \to 0$).

The equation (3.54) drives the field ϕ toward the ϕ_∞ outside the object and toward ϕ_c inside the object. Note that the second term acts like the friction term.

In order to solve (3.54) we must do several approximations. Outside the object we assume that the field sits near the extreme ϕ_∞ and we can linearized our equation

$$\frac{1}{r}\frac{\mathrm{d}^2\left(r\phi\right)}{\mathrm{d}r^2} = m_\infty^2(\phi - \phi_\infty), \tag{3.55}$$

with the decaying solution

$$\phi(r) = -\frac{\beta}{4\pi M_{pl}}\frac{\tilde{M}}{r}e^{-m_\infty r} + \phi_\infty. \tag{3.56}$$

Note that the integration constant $\tilde{M}$ is not generally the mass of the object M_c as in the case of the Newtonian potential because it is determined by the field inside the object which has different behavior than the Newtonian potential. As we will see later, for small Newtonian potentials (in magnitude) this effective mass

$\tilde{M} \approx M_c$ but as the potential grows larger part of the object's mass is screened away $\tilde{M} < M_c$.

Inside the object we use one of the two approximations based on the initial value of $\phi_i \equiv \phi(0)$ – either $\phi_i \approx \phi_c$ or $\phi_i \gg \phi_c$.

Thin-shell regime

In the *thin-shell* regime the field initially sits very close the minimum ϕ_c, i.e. we require

$$(\phi_i - \phi_c)/\phi_c \ll 1. \tag{3.57}$$

The field is frozen near this value until the friction term is sufficiently small to allow the field to roll. This "moment" is denoted by R_{roll}. As soon as ϕ is displaced significantly from ϕ_c we may neglect the potential term in (3.54). This gives us the solution

$$\phi(r) = \begin{cases} \phi_c & 0 < r < R_{roll} \\ \frac{\beta}{6M_{pl}}\rho_c r^2 + \frac{A}{r} + D & R_{roll} < r < R_c. \end{cases} \tag{3.58}$$

We have boundary conditions coming from the requirement on matching ϕ and $\mathrm{d}\phi/\mathrm{d}r$ at R_{roll}, namely: $\phi = \phi_c$ and $\mathrm{d}\phi/\mathrm{d}r = 0$ at $r = r_{roll}$. This fixes our constants and the solution is

$$\phi(r) = \begin{cases} \phi_c & 0 < r < R_{roll} \\ \frac{\beta\rho_c}{3M_{pl}}\left(\frac{r^2}{2} + \frac{R_{roll}^3}{r}\right) - \frac{\beta\rho_c R_{roll}^2}{2M_{pl}} + \phi_c & R_{roll} < r < R_c. \end{cases} \tag{3.59}$$

The approximation of separating the solution into the two regions only makes sense if $(R_c - R_{roll})/R_c \ll 1$. Otherwise there is no clear separation between the two regions, and one needs a solution valid over the entire range $0 < r < R_c$. In Chapter 4 is (3.54) solved numerically and we can check these approximations against numerical solutions.

With approximation $(R_c - R_{roll})/R_c \ll 1$ we can determines the effective mass of the object $\tilde{M}$ from the requirement $\phi(R_c^-) = \phi(R_c^+)$ and $\mathrm{d}\phi/\mathrm{d}r(R_c^-) = \mathrm{d}\phi/\mathrm{d}r(R_c^+)$.

$$\tilde{M} = \frac{3\Delta R_c}{R_c} M_c, \tag{3.60}$$

where

$$\frac{\Delta R_c}{R_c} \equiv \frac{\phi_\infty - \phi_c}{6\beta M_{pl}|\Phi_N(R_c)|} \approx \frac{R_c - R_{roll}}{R_c} \ll 1. \tag{3.61}$$

This qualitative derivation of the thin-shell regime is using too much strong assumptions and can be done more precisely without ignoring some of the terms but then it is harder to see the principle of the thin-shell effect. For more details see e.g. [108], [81], [118].

Thick-shell regime

In the *thick-shell* regime the field is initially sufficiently displaced from the minimum – $\phi_i \gg \phi_c$ that it begins to roll almost immediately (no friction term). Hence the interior solution is most easily obtained by taking the $R_{roll} = 0$ in (3.59) and replacing ϕ_c by ϕ_i

$$\phi(r) = \frac{\beta\rho_c r^2}{6M_{pl}} + \phi_i \quad 0 < r < R_c. \tag{3.62}$$

By matching the interior and exterior solutions, we obtain

$$\begin{aligned} \phi_i &= \phi_\infty - 3\beta M_{pl}\Phi_N(R_c) \\ \tilde{M} &= M_c, \end{aligned} \tag{3.63}$$

which is the linear regime with no screening. From the definition of $\Delta R_c/R_c$ we also obtain

$$\frac{\Delta R_c}{R_c} \equiv \frac{\phi_\infty - \phi_c}{6\beta M_{pl}|\Phi_N(R_c)|} > 1. \tag{3.64}$$

Thin-shell suppression factor

The chameleon force outside the object (where experiments take place) comparing to the Newtonian force is

$$\begin{aligned} \frac{F_{thick}}{F_N} &= 2\beta^2 \\ \frac{F_{thin}}{F_N} &= 2\beta^2 \frac{3M_{pl}\left(\phi_\infty - \phi_c\right)}{\beta\rho_c R_c^2}, \end{aligned} \tag{3.65}$$

where we ignore the term $m_\infty r \ll 1$. Therefore for the coupling β of order unity the chameleon force is as strong as gravity unless it is screened away by the thin-shell effect.

3.7 Unified Dark Energy and Dark Matter

Despite the fact that dark matter and dark energy have different equations of state and completely different clustering properties there have been many attempts to unify them into a single entity. This can be done using either a single fluid or a single scalar field.

3.7.1 Generalized Chaplygin Gas Model

The Chapligin[5] gas model has been proposed in 2001 in order to explain the cosmic acceleration [73]. The so-called generalized Chaplygin gas is a a perfect fluid having the following equation of state:

$$p = -\frac{A}{\rho^\alpha}, \tag{3.66}$$

A is a positive constant. The choice $\alpha = 1$ corresponds to the original Chaplygin gas model which is now completely ruled out. This equation has a connection with the string theory and it can be obtained from the Nambu-Goto action for d-branes moving in a $(d+2)$-dimensional spacetime in the lightcone parametrization. For $\alpha > 0$, the pressure is suppressed by the energy density in the early universe and the Chaplygin gas acts like pressureless matter. At late times the negative pressure becomes important and the Chaplygin gas acts like dark energy realizing the cosmic acceleration.

[5]Named after Sergey Chaplygin (1869–1942), Russian mathematician, physicist, and engineer, who found a similar behavior in aerodynamical studies.

From the energy conservation equation and the equation of state (3.66) follows

$$\rho(t) = \left[A + \frac{B}{a^{3(1+\alpha)}}\right]^{1/(1+\alpha)}, \tag{3.67}$$

where B is an integration constant.

The density then evolves as $\rho \propto a^{-3}$ in the early epoch when $a \ll 1$ and as $\rho \propto A^{1/(1+\alpha)}$ in the late epoch when $a \gg 1$. The later solution $\rho \approx const$ corresponds to the de Sitter Universe.

At the background level the Chaplygin gas can explain both dark matter and dark energy. However, at the perturbation level the sound speed becomes large at the late epoch which leads to growth of inhomogeneities. The observations constrain the values of $|\alpha| \lesssim 10^{-5}$ [100]. It is difficult for this model to have suppressed role of the pressure during most of the matter era (for a successful structure formation) while a large negative pressure at the late time (for cosmic acceleration).

3.7.2 K-essence

As an unified model of dark energy and dark matter can also serve a single field with a purely kinetic Lagrangian density

$$\mathcal{L}_K = P(X). \tag{3.68}$$

Let us take a function $P(X)$ with an extremum at some value $X = X_0$. If the field sits near the extremum, such as holds the condition

$$\epsilon \equiv \frac{X - X_0}{X_0} \ll 1, \tag{3.69}$$

the function $P(X)$ can be expanded around this extremum:

$$P(X) = P_0 + P_2(X - X_0)^2. \tag{3.70}$$

The continuity equation in the flat FLRW spacetime yields

$$(P_{,X} + 2XP_{,XX})\dot{X} + 6HP_{,X}X = 0. \tag{3.71}$$

Then substituting (3.69) into (3.71) and calculating up to the linear order we obtain

$$\dot{\epsilon} = -3H\epsilon. \tag{3.72}$$

This gives the following solution

$$X = X_0\left[1 + \epsilon_1(a/a_1)^{-3}\right], \tag{3.73}$$

where ϵ_1 and a_1 are constants. The condition (3.69) translates into

$$\epsilon_1(a/a_1)^{-3} \ll 1. \tag{3.74}$$

The equation of state for k-essence as the unified model is

$$w_K = -\left[1 + \frac{4P_2}{P_0}X_0^2\epsilon_1\left(\frac{a}{a_1}\right)^{-3}\right]^{-1}, \tag{3.75}$$

which approaches $w_K \to 0$ during the early epoch and $w_K \to -1$ at the late epoch.

Unlike in the case of the Chaplygin gas model, the sound speed of the k-essence

$$c_s^2 = \frac{1}{2}\epsilon_1 \left(\frac{a}{a_1}\right)^{-3} \tag{3.76}$$

is always $c_s^2 \ll 1$ and thus is compatible with the observations of large-scale structure.

3.8 $f(R)$ Gravity

Until now we considered the dark energy as a modification of the right-hand side of the Einstein equations – adding some kind of exotic matter or extra scalar fields. We can also change the left-hand side of the Einstein equations and consider the modification of gravity itself. One of the simplest modified gravity models is the so-called $f(R)$ gravity in which we consider general functions of the Ricci scalar R in the action

$$S = \frac{M_{pl}^2}{2}\int \mathrm{d}^4x\sqrt{-g}\,[F(R)] + S_m[\psi_m; g_{\mu\nu}], \tag{3.77}$$

where $\S_m$ is the action of matter fields and $F(R) = R + f(R)$ is an arbitrary function of the Ricci scalar. The matter fields ψ_m obey standard conservation equations and therefore the metric $g_{\mu\nu}$ corresponds to the physical frame (which here is the Jordan frame).

Variation with respect to the metric[6] $g^{\mu\nu}$ gives us equation of motion (for more details see § A.4)

$$F_{,R}R_{\mu\nu} - \frac{1}{2}Fg_{\mu\nu} + g_{\mu\nu}\Box F_{,R} - \nabla_\mu\nabla_\nu F_{,R} = \frac{1}{M_{pl}^2}T_{\mu\nu}. \tag{3.78}$$

For $f(R) = -2\Lambda$ the Einstein gravity is reconstructed. Taking the trace of (3.78) we get

$$3\Box F_{,R} + F_{,R}R - 2F = \frac{1}{M_{pl}^2}T. \tag{3.79}$$

We see that there is a propagating scalar degree of freedom, so-called *scalaron* $\Psi \equiv F_{,R}$ with mass $m_\Psi^2 = F_{,R}/(3F_{,RR})$, which corresponds to the scalar field conformally coupled to matter in the Einstein frame.

To get the inflation we need a solution that approaches the de Sitter solution characterized by vacuum space with with a constant positive curvature. Thus $\Box F_{,R} = 0$ and (3.79) becomes

$$F_{,R}R - 2F = 0. \tag{3.80}$$

[6]In this co-called metric formalism used to derive field equations, the connections $\Gamma^\alpha_{\beta\gamma}$ have the usual definition in terms of the metric $g_{\mu\nu}$. There can be also used another approach, the so-called Palatini formalism in which $\Gamma^\alpha_{\beta\gamma}$ and $g_{\mu\nu}$ are treated as independent variables. In General Relativity these two approaches give the same results but not in $f(R)$ gravity. In the Palatini formalism the field equations is of the second order, unlike the fourth-order equations in the metric case. Hence the scalar-field degree of freedom does not have a dynamical evolution as in the case of General Relativity [11].

For example the model $f(R) = \alpha R^2$ gives rise to an asymptotically exact de Sitter solution and can be responsible for the inflation in the early Universe. The inflation ends when the quadratic term becomes smaller than the linear term. As at the present epoch is the curvature very small this model is not suitable to realize the present cosmic acceleration. Models like $f(R) = -\alpha/R^n$ with $\alpha > 0,\ n > 0$ could in principle give rise to the present acceleration. However, these models do not satisfy local gravity constraints because of the instability associated with negative values of $f_{,RR}$. Moreover, the standard matter epoch is not present because of a large coupling between the Ricci scalar and the non-relativistic matter.

There are four conditions for the viability of $f(R)$ models [9]

- $F_{,R} > 0$ $(R > R_0)$, where R_0 is the Ricci scalar at the present epoch,
  –required to avoid anti-gravity [11]

- $F_{,RR} > 0$ $(R > R_0)$,
  –required for consistency with local gravity tests [57], for the presence of the matter-dominated epoch [8] and for the stability of cosmological perturbations [105]

- $f(R) \to -2\Lambda$ $(R \gg R_0)$,
  –required for consistency with local gravity tests [111] and for the presence of the matter-dominated epoch [9]

- $0 < \frac{RF_{,RR}}{F_{,R}} < 1$ $(F_{,R}R - 2F = 0)$.
  –required for the stability of the late-time de Sitter solution [83]

Some examples of $f(R)$ models that satisfy these conditions:

$$f(R) = -\mu R_c (R/R_c)^p \qquad \text{for } 0 < p < 1;\ \mu, R_c > 0, \tag{3.81}$$

$$f(R) = -\mu R_c \frac{(R/R_c)^{2n}}{(R/R_c)^{2n} + 1} \qquad \text{for } n, \mu, R_c > 0, \tag{3.82}$$

$$f(R) = -\mu R_c \left[1 - (1 + R^2/R_c^2)^{-n}\right] \qquad \text{for } n, \mu, R_c > 0, \tag{3.83}$$

$$f(R) = -\mu R_c \tanh(R/R_c) \qquad \text{for } \mu, R_c > 0. \tag{3.84}$$

One of the main prediction of $f(R)$ gravity is different structure formation history than in ΛCDM. For the large-scale structure formation on subhorizon scales $k \gg H$ in quasi-static approximation one gets the modified equation for matter density perturbation [20]

$$\ddot{\delta}_m + 2H\dot{\delta}_m - 4\pi G_{\text{eff}} \rho_m \delta_m \approx 0, \tag{3.85}$$

where the effective gravitational constant is defined by

$$G_{\text{eff}} \equiv \frac{G}{1 + f_{,R}} \frac{4k^2 + 3a^2 m_\Psi^2}{3k^2 + 3a^2 m_\Psi^2}. \tag{3.86}$$

On scales much larger than the scalaron Compton wavelength m_Ψ^{-1}, gravity is unmodified aside from the overall reduction factor $f_{,R}$. However, on smaller scales

the gravitational coupling increases by the factor 4/3. As the scalaron mass m_Ψ and the factor $f_{,R}$ depend on curvature (local density), the chameleon mechanism discussed earlier can prevent the detection of this effect in the Solar System.

3.9 Other Models of Modified Gravity

The list of possible modifications of gravity is nearly endless so in this section we just briefly introduce some of them with references for further reading.

3.9.1 Gauss-Bonnet Dark Energy Models

In $f(R)$ gravity one adds general function of the Ricci scalar. But in principle one can add general functions of the Ricci and Riemann tensors as well, e.g. $f(R, R_{\mu\nu}R^{\mu\nu}, R_{\alpha\beta\gamma\delta}R^{\alpha\beta\gamma\delta}, ...)$ [33]. These Lagrangians are generally plagued by the existence of ghosts. However, there exists a combination of Ricci and Riemann tensors that keeps the equations at second-order in the metric and does not necessarily give rise to instabilities – so-called Gauss-Bonnet term $\mathcal{G}$ coupled to a scalar field

$$\mathcal{G} \equiv R^2 - 4R_{\mu\nu}R^{\mu\nu} + R_{\alpha\beta\gamma\delta}R^{\alpha\beta\gamma\delta}. \tag{3.87}$$

The Gauss-Bonnet term is the unique invariant for which the highest (second) derivative occurs linearly in the equations of motion and thus ensuring the uniqueness of solutions. The Gauss-Bonnet term naturally arises as a correction to the tree-level action of low-energy effective string theories [76]. The starting action is given by

$$S = \int \mathrm{d}^4x\sqrt{-g}\left[\frac{M_{pl}^2}{2}R - \frac{\gamma}{2}\left(\nabla\phi\right)^2 - V(\phi) + f(\phi)\mathcal{G}\right], \tag{3.88}$$

where $\gamma = \pm 1$ ($+1$ for the canonical scalar). For more details see [88][85][29].

3.9.2 Braneworld Models

In the braneworld model of Dvali, Gabadadze and Porrati (DGP model) [44] the 3-brane is embedded in a Minkowski bulk spacetime with infinitely large extra dimensions. The theory gives rise to the correct 4D potential at short distances whereas at large distances the potential is that of a 5D theory. The action of the theory is

$$S = \frac{M_{(5)}^3}{2}\int \mathrm{d}^5X\sqrt{-\tilde{g}}\tilde{R} + \frac{M_{pl}^2}{2}\int \mathrm{d}^4x\sqrt{-g}R + \int \mathrm{d}^4x\sqrt{-g}\mathcal{L}_m, \tag{3.89}$$

where $g_{AB}(X) = g_{AB}(x, y)$ denotes a 5D metric for which the 5D Ricci scalar is $\tilde{R}$ and $M_{(5)}$ is the 5D Planck mass. Capital letters are used for 5D quantities $(A, B = 0, 1, 2, 3, 5)$. The brane is located at $y = 0$. The induces 4D metric on the brane is denoted by

$$g_{\mu\nu}(x) \equiv \tilde{g}_{\mu\nu}(x, y = 0). \tag{3.90}$$

The cross-over scale r_0 is defined by

$$r_0 \equiv \frac{M_{pl}^2}{2M_{(5)}^3}. \tag{3.91}$$

At short distances $r \ll r_0$ gravity behaves as usual 4D theory, i.e the gravitational potential has correct $1/r$ behavior (except small logarithmic repulsion term). On the other hand at large distances $r \gg r_0$ the potential scales as $1/r^2$ in accordance with laws of 5D theory.

The presence of the extra dimension has severe consequences on the cosmology as well. It can be shown ([11][82]) that the matter dominated Universe approaches the de Sitter solution $H = r_0^{-1}$. This cosmological solution drives our Universe into the self-inflationary regime without dark energy. From $H_0 \approx r_0^{-1}$ we get $M_{(5)} \approx 10 - 100$ MeV.

3.9.3 Massive Gravity

The idea to give a mass to the graviton (infrared modification of gravity) is not new and has been investigated since the first years of General Relativity. It is a less minimal theory than $f(R)$ theories or modified gravities with an extra scalar field because it introduces three new degrees of freedom rather than one. By giving a mass m to the graviton we deform the classical potential to the Yukawa profile $\sim \frac{1}{r}e^{-mr}$ which departs from the classical one at distances $r > 1/m$. By choosing the graviton mass to be of the order of the Hubble constant $m \sim H$ one can hope to explain the acceleration of the universe without dark energy.

The simplest theory for a non-self-interacting massive graviton is Fierz-Pauli theory [54]. The action for a single massive spin 2 particle in flat space, carried by a symmetric tensor field $h_{\mu\nu}$ is

$$\begin{aligned} S = \int \mathrm{d}^4x \Big[&- \frac{1}{2}\partial_\lambda h_{\mu\nu}\partial^\lambda h^{\mu\nu} + \partial_\mu h_{\nu\lambda}\partial^\nu h^{\mu\lambda} - \partial_\mu h^{\mu\nu}\partial_\nu h \\ &+ \frac{1}{2}\partial_\lambda h \partial^\lambda h - \frac{1}{2}m^2\left(h_{\mu\nu}h^{\mu\nu} - h^2\right)\Big] + S_m. \end{aligned} \tag{3.92}$$

Any other combination of $h_{\mu\nu}h^{\mu\nu}$ and h^2 would lead to instabilities. Varying the action with respect to $h_{\mu\nu}$ yields the equation of motion

$$R_{\mu\nu} - \frac{1}{2}Rg_{\mu\nu} + \frac{1}{2}m^2(h_{\mu\nu} - h\eta_{\mu\nu}) = \frac{1}{M_{pl}^2}T_{\mu\nu}, \tag{3.93}$$

where all quantities are linearized around $\eta_{\mu\nu}$.

Because of the so-called vDVZ discontinuity ("van Dam-Veltman-Zakharov") in the propagator of a graviton, the Fierz-Pauli theory leads to different physical predictions from those of GR regardless the mass of the graviton (even when $m \to 0$). The Vainshtein mechanism [117] allows in principle to get rid of the vDVZ discontinuity by introducing non-linear Fierz-Pauli gravity.

The Vainshtein mechanism is another example of the screening mechanism and restores the continuity with GR on scales below the so-called Vainshtein radius r_V, defined as

$$r_V \equiv (GM/m^4)^{1/5}. \tag{3.94}$$

Much below the Vainshtein radius, which grows as the graviton's mass approaches 0, only linear terms plays crucial role and the GR is restored.

More about the massive gravity and the Vainshtein mechanism see e.g. [62][15].

3.9.4 Acceleration without Dark Energy

So far we studied some kind of a dark energy – either in a form of an exotic matter or by modifying gravity itself. But this need for a dark energy as an explanation of the acceleration comes from our observations which are based on the presumption of the homogeneous and isotropic Universe. What we observe are different expansion rates at different distances rather than an increase in the expansion rate at all distances. But this can be caused by strong inhomogeneities in the distribution of matter rather than by an accelerating Universe.

Void models

The basic idea behind void models is that we live in the middle of a huge spherical region which is expanding faster because it is emptier than the outside. That means that the Universe as a whole does not accelerate but that we observe an *apparent* cosmic acceleration. The edge of this void should be located around $z \sim 0.3-0.5$, the value at which in the standard interpretation we observe the beginning of the acceleration. These models are described by the Lemaître-Tolman-Bondi (LTB) spherically symmetric metric – the generalization of a FLRW metric in which the expansion factor along the radial coordinate is different relative to the surface line element $\mathrm{d}\Omega^2$ [96][6].

The inhomogeneous LTB model matches to the supernovae data and the location of the first acoustic peak of CMB temperature power spectrum but cannot satisfactorily reproduce the entire CMB angular power spectrum [37]. The observed isotropy of the CMB radiation implies that we must live close to the center of the void – nearer than 15 Mpc [5]. Moreover, there is no valid mechanism at present to explain the formation of such huge inhomogeneities, let alone one with our Galaxy near the center.

Backreaction

Unlike the void models, which regard the acceleration as an apparent one, *backreaction* models try to explain the cosmic acceleration by arranging inhomogeneities so that the deviation from the FLRW metric can produce a real acceleration [107][97][80]. Because GR equations are non-linear, averaging the inhomogeneities and then solving the GR equations (which is the usual approach) is not the same as first solving the full (inhomogeneous) GR equations and then averaging them – the expected value of a non-linear function is not the same as the nonlinear function of the expected value.

Any large inhomogeneities must be conceal from our sight to fit observations. Strong peculiar velocities instead of strong density fluctuations can do this job, but there are strong constraints on peculiar velocities from e.g., the kinematic Sunyaev–Zel'dovich effect. Moreover, the accompanying anisotropy is another source of observable effects difficult to accommodate with current observations.

3.10 Summary

As we saw, there are many ways how to modify gravity and therefore many different theories of gravity. But how much are these theories different? How can we distinguish between them?

On the background level, all modified theories must be able to recover the standard ΛCDM model very accurately – to fit current data. As these data allow only small deviations from the standard model, the usual approach is to parametrized the dark energy with linear equation of state

$$w = w_0 + (1 - a)w_a, \tag{3.95}$$

i.e. on the background level all modified theories must behave (almost) the same. The main differences come with perturbations. All surveys focus on the perturbed level. Effects like BAO, CMB or the growth of structures, all of them come from the deviations from the smooth FLRW background. Introduction to the perturbation theory and ways to measure deviations from the standard model are in § A.2 and § A.3.

In order to distinguish between modified theories we must measure these effects. Different sound speed, form of coupling to matter or time evolution will lead to different prediction of these effects. It is expected that joint LSST BAO and WL can yield 0.5% level precision on comoving distances for $0.3 < z < 3$. The parameters of equation of state (3.95) should be measured with percent-level precision. Euclid's forecast for accuracies of w_0 and w_a are 2% and 10%.

4. Numerical Solutions to Chameleon Field

Within the DESC we cooperate mostly with the Argonne National Laboratory (ANL) in United States. ANL is a member institution of the LSST Corporation and a number of ANL staff members participates in the LSST DESC. The ANL group is interested in (modified) large-scale cosmological simulations. In cosmological simulations for the LSST, ANL planes to include a large number of models. Our contribution to the project is a research on the chameleon field (see § 3.6). Even though the term chameleon field sounds rather exotic, in a general scalar-field theory with a matter coupling and arbitrary self-interaction potential, there will generically be some values of the field about which the field theory exhibits a chameleon mechanism. Our task is to probe the chameleon mechanism on galactic scales.

In this chapter we study a chameleon behavior in regions where the analytical solutions do not exist. We start with a Hu-Sawicki $f(R)$ model of gravity and transform the original action into the Einstein frame to get a chameleon type of action. At first, we compare our numerical solution in a special case – planar slab in a vacuum – against the exact solution to get an idea about an accuracy of our algorithm. Then we apply our algorithm on more realistic cases – spherical object in a background (e.g. a star) and NFW halo. Next follows a section about N-body simulations. We discuss algorithms used in cosmological simulations with focus on FFT-based methods. Then we introduce problems concerning application of these methods on chameleon gravity. This chapter is concluded by the discussion of results and possible future tasks.

4.1 Hu-Sawicki $f(R)$ Models

We wish to study a class of $f(R)$ models that accelerates the expansion at the late epoch without a cosmological constant and satisfies both cosmological and Solar System tests. We are interested in the Hu-Sawicki $f(R)$ models [66]. The action of these models in the Jordan frame is

$$S = \frac{M_{pl}^2}{2} \int \mathrm{d}^4x \sqrt{-\tilde{g}} \left[\tilde{R} + f(\tilde{R}) \right] + S_m[\psi_m; \tilde{g}_{\mu\nu}], \tag{4.1}$$

where tildes now denote quantities in the Jordan frame and the $f(\tilde{R})$ is of the broken power law form

$$f(\tilde{R}) = -M^2 \frac{c_1 (\tilde{R}/M^2)^m}{c_2 (\tilde{R}/M^2)^m + 1} = -\frac{2\Lambda}{1 + (L^2\tilde{R})^{-m}}, \tag{4.2}$$

with $m > 0$. In the second step we just redefined constants (following [113]). This form of $f(\tilde{R})$ also satisfies all four conditions for the viability of $f(R)$ models described in § 3.8.

In the high curvature limit (as it is in high density regions such as the Solar System) this can be approximated by

$$f(\tilde{R}) = -\frac{2\Lambda}{1+(L^2\tilde{R})^{-m}} \approx -2\Lambda + \frac{2\Lambda}{(L^2\tilde{R})^m}. \tag{4.3}$$

In this limit we can also see that cosmological tests at high redshifts remain the same as in General Relativity.

We do not want to work with fourth-order field equations so we use the conformal transformation as described in § 3.2.1 to transform our action into the Einstein frame. Inserting (3.10) into (3.11) yields

$$S = \int \mathrm{d}^4x\sqrt{-g}\left[\frac{M_{pl}^2}{2}R - \frac{1}{2}(\partial\phi)^2 - V(\phi)\right] + S_m[\psi_m; e^{\beta\phi/M_{pl}}g_{\mu\nu}], \tag{4.4}$$

where $\beta = 1/\sqrt{6}$, the potential

$$V(\phi) \equiv \frac{M_{pl}^2}{2}\frac{f_{,\tilde{R}}\tilde{R} - f}{(1+f_{,\tilde{R}})^2} = \frac{M_{pl}^2}{2}\frac{2\Lambda - \frac{2\Lambda(1+m)}{\left(L^2\tilde{R}\right)^m}}{\left(1 - \frac{2\Lambda n}{\left(L^2\tilde{R}\right)^m\tilde{R}}\right)^2}, \tag{4.5}$$

and the field

$$\phi \equiv -M_{pl}\sqrt{\frac{3}{2}}\ln\left(1+f_{,\tilde{R}}\right) = -\frac{M_{pl}}{2\beta}\ln\left(1 - \frac{2\Lambda m}{\left(L^2\tilde{R}\right)^m\tilde{R}}\right). \tag{4.6}$$

In the high-curvature limit these expressions simplify as

$$\begin{aligned} V(\phi) &\approx M_{pl}^2\Lambda - \frac{M_{pl}^2\Lambda\,(1+m)}{\left(L^2\tilde{R}\right)^m}, \\ \phi &\approx \frac{M_{pl}}{2\beta}\frac{2\Lambda m}{L^{2m}\tilde{R}^{m+1}}. \end{aligned} \tag{4.7}$$

Inserting $\tilde{R} = \tilde{R}(\phi)$ into the potential we get

$$V(\phi) = M_{pl}^2\Lambda - \frac{M_{pl}^2\Lambda\,(1+m)}{L^{2m}}\left(\frac{L^{2m}}{2\Lambda m}\right)^{\frac{m}{m+1}}\left(\frac{2\beta\phi}{M_{pl}}\right)^{\frac{m}{m+1}}. \tag{4.8}$$

Now we reparametrize our constants: $L \to \Phi_s$ and define $n \equiv m/(m+1)$ $(0 < n < 1)$ to obtain

$$V(\phi) = M_{pl}^2\Lambda - \frac{\beta\rho_\infty}{nM_{pl}}\left(2\beta M_{pl}\Phi_s\right)^{1-n}\phi^n, \tag{4.9}$$

where ρ_∞ is the background density and Φ_s is the so-called screening potential (dimensionless). Derivative of the potential is

$$V_{,\phi}(\phi) = -\frac{\beta}{M_{pl}}\rho_\infty\left(\frac{2\beta M_{pl}\Phi_s}{\phi}\right)^{1-n} \tag{4.10}$$

and the effective potential is then

$$V_{\text{eff},\phi}(\phi) = \frac{\beta}{M_{pl}}\rho - \frac{\beta}{M_{pl}}\rho_\infty \left(\frac{2\beta M_{pl}\Phi_s}{\phi}\right)^{1-n}. \tag{4.11}$$

The value of the field in the minimum of the effective potential is

$$\phi_{\min}(\rho) = 2\beta M_{pl}\Phi_s \left(\frac{\rho_\infty}{\rho}\right)^{1/(1-n)} \equiv \phi_\infty \left(\frac{\rho_\infty}{\rho}\right)^{1/(1-n)}, \tag{4.12}$$

where in the second step we identify the background value of the field $\phi_\infty \equiv 2\beta M_{pl}\Phi_s$. The mass of the field in the minimum of the effective potential is

$$m^2(\phi_{\min}) \equiv V_{\text{eff},\phi\phi}(\phi_{\min}) = \frac{\beta}{M_{pl}}(1-n)\frac{\rho_\infty}{\phi_\infty}\left(\frac{\rho}{\rho_\infty}\right)^{\frac{2-n}{1-n}}. \tag{4.13}$$

In the above, the word "background" in the background density ρ_∞ and the field ϕ_∞ do not refer to the background of the Universe but rather to the surrounding of the field. For example, the chameleon field of a star in a galaxy would approach to the value given by the minimum of the effective potential with the density of the galaxy rather than the Universe. In this sense the screening potential Φ_s should be viewed as an effective screening potential. For a typical galaxy with density of five orders of magnitude greater than the Universe background density and for $n = 1/2$ this would result into $\Phi_{\text{gal}} = \Phi_s \cdot 10^{-10}$.

It is expected that quantum corrections from matter loops do not change the form of the matter coupling but can change the value of coupling strength β [114]. Therefore β can posses an arbitrary value. In numerical computation we are using the standard value $\beta = 1/\sqrt{6}$.

4.2 Numerical Solutions

We want to solve the equation (3.45) with the potential (4.10), i.e.

$$\Delta\phi = \frac{\beta}{M_{pl}}\rho - \frac{\beta}{M_{pl}}\rho_\infty \left(\frac{\phi_\infty}{\phi}\right)^{1-n}. \tag{4.14}$$

As it is a non-linear equation without an exact solution we need to solve it numerically. The main problem with this equation is that it is ill-conditioned and therefore any numerical computation must be treated carefully. This instability can be seen easily from the linearized equation around the value in minimum of the potential, $\phi = \phi_{\min} + \delta\phi$

$$\Delta\delta\phi = m^2(\phi_{\min})\delta\phi. \tag{4.15}$$

For a slowly varying m we have two solutions

$$\delta\phi \propto \frac{e^{\pm mr}}{r}. \tag{4.16}$$

Now, for either $r \to 0$ or $r \to \infty$ we need to fix integration constants to prevent the divergence of the solution. This is very hard to do numerically because every

small inaccuracy will eventually grow ad infinitum (exponentially). Therefore we cannot solve the equation (4.14) purely numerically but we need to use analytical solutions in highly unstable regions.

We will solve the equation (4.14) in special cases where the Poisson equation reduces to an ordinary differential equation of second order – a planar slab in a vacuum, a spherical object of a constant density in the background and the NFW halo.

4.2.1 Runge-Kutta Method with Adaptive Stepsize

For the integration of ordinary differential equations we use the Runge-Kutta method [95]. This method uses "trial" steps across the integration interval and then uses all of them (with appropriate weights) to compute the "real" step across the whole interval. The classical fourth-order Runge-Kutta formula is

$$\begin{aligned} k_1 &= hf(x_n, y_n) \\ k_2 &= hf(x_n + \frac{1}{2}h, y_n + \frac{1}{2}k_1) \\ k_3 &= hf(x_n + \frac{1}{2}h, y_n + \frac{1}{2}k_2) \\ k_4 &= hf(x_n + h, y_n + k_3) \\ y_{n+1} &= y_n + \frac{1}{6}k_1 + \frac{1}{3}k_2 + \frac{1}{3}k_3 + \frac{1}{6}k_4 + O(h^5) \end{aligned} \tag{4.17}$$

For a practical usage we need to make frequent changes in the stepsize of the algorithm. For example, inside and near the star we need many small steps to obtain the proper behavior of the chameleon. But when we are outside the star and the field behaves smoothly only few large steps are required to obtain the desired accuracy. As we will sometimes integrate our equations at very large radii (many orders of magnitude of a characteristic size of the system) this improvement in efficiency can be factors of hundred or more.

The most straightforward technique to implement the adaptive stepsize control is *step doubling*. We take each step twice, once as a full step, and then independently as two half-steps. If y is the exact solution and y_1 (one step $2h$) and y_2 (two steps of size h) are two approximate solutions, these are related by

$$\begin{aligned} y(x + 2h) &= y_1 + (2h)^5\phi + O(h^6) \\ y(x + 2h) &= y_2 + 2(h)^5\phi + O(h^6), \end{aligned} \tag{4.18}$$

where we assume ϕ to be constant over the step. The difference between the two numerical estimates is a indicator of the truncation error

$$\delta \equiv y_2 - y_1. \tag{4.19}$$

Note that δ is actual a vector. This can be used to improve the numerical estimate of the true solution but than we would loose the information about the error. We want to adjust the stepsize h so the error δ is neither too large (inaccurate solution) nor too small (slow algorithm). We define a scale

$$\texttt{scale = atol + |y|rtol}, \tag{4.20}$$

where `atol` is the absolute tolerance and `rtol` is the relative error tolerance. We define the error of the solution

$$\texttt{err} = \sqrt{\frac{1}{N}\sum_{i=0}^{N-1}\left(\frac{\delta_i}{\texttt{scale}_i}\right)^2}. \tag{4.21}$$

One can define the norm of δ arbitrary – as long as it scales as $\texttt{err} \propto \delta$ the algorithm remains unchanged. If this error $\texttt{err} \leq 1$ than we accept the step, otherwise reject it and decrease the stepsize. If this error is too small, on the contrary, we want to increase the stepsize to get a better efficiency. From (4.18) we see that the error scales as h^5 Thus we adjust the new step as

$$h_{n+1} = Sh_n\left(\frac{1}{\texttt{err}}\right)^{\frac{1}{5}}, \tag{4.22}$$

where S is a safety factor. Because the error scales only approximately as h^5 (in the leading order) by putting the safety factor $S \lesssim 1$ this ensures the desired accuracy. In our program we use $S = 0.9$. We also do not let the stepsize increase or decrease too fast, and not to let the stepsize increase at all if the previous step was rejected. In our algorithm the stepsize cannot increase by more than a factor of ten nor decrease by more than a factor of five in a single step.

4.2.2 Shooting Method

We are dealing with an ordinary differential equation of second order with two boundary conditions at **two different points**. The problem is that in this case we cannot just start with some fixed initial conditions at the begging of the integration and integrate the equations. For solving this two-point boundary value problem we will use the *shooting method* [95].

The shooting method is a bit like trial and error. At the initial point the one initial condition is fixed by the boundary conditions. We then *guess* the second initial condition, integrate our equations and try to match the boundary conditions at the end of the integration. This problem can be viewed as a root-finding problem.

At the initial time t_0 we have the condition $y_0(t_0) = b_0$ and at the end of the integration the condition $y_1(t_1) = b_1$. The second initial condition (which we guess) is denoted by s and $y_0(t_0; s) = b_0$ is satisfied. Then we define the function $F(s)$ as

$$F(s) \equiv y_1(t_1; s) - b_1. \tag{4.23}$$

If $F(s)$ has a root s_0 then s_0 is our required initial condition. As a *root-finding algorithm* we use the simplest method – the bisection method [95]. Methods based on derivative (secant method, Newton's method) are no use for our problem because the shooting functions for non-linear equations are not well behaved and have very large gradients.

The *shooting parameter* s does not have to be directly one of the initial conditions. We can choose some combination of $y(t_0)$ and $\dot{y}(t_0)$ (so-called Robinson boundary conditions) fixed by s or the initial time can be fixed by s. We simply need to have specified initial conditions for given s.

4.3 Planar Slab in Vacuum

4.3.1 Configuration

We want to check our algorithm against an exact solution first [112]. For that purpose we use the potential

$$V(\phi) = M_\Lambda^4 \left(1 + \gamma \left|\frac{\phi}{M_\Lambda}\right|^k\right), \tag{4.24}$$

with $M_\Lambda = 2.4 \cdot 10^{-3}$ eV, $\gamma > 0$. For $1 \leq k \leq 2$ the effective mass of the field does not increase with an increase of ρ and therefore cannot produce the chameleon behavior. Moreover, the range $-1/2 \lesssim k < 1$ is constrained by cosmology and therefore we restrict ourself only on $k \lesssim -1/2$ and $k > 2$. The minimum of the effective potential is at the value of the field

$$\phi_{\min}(\rho) = M_\Lambda \mathrm{sgn}(1-k) \left(\frac{\beta\rho}{|k|\gamma M_\Lambda^3 M_{pl}}\right)^{\frac{1}{1-k}}. \tag{4.25}$$

This potential has an exact solution in a vacuum outside an infinitely thick planar slab with density $\rho(z) = \rho_0\theta(-z)$, where $\theta(z)$ is the Heaviside step function. The equation of motion outside the slab, $\mathrm{d}^2\phi/\mathrm{d}z^2 = V_{,\phi}$, is solved by

$$\phi(z) = \phi_0 \left(1 + \sqrt{\frac{1}{2}(k-2)^2\gamma M^{4-k}\phi_0^{k-2}}\, z\right)^{-\frac{2}{k-2}} \equiv \phi_0 \left(1 + z/z_c\right)^{-\frac{2}{k-2}}, \tag{4.26}$$

where ϕ_0 is the field value on the surface of the slab ($z = 0$) . We defined the characteristic scale z_c for the solution (4.26) as

$$z_c^{-1} \equiv \sqrt{\frac{1}{2}(k-2)^2\gamma M^{4-k}\phi_0^{k-2}}. \tag{4.27}$$

Note that except prefactors of order k the scale z_c^{-1} is the same as $m_{\text{eff}}(\rho_0)$ – the chameleon Compton wavelength in the slab, and therefore it is truly the characteristic scale. From boundary conditions $\mathrm{d}\phi/\mathrm{d}z \to 0$ as $z \to \pm\infty$ and the requirement of a continuity at $z = 0$ one can show that

$$\phi_0 = \left(1 - \frac{1}{k}\right)\phi_{min}(\rho_0). \tag{4.28}$$

Inside the slab an exact solution does not exist and the numerical one is unstable as discussed earlier. Therefore we will test our algorithm only on the interval $(0, \infty)$.

First we use the initial conditions from the exact solution to test the accuracy of our integrator, i.e.

$$\begin{aligned} \phi(0) &= \phi_0 \\ \frac{\mathrm{d}\phi}{\mathrm{d}z} &= -\frac{2}{k-2}\frac{\phi_0}{z_c}. \end{aligned} \tag{4.29}$$

Next we will test the shooting algorithm. For that purpose we use one boundary condition $\phi(0) = \phi_0$. The second condition used in the analytical solution – $\mathrm{d}\phi/\mathrm{d}z\,(z \to \infty) = 0$ is not sufficient for our numerical solution. Because $\mathrm{d}\phi/\mathrm{d}z$ tends to zero very slowly we must choose a different condition. We use the behavior of the solution at large z, i.e.

$$\phi \propto z^{-\frac{2}{k-2}}, \tag{4.30}$$

which can be guess easily even without the knowledge of the exact solution. Taking a derivative we obtain the Robin boundary condition

$$\frac{\mathrm{d}\phi}{\mathrm{d}z} + \frac{2\phi}{(k-2)z} = 0, \tag{4.31}$$

which is valid for $z \gg z_c$. Comparing with the boundary condition from the exact solution at some z_{max} we see that the error of condition (4.31) scales as z_c/z_{max}.

We define an error

$$\delta_\phi \equiv \sqrt{\sum_{i=1}^{N} \frac{1}{N} \left(\frac{\phi_A(z_i) - \phi_N(z_i)}{\phi_A(z_i)} \right)^2}, \tag{4.32}$$

where ϕ_A is the analytical solution and ϕ_N is the numerical solution.

4.3.2 Numerical Results

We tested our algorithm against the potential (4.24) with following parameters

$$\begin{aligned} M_\Lambda &= 2.4 \cdot 10^{-3}\ \mathrm{eV} \\ \gamma &= 1 \\ \rho_0 &= 10^{-11}\ \mathrm{eV}^4 \\ z_0 &= 0 \\ z_{max} &= 100 z_c \\ \texttt{atol} &= 10^{-10} \\ \texttt{rtol} &= 10^{-8} \end{aligned} \tag{4.33}$$

and various k. Let us first test the accuracy of our integrator. In Figure 4.1 are shown solutions for $k > 2$ and exact initial conditions. We see that except the case $k = 3$ our numerical solutions match the analytical pretty accurately. According to (4.32) we computed the errors as

$$\begin{aligned} \delta_\phi &= \infty && (k = 3) \\ \delta_\phi &= 6.7\% && (k = 4) \\ \delta_\phi &= 0.05\% && (k = 6) \\ \delta_\phi &= 0.009\% && (k = 8). \end{aligned}$$

We see that for larger k the error is decreasing while as k tends to two the problem is becoming more and more unstable. If we write our numerical solution as the analytical one plus a small deviation

$$\phi_N = \phi_A + \delta\phi, \tag{4.34}$$

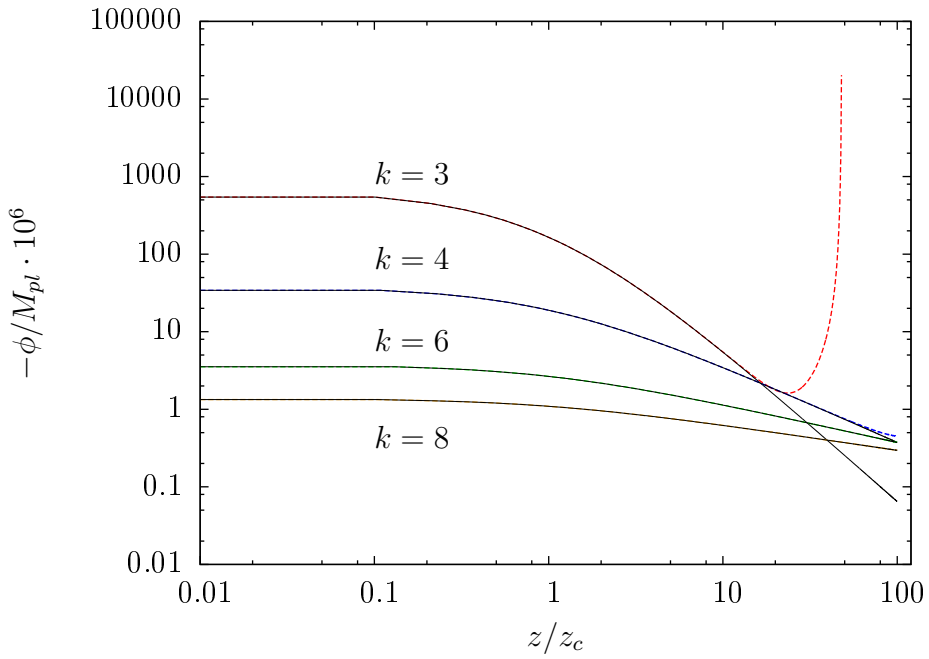

Figure 4.1: Numerical (dashed lines) and analytical (solid lines) solutions for the potential (4.24) with various $k > 2$. We use $\gamma = 1$ and $\rho_0 = 10^{-11}$ eV^4.

we can linearize the equation of motion and find

$$\delta\phi \propto (1 + z/z_c)^{\alpha_\pm}\,, \tag{4.35}$$

where

$$\alpha_\pm = \frac{1}{2}\left(1 \pm \frac{3k-2}{k-2}\right). \tag{4.36}$$

The non-decaying mode α_+ is getting worse as $k \to 2$. In order to get the correct solution we need to increase the accuracy of our integrator. In Figure 4.2 are shown numerical solutions for $k = 3$ and various `rtol`. This tells us how the numerical integration of non-linear equations can be problematic – even the slightest deviation can produce a disastrous behavior. Thus we should always use an analytical solution whenever it is possible and avoid the numerical integration over too large distances.

The computed errors come only from the large errors for higher z. We computed the error also for $z < 10z_c$:

$$\begin{aligned} \delta_\phi &= 1 \cdot 10^{-3} && (k = 3) \\ \delta_\phi &= 1 \cdot 10^{-5} && (k = 4) \\ \delta_\phi &= 7 \cdot 10^{-7} && (k = 6) \\ \delta_\phi &= 2 \cdot 10^{-7} && (k = 8). \end{aligned}$$

For the most stable case ($k = 8$) we see that we almost achieved the desired accuracy $\texttt{rtol} = 10^{-8}$. On even shorter distances this accuracy is truly achieved.

Next we tested our shooting algorithm. We used the same potential with parameters (4.33) but now with $k < -1/2$ (more stable). The Robin boundary

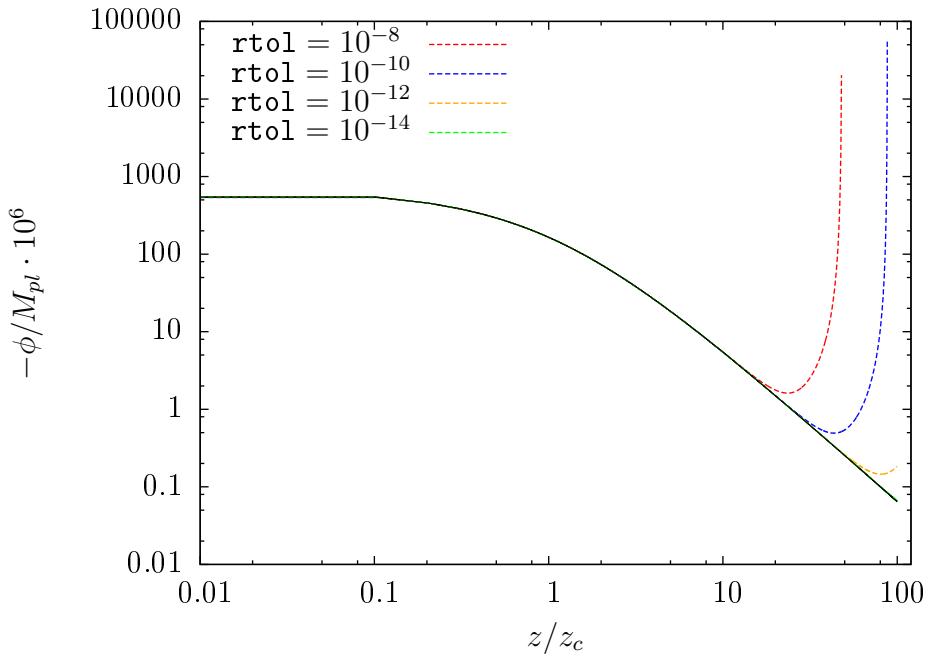

Figure 4.2: Numerical (dashed lines) and analytical (solid line) solutions for the potential (4.24) with $k = 3$ and various tolerances of relative error. We use $\gamma = 1$ and $\rho_0 = 10^{-11}$ eV^4.

condition (4.31) is used. In Figure 4.3 are shown these solutions with errors

$$\begin{aligned} \delta_\phi &= 2.1\% \quad (k = -1) \\ \delta_\phi &= 1.2\% \quad (k = -2) \\ \delta_\phi &= 0.5\% \quad (k = -4) \\ \delta_\phi &= 0.4\% \quad (k = -8). \end{aligned}$$

Note that for $z_{max} = 100 z_c$ the error of the boundary condition is 1% and therefore the shooting algorithm works satisfactorily.

4.4 Stars

Next we will consider a more realistic case – a compact spherical object of constant density ρ_c surrounded by the background of density ρ_∞ as discuss in § 3.6.3. This can be an approximate model of a star, globular clusters or a spherical overdensity on large scales. We remind here the used notation

$$\begin{aligned} V_{\text{eff},\phi}\left(\phi_c\right)_{|\rho=\rho_c} &\equiv 0 & m_c^2 &\equiv V_{\text{eff},\phi\phi}\left(\phi_c\right) \\ V_{\text{eff},\phi}\left(\phi_\infty\right)_{|\rho=\rho_\infty} &\equiv 0 & m_\infty^2 &\equiv V_{\text{eff},\phi\phi}\left(\phi_\infty\right). \end{aligned}$$

With the spherical symmetry the equation (4.14) becomes

$$\frac{\mathrm{d}^2\phi}{\mathrm{d}r^2} + \frac{2}{r}\frac{\mathrm{d}\phi}{\mathrm{d}r} = \frac{\beta}{M_{pl}}\rho(r) - \frac{\beta}{M_{pl}}\rho_\infty\left(\frac{\phi_\infty}{\phi}\right)^{1-n}. \tag{4.37}$$

We will use the potential with $n = 1/2$ which corresponds to the simplest Hu-Sawicki model $m = 1$. Note that this particularly choice affects the value

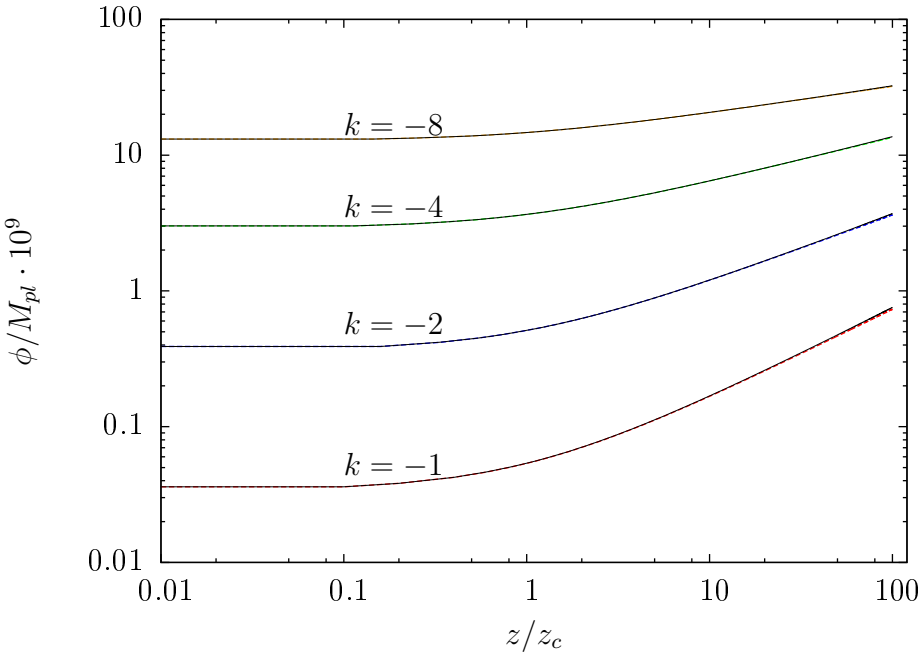

Figure 4.3: Numerical (dashed lines) and analytical (solid lines) solutions for the potential (4.24) with various $k < -1/2$. We use $\gamma = 1$ and $\rho_0 = 10^{-11}$ eV^4.

of the field in the minimum of the potential and also the effective mass of the field, but does not affect the qualitative description of the problem.

4.4.1 Expected Behavior

For a low-mass star we are in the thick-shell (linear) regime where the chameleon behaves like the Newtonian potential

$$\phi(r) = \phi_\infty + 2\beta M_{pl}\Phi_N e^{-m_\infty r} = 2\beta M_{pl}\left(\Phi_s + \Phi_N e^{-m_\infty r}\right). \tag{4.38}$$

The exponential factor could be neglected as long as $m_\infty r \ll 1$. As the object becomes more massive so grows (in magnitude) the potential Φ_N. Because we have $\phi > 0$, once the potential is large enough that $|\Phi_N| > \Phi_s$, the linear regime breaks down.

Next we will denote R_{eq} the *equivalence radius* – radius at which the Newtonian potential equals the screening potential $|\Phi_N(R_{eq})| = \Phi_s$. By letting the equivalence radius posses also negative values such as $(1 + |R_{eq}|/R_c)|\Phi_N(0)| = \Phi_s$ we can clearly distinguish between the linear ($R_{eq} < 0$) and the screening ($R_{eq} > 0$) regime.

When $R_{eq} > 0$ the field will be initially frozen near ϕ_c and starts to roll away at a radius $R_{roll} < R_{eq}$. If $R_{eq} < R_c$ we expect that the field manages to catch up the linearized solution still inside the object and there will be no screening outside the object. But when $R_{eq} \gtrsim R_c$ the field reaches the surface of the object with different value than expected from the linearized solution. Outside the object the field behaves like in the linearized case but now with a different amplitude and hence the screening occurs.

4.4.2 Boundary Conditions

Because of the numerical instabilities we must treat boundary conditions carefully. In the analytical solution the boundary conditions are $\mathrm{d}\phi/\mathrm{d}r(r=0)=0$ (from symmetry reasons) and $\phi(r)=\phi_\infty$ as $r\to\infty$. The boundary condition at the origin $r=0$ works fine in the linear regime ($R_{eq}<0$) when the solution is displaced enough from ϕ_c and we can use the shooting method to find $\phi(0)$. But when we enter the non-linear regime and the solution is very close to ϕ_c the numerical instabilities appear. In this case we must use an analytical method.

In this non-linear case we can find the linearized solution $\phi=\phi_c+\delta\phi$ near the origin with

$$\delta\phi = A\frac{e^{+m_c r}}{r} + B\frac{e^{-m_c r}}{r}. \tag{4.39}$$

We want to have a non-divergent solution at the origin so we choose $A=-B$ which automatically satisfies the boundary condition $\mathrm{d}\phi/\mathrm{d}r(r=0)=0$. Now we reparametrized the constant A such as at some radius R_{roll} the solution is $\delta\phi(r=R_{roll})=\epsilon\phi_c$, i.e.

$$\phi = \phi_c\left(1+\epsilon\frac{R_{roll}}{r}\frac{e^{+m_c r}-e^{-m_c r}}{e^{+m_c R_{roll}}-e^{-m_c R_{roll}}}\right). \tag{4.40}$$

The parameter ϵ ensures that in the region $0<r<R_{roll}$ we are close enough to the minimum of the effective potential and our linearized solution is valid. In numerical simulations we chose $\epsilon=0.01$. In the shooting method we now use the parameter R_{roll} as the shooting parameter and we start the integration at R_{roll} with initial conditions obtained from this linearized solution. This approach gets us through the most unstable region near the origin.

As the mass of the object grows the field starts to roll closer and closer to the surface $R_{roll}\to R_c$, until it enters the *no-shell* solution $R_{roll}=R_c$. In this limit the above method is unstable and gives wrong result. We must therefore use once again the analytical solution. With no shell the field is nearly frozen in the whole interior and starts to roll at the surface of the object with [108]

$$\begin{aligned}\phi(R_c) &= \phi_c + \frac{\phi_\infty-\phi_c}{m_c R_c}\frac{e^{m_c R_c}-e^{-m_c R_c}}{e^{m_c R_c}+e^{-m_c R_c}},\\ \frac{\mathrm{d}\phi}{\mathrm{d}r}(R_c) &= \frac{\phi_\infty-\phi_c}{r_c}\left[1-\frac{2}{m_c R_c\left(e^{m_c R_c}+e^{-m_c R_c}\right)}\right].\end{aligned} \tag{4.41}$$

The boundary condition at infinity $\phi(r)=\phi_\infty$ is bad in both linear and non-linear cases. As discussed earlier the existence of the non-decaying solution $\delta\phi\propto e^{m_\infty r}/r$ makes the integration at radii $r\gtrsim 1/m_\infty$ numerically difficult. We will use the analytical solution (which contains only the decaying mode) to get the condition

$$\frac{\mathrm{d}\delta\phi}{\mathrm{d}r} + \frac{1+m_\infty r}{r}\delta\phi = 0, \tag{4.42}$$

which is valid for $\delta\phi/\phi_\infty<\epsilon$. In our numerical simulations we chose $\epsilon=0.01$ and we integrate our equations till this condition is satisfied. Then we try to match the boundary condition (4.42) via the shooting method.

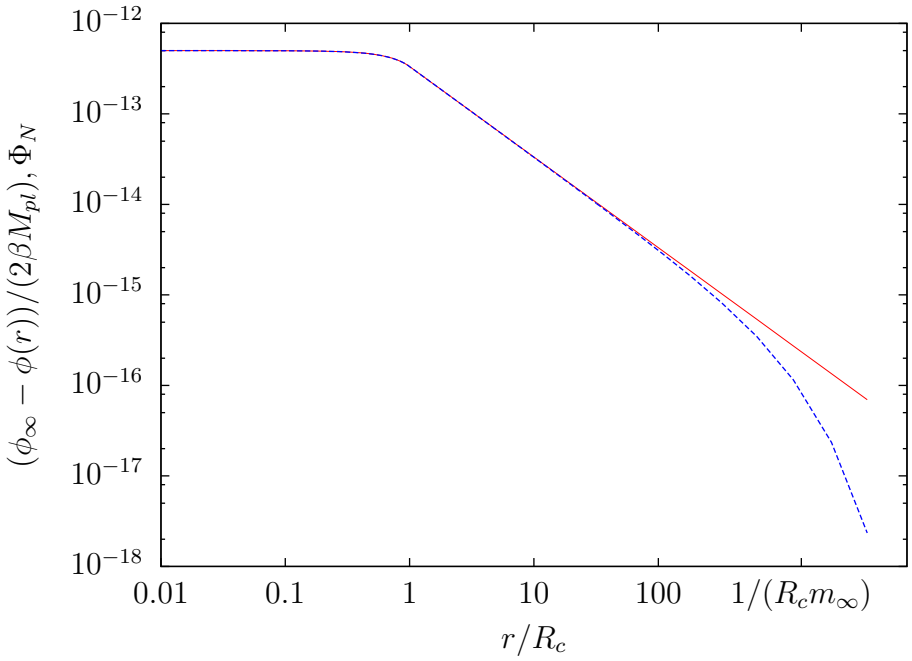

Figure 4.4: Chameleon field (blue dashed line) and Newtonian potential (red solid line) for a spherical object of constant density in the background. Chameleon field is in the linear regime $R_{eq} = -R_c$ with the screening potential $\Phi_s = 10^{-12}$.

4.4.3 Numerical Results

In Figure 4.4 is shown a numerical solution to the chameleon field in the linear regime – we set the screening potential $\Phi_s = 10^{-12}$ and adjust density so that the equivalence radius $R_{eq} = -R_c$. We also plot the Newtonian potential for comparison. We see that the chameleon field behaves like the Newtonian potential as we expected. Around $r \sim 1/m_\infty$ the chameleon behavior starts to deviates from the Newtonian and enters the exponentially damped phase.

In Figure 4.5 are shown numerical solutions for the chameleon field with the same mass of the object but with several screening potentials. The red solid line is a linear solution that tracks the Newtonian potential. The next two solutions are in a deep screening regime. We see (if approaching from the infinity) that these solutions behave like the Newtonian potential outside the star, but once they reach the "barrier" Φ_s at the surface of the star the field will freeze.

Let us now examine the screening inside the object more closely. For observations is not important the actual value of the field but rather the derivative – the chameleon force F_ϕ. In Figure 4.6 is plotted the force affecting a test particle compared to the Newtonian one as a function of a distance for several values of the screening potential and corresponding equivalence radii. We see that for $R_{eq} \ll R_c$ there is no screening outside the object, but as the R_{eq} grows (while still $R_{eq} < R_c$) the force is screened outside the object (in contradiction with our expectations). While inside a radius $R_{roll} < R_{eq}$ the force is exponentially damped.

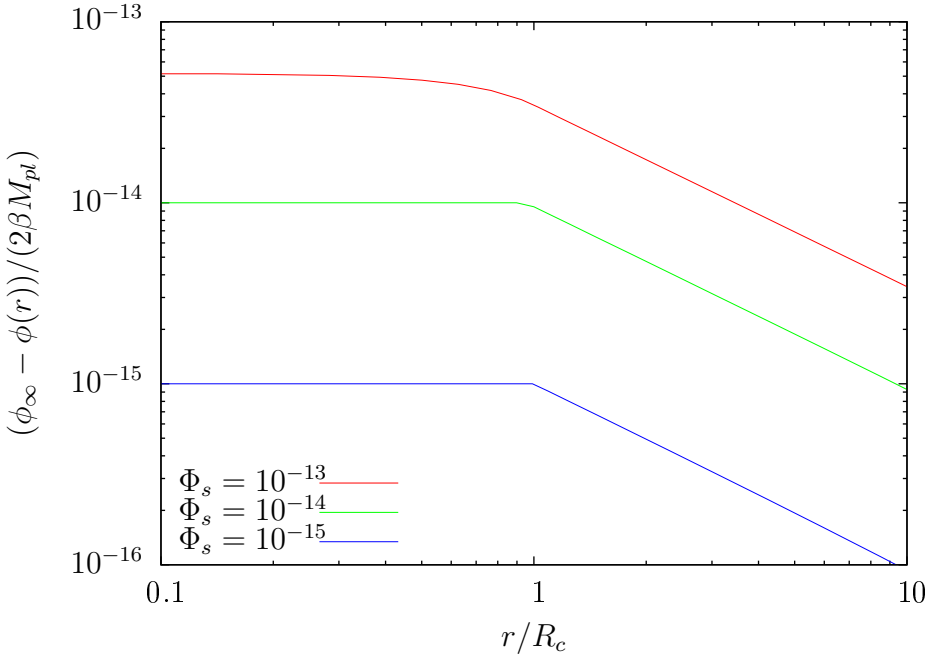

Figure 4.5: Chameleon field for several screening potentials with corresponding equivalence radii. The top solution is in the linear regime and the two last solutions correspond to the non-linear screened regime.

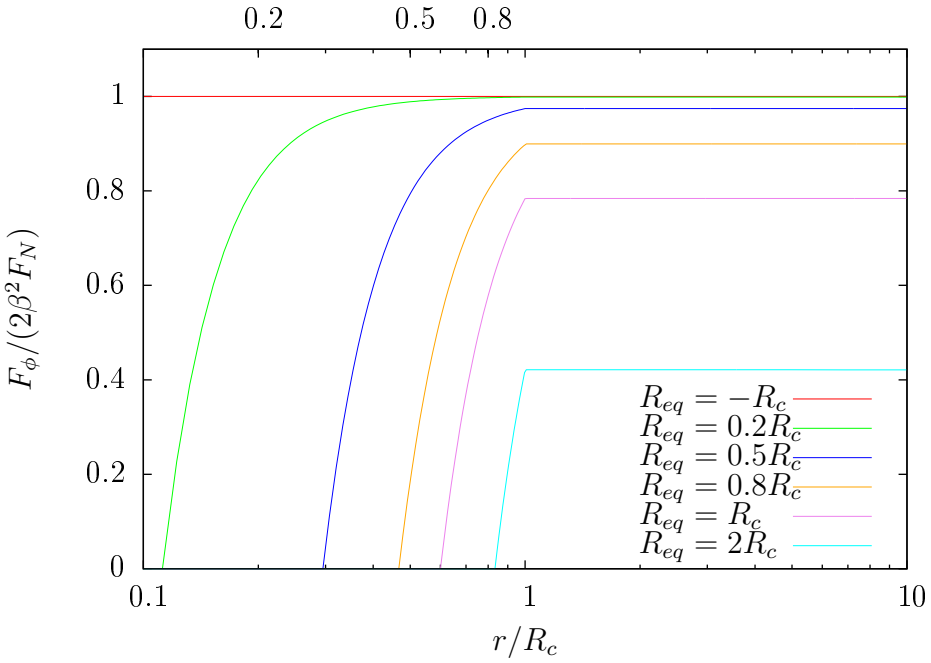

Figure 4.6: Chameleon force for several screening potentials with corresponding equivalence radii. For $R_{eq} \ll R_c$ there is no screening outside the object. As the R_{eq} grows, the screening occurs. While inside a radius $R_{roll} < R_{eq}$ the force is exponentially damped.

4.5 NFW Halo

The Navarro-Frenk-White (NFW) profile proposed in [84] describes the distribution of cold dark matter. The NFW profile of matter overdensity is given by

$$\delta\rho_{NFW}(r) = \frac{\rho_c}{r/r_s\,(1+r/r_s)^2}, \tag{4.43}$$

where ρ_c is the density scale and r_s is the scale radius. We will also be using the dimensionless radius $x \equiv r/r_s$. We use $\rho_c = 3 \cdot 10^{-5}$ eV^4 and $r_s = 10$ kpc $= 1.57 \cdot 10^{27}\text{eV}^{-1}$, if not stated otherwise. Total mass of the halo is divergent (logarithmically) so we take a cut-off at the radius r_{200}, which is defined as a radius at which the density is 200 times the critical density. Then the mass of the halo is

$$M_{200} = \int_0^{r_{200}} 4\pi r^2 \rho(r)\mathrm{d}r = 4\pi\rho_c r_s^3 \left(\ln(1+c) - \frac{c}{c+1}\right), \tag{4.44}$$

where $c \equiv r_{200}/r_s$ is the concentration of the halo. For a given mass the halo is fully characterized by the concentration.

The Newtonian potential and force corresponding to the density (4.43) is

$$\Phi_N(r) = -4\pi G\rho_c r_s^2 \frac{\ln(1+x)}{x}, \tag{4.45}$$

$$F_N(r) = -4\pi G\rho_c r_s \frac{\ln(1+x) - \frac{x}{1+x}}{x^2}. \tag{4.46}$$

We want to compute the chameleon profile for a NFW halo. Unlike stars the density of the halo is not constant and therefore neither does the effective mass of the field

$$V_{\text{eff},\phi}(\phi_B) \equiv 0 \qquad m^2(\rho) \equiv V_{\text{eff},\phi\phi}(\phi_B). \tag{4.47}$$

However, for realistic halos the matter density varies on scales much larger than the Compton wavelength m^{-1} of the chameleon field in that region. In such a case that $\mathrm{d}\ln\rho/\mathrm{d}r \ll m$ one can make an adiabatic approximation and treats $\rho(r)$ as a constant in the equations of motion. In Figure 4.7 is shown the effective mass of the chameleon field versus the distant x. Here we see that for the most relevant regions of the halo ($r < r_{200}$) we have $\mathrm{d}\ln\rho/\mathrm{d}r \ll m$ and therefore we can neglect the space dependence of the chameleon mass m.

4.5.1 Expected Behavior

We know we can treat $\rho(r)$ as a constant and thus we are expecting the behavior of the chameleon field in the case of the NFW halo to be rather similar to the interior of stars, except there are now no boundaries of the object. In the linear regime $R_{eq} < 0$ the chameleon should track the Newtonian potential and starts to deviate at $r \sim 1/m_\infty$ when it enters the exponentially damped phase. As the mass of the halo will grow and/or the screening potential will decrease, R_{eq} will become positive and the field will be screened at $r \lesssim R_{eq}$. As there is now no boundary as the surface of the star it will reach the linear solution at some radius $r \gtrsim R_{eq}$. However, for really massive halos and/or small screening potential the R_{eq} will be very large. In such a case the field might not catch the linear solution till $r \sim 1/m_\infty$ where it enters the damped phase.

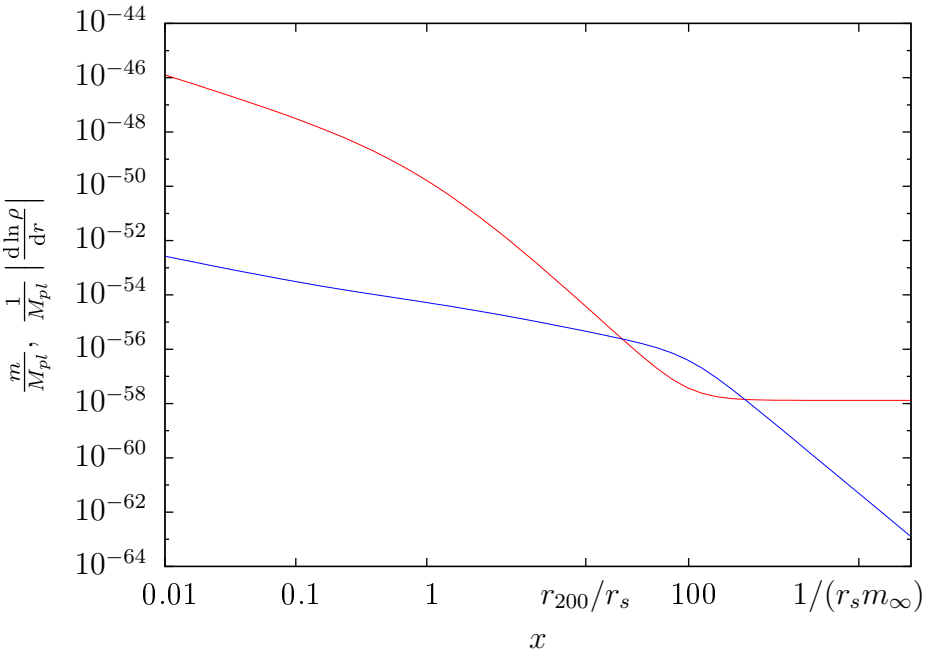

Figure 4.7: The effective mass of the chameleon field (red) and $\left|\frac{\mathrm{d}\ln\rho}{\mathrm{d}r}\right|$ (blue) versus distant $x = r/r_s$. For the most important part of the halo $x < r_{200}/r_s$ we have $\left|\frac{\mathrm{d}\ln\rho}{\mathrm{d}r}\right| \ll m$.

4.5.2 Boundary Condition

Because the NFW halo has a cuspy distribution, i.e. $\rho(x \to 0) \to \infty$, we do not have the symmetry condition $\mathrm{d}\phi/\mathrm{d}r(r = 0) = 0$. In the linear regime we will use the known behavior of the Newtonian potential, i.e.

$$\frac{\mathrm{d}\delta\phi}{\mathrm{d}r}(0) + \frac{\delta\phi(0)}{2r_s}\frac{c+1}{c} = 0. \tag{4.48}$$

In the non-linear case ($R_{eq} > 0$) we will look for the radius R_{roll} where the field starts to roll from the minimum of the effective potential as in the case of stars. For $r < R_{roll}$ we use the solution in the minimum of the effective potential $\phi = \phi_B + \delta\phi$. This solution ϕ_B is not a constant as in the case of the star but as long as holds the inequation

$$\frac{M_{pl}}{\beta}\frac{\Delta\phi_B}{\rho} \ll 1, \tag{4.49}$$

the solution is valid. At $r < R_{roll}$ we use linearized solution as in the case of stars

$$\phi = \phi_B(r)\left(1 + \epsilon\frac{R_{roll}}{r}\frac{e^{+mr} - e^{-mr}}{e^{+mR_{roll}} - e^{-mR_{roll}}}\right), \tag{4.50}$$

where now $m = m(r)$.

For $r \to \infty$ we will use the same condition as in the case of stars, i.e. we require

$$\frac{\mathrm{d}\delta\phi}{\mathrm{d}r} + \frac{1 + m_\infty r}{r}\delta\phi = 0, \tag{4.51}$$

at some $r_{max}(\sim 1/m_\infty)$, where the condition $\delta\phi/\phi_\infty < \epsilon$ holds.

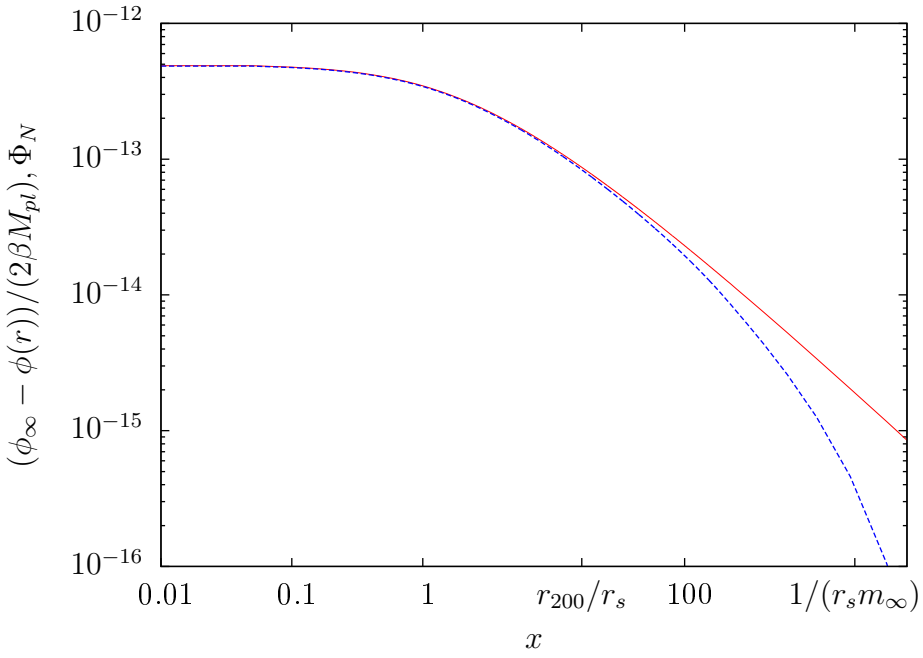

Figure 4.8: Chameleon field (blue dashed line) and Newtonian potential (red solid line) for a NFW density profile. Chameleon field is in the linear regime $R_{eq} = -r_s$ with the screening potential $\Phi_s = 10^{-12}$.

4.5.3 Numerical Results

In Figure 4.8 is shown a numerical solution to the chameleon field in the linear regime – we set the screening potential $\Phi_s = 10^{-12}$ and adjust density ρ_c so that the equivalence radius $R_{eq} = -r_s$. We also plot the Newtonian potential for comparison. We see that the chameleon field behaves like the Newtonian potential as we expected. At large radii the chameleon behavior starts to deviate from Newtonian and around $r \sim 1/m_\infty$ enters the exponentially damped phase.

In Figure 4.9 are shown chameleon forces for the same mass of the halo ($\rho_c = 3 \cdot 10^{-5}$ eV^4) but with several different screening potentials with corresponding equivalence radii. The force is damped at radii $r < R_{roll} < R_{eq}$ while at radii $r \gg R_{eq}$ the field manages to catch up the linearized solution and the force is unscreened as we expected.

Let us now explore the rotation curves in the presence of the chameleon field. The circular velocity which includes the acceleration due to the Newtonian force and the fifth force from the chameleon is given by

$$v_c(r) = \sqrt{\frac{1}{8\pi M_{pl}^2}\frac{M(r)}{r} + \frac{\beta r}{M_{pl}}\frac{\mathrm{d}\phi}{\mathrm{d}r}}. \tag{4.52}$$

In Figure 4.10 are shown rotation curves with and without the chameleon force. We see that for R_{eq} of order r_s the rotational curve looks like in the normal case but the larger amplitude. This means that we cannot distinguish this case from the more dense distribution of dark matter. For the detection of the chameleon field is important the behavior around the transition R_{roll} which therefore should not occur around the peak of the curve (or sooner).

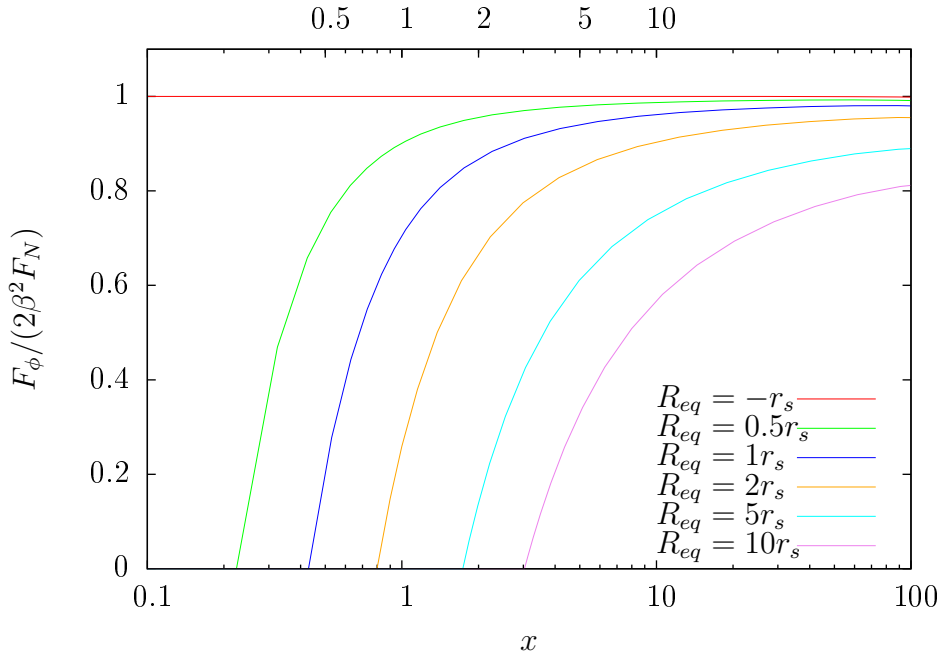

Figure 4.9: Chameleon force for several screening potentials with corresponding equivalence radii. For $R_{eq} < 0$ there is no screening while for $R_{eq} > 0$ inside a radius $R_{roll} < R_{eq}$ the force is exponentially damped.

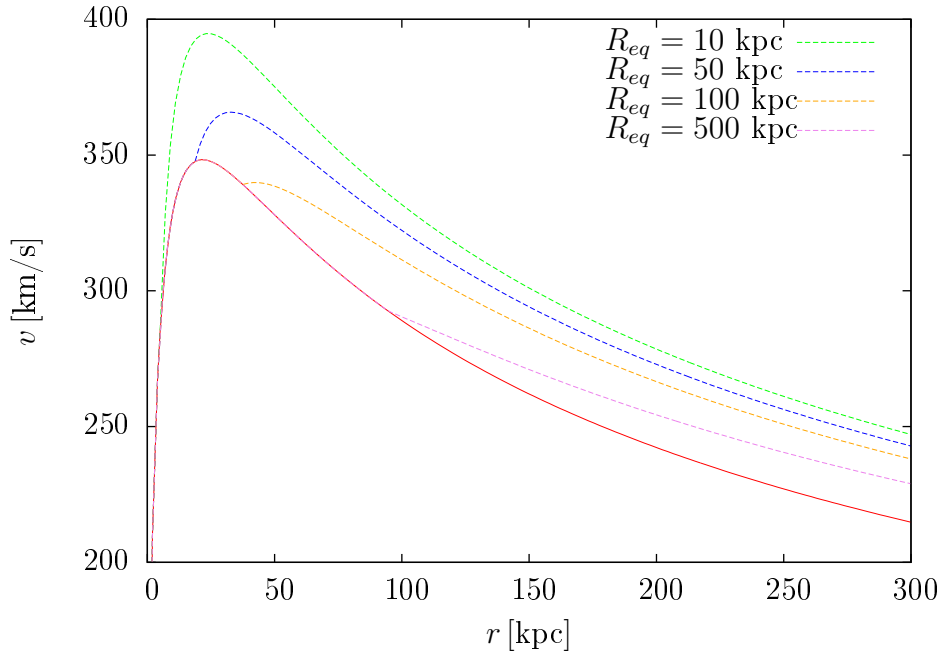

Figure 4.10: The circular velocity from the sole Newtonian potential (red solid line) and in the presence of the fifth force (dashed lines). Rotation curves for several screening potentials are shown.

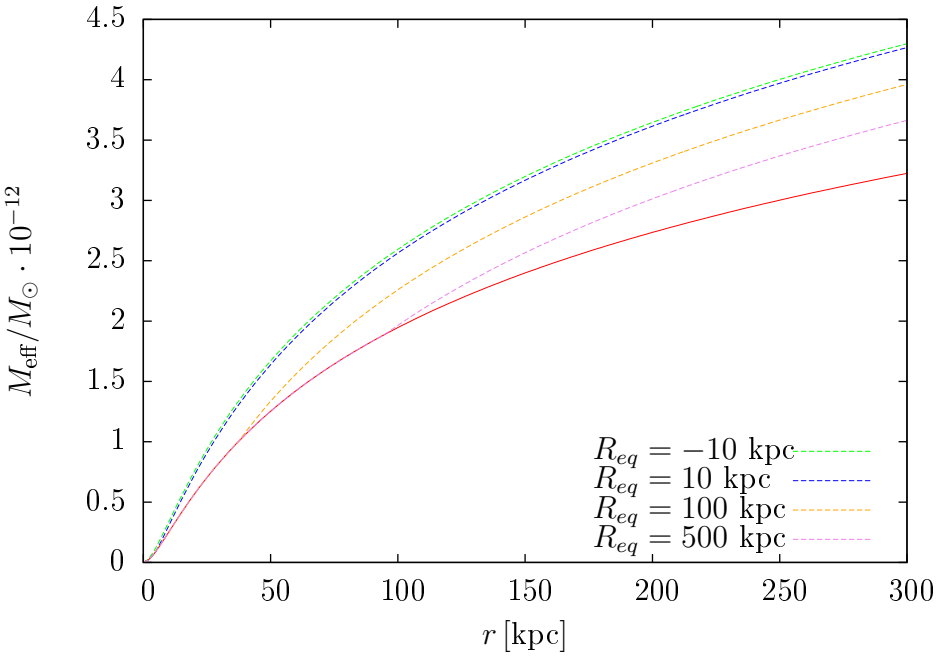

Figure 4.11: Effective mass distribution for lensing measurements (red solid line) and dynamical measurements (dashed lines) for several screening potentials Φ_s, scale radius $r_s = 10$ kpc and concentration $c = 16.4$.

We now "inverse" the relation (4.52) and ask a question: What mass distribution would we observe based on lensing measurements and on dynamical measurements? Relativistic particles are unaffected by the chameleon force whereas non-relativistic particles such as stars and galaxy's satellites obey the chameleon force and therefore these two types of measurements combined can detect the chameleon. The effective mass within radius r for dynamical measurements is

$$M_{\text{eff}}(r) = M(r) + 8\pi\beta M_{pl} r^2 \frac{\mathrm{d}\phi}{\mathrm{d}r}. \tag{4.53}$$

For lensing measurements we have $M_{\text{eff}} = M$. In Figure 4.11 is shown M_{eff} versus the distance r for lensing measurements and dynamical measurements for several screening potentials Φ_s for galaxy with the scale radius $r_s = 10$ kpc and the concentration $c = 16.4$. In Figure 4.12 is plotted a similar dependence, but now with several concentrations c of the halos of the same mass $M_{200} = 3 \cdot 10^{12} M_{\odot}$ and the same screening potential $\Phi_s = 10^{-6}$. And finally in Figure 4.13 is plotted the same dependence for several masses M_{200} of the halos with the same concentration $c = 15$ and the same screening potential $\Phi_s = 10^{-6}$.

From this mass distributions we see that with (enough accurate) both dynamical and weak lensing measurements the chameleon field can be detected quite easily. The main problem here is that the more massive halo, and/or the smaller the screening potential, the greater the distance where we would have to make our measurements.

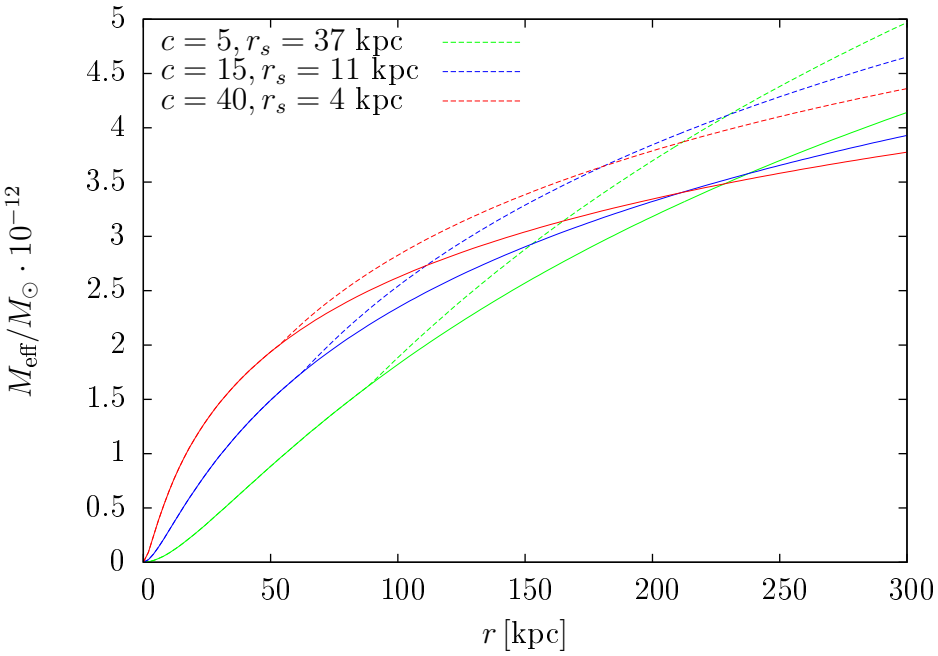

Figure 4.12: Effective mass distribution for lensing measurements (solid lines) and dynamical measurements (dashed lines) for several concentrations c, mass $M_{200} = 3 \cdot 10^{12} M_\odot$ and the screening potential $\Phi_s = 10^{-6}$.

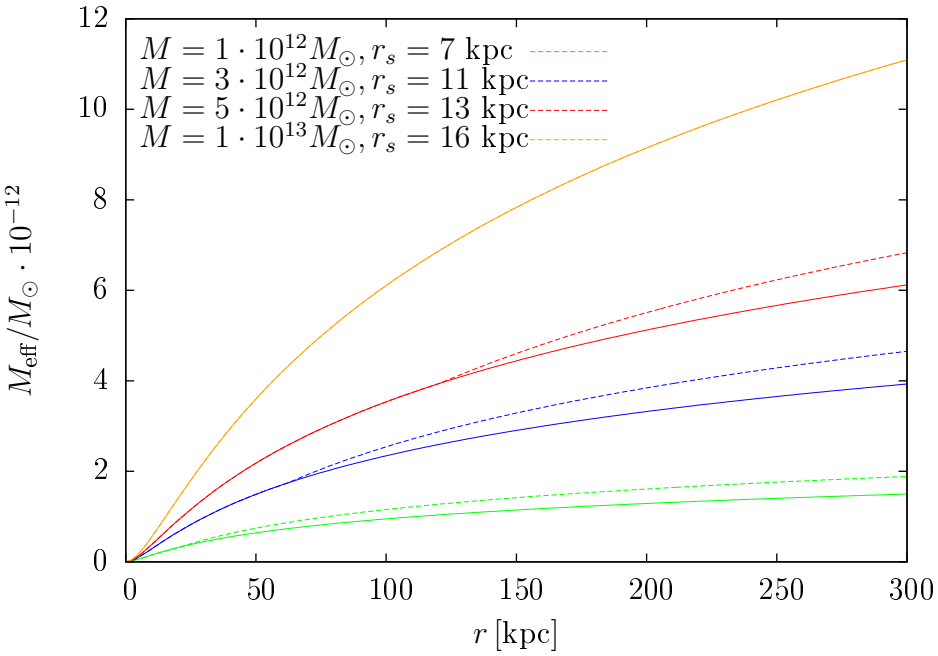

Figure 4.13: Effective mass distribution for lensing measurements (solid lines) and dynamical measurements (dashed lines) for several masses M_{200}, concentration $c = 15$ and the screening potential $\Phi_s = 10^{-6}$.

4.6 N-Body Simulations

We have solved rather specific problems – we assumed spherical symmetry and required only slow changes in the matter distribution. These are great for acquiring intuition about how the chameleon field works and for forecasts in approximate models. But for practical usage we need to be able to solve chameleon equations in a more generic case with no spherical symmetry. For this purpose we will use the *N-body simulations*. Let us start with "normal" N-body simulations.

4.6.1 Introduction

Many physical phenomena involve, or can be simulated with particle systems, where each particle interacts with all other particles. This involves the gravitational interaction among the stars, galaxies or clusters of galaxies which is of our main interest here. The purpose of cosmological simulations is to model the growth of structures in the universe.

Systems where the dominant force is long-range (such as gravity) are not well treatable by statistical mechanical methods – energy is not extensive, the canonical and micro-canonical ensembles do not exist, and the heat capacity is negative [22]. Thus we cannot work with a distribution function but rather directly with the particles. The cosmological N-body simulations use a comoving box of length L where dynamics of particles is collisionless, i.e. we treat only long-range gravitational interaction. The homogeneity and isotropy of the Universe on large scales is "solved" by using triply periodic boundary conditions.

The algorithm for N-body simulation with N particles of mass m_i with positions $\boldsymbol{x}_i(t)$ where $i = 1, ..., N$ can be characterized as

1. `Set initial conditions (positions and velocities)`
2. `Compute forces for each particle`
3. `Integrate equations of motion for each particle`
4. `Update time and go to 2.`

Initial conditions

The Universe was never completely smooth and this is encoded in small perturbations in otherwise homogeneous and isotropic matter density. Periodic boundary conditions imply discrete sampling in the Fourier space. Fluctuations in the particle distribution are represented by a population of modes with independent random phases in Fourier space. On scales which are small compared with the box size, the Central Limit Theorem guarantees an approximately Gaussian density distribution. A Gaussian distribution may be approximated on large scales by averaging over an ensemble of distributions in which mode amplitudes are drawn from a Gaussian variate.

Equations of motion

In cosmological simulations we should use GR equations of motion. On large scales, the Universe is nearly isotropic and described by the FLRW metric. How-

ever, on small scales GR reduces to the Newtonian physics. This fact can be used to think of the Universe as being filled with a self-gravitating fluid that locally obeys Newton's law of gravitation, while expanding as an FLRW metric on large scales. Hamiltonian of a test particle is [91]

$$H = \frac{\boldsymbol{p}_i^2}{2m_i a^2} + \frac{m_i}{a}\Phi(\boldsymbol{x}_i), \tag{4.54}$$

where $\boldsymbol{x}_i = \boldsymbol{r}_i/a(t)$ and $\boldsymbol{p}_i = a^2 m_i \dot{\boldsymbol{x}}_i$ are comoving canonical coordinates. The particles then move according to Hamilton's equations.

$$\begin{aligned} \frac{\mathrm{d}\boldsymbol{x}_i}{\mathrm{d}t} &= \boldsymbol{v}_i \\ \frac{\mathrm{d}\boldsymbol{v}_i}{\mathrm{d}t} &= -2\frac{\dot{a}}{a}\boldsymbol{v}_i - \frac{\nabla_i \Phi}{a^3} = -2\frac{\dot{a}}{a}\boldsymbol{v}_i + \frac{\boldsymbol{f}_i}{a^3}, \end{aligned} \tag{4.55}$$

where $\boldsymbol{v} = \dot{\boldsymbol{x}}$ and $\boldsymbol{f}_i = -\nabla_i \Phi$ is a force affecting a particle with a mass of unity $(\boldsymbol{F}_i/m_i)$. To integrate these equations numerically it is convenient to transform to a new time variable $p = a^\alpha$. Equations of motion then becomes

$$\begin{aligned} \frac{\mathrm{d}\boldsymbol{x}_i}{\mathrm{d}p} &= \boldsymbol{u}_i, \\ \frac{\mathrm{d}\boldsymbol{u}_i}{\mathrm{d}p} &= -2A(p)\boldsymbol{u}_i + B(p)\boldsymbol{f}_i, \end{aligned} \tag{4.56}$$

where

$$\begin{aligned} A(p) &= \frac{1 + \alpha + \ddot{a}a/\dot{a}^2}{2\alpha a^\alpha}, \\ B(p) &= \frac{1}{\alpha^2 \dot{a}^2 a^{2\alpha+1}}. \end{aligned} \tag{4.57}$$

These equations need to be discretized and then solved. There are many ways to do it, one example is the *leapfrog scheme* [45]

$$\begin{aligned} \boldsymbol{x}_{n+1} &= \boldsymbol{x}_n + \boldsymbol{u}_{n-1/2}\Delta p, \\ \boldsymbol{u}_{n+1/2} &= \boldsymbol{u}_{n-1/2}\frac{1 - A_n\Delta p}{1 + A_n\Delta p} + \frac{B_n}{1 + A_n\Delta p}\boldsymbol{f}_n\Delta p, \end{aligned} \tag{4.58}$$

where we omitted the particle indices i and replace them with the timestep indices n. The optimum choice of the parameter α will depend upon the problem under investigation.

This scheme is fast one and second-order accurate. One can also use slower but more accurate methods such as Runge-Kutta. The leapfrog integrator is an example of a symplectic integrator which preserves certain conserved quantities exactly, such as the total angular momentum, the phase-space volume, and the Jacobi constants.

4.6.2 Force computing

Integration of the equations of motion is rather straightforward and except the choice of an integration scheme there are no problems. The main problem comes

with the computation of the forces which must be both accurate and very fast (we are dealing with very large number of particles).

The force affecting a particles is

$$\boldsymbol{f}(\boldsymbol{x}) = \sum_i G m_i \frac{\boldsymbol{x} - \boldsymbol{x}_i}{|\boldsymbol{x} - \boldsymbol{x}_i|^3}, \tag{4.59}$$

where the sum is preformed over **all** particles, i.e. even the periodic ones. In practice, the periodic sum is approximated using the Ewald's method [50], which was originally invented for solid-state physics and imported to this field by Hernquist et al.[60]. The idea of the Ewald's method is to break the sum into two pieces – one that converges quickly in the real space (within the box) and one that converges quickly in the Fourier k-space (long range outside the box).

For a review of numerical techniques in force evaluations see e.g. [42] or [109].

Particle-Particle methods

The Particle-Particle (PP) methods are based on evaluating the sum in (4.59) directly. For few particles the direct summation provides very accurate result – the only inaccuracy arises from the Ewald's summation. But for large number of particles this brute-force approach is not feasible as it requires $O(N)^2$ time. If one wants to compute the sum more efficiently some approximation is needed.

The tree code was pioneered by Barnes and Hut [17]. It uses a hierarchical spatial tree to define localized groups of particles. The usual oct-tree method starts with the box containing all particles as a root. Then the box is split into up to eight child cells of half their parent's size. This is done recursively to the bottom as long as the current box contains at least n_{max} particles. Then for each box its mass and center of the mass is computed. When calculating the force affecting a particle in a box A one considers the ratio

$$\vartheta = \frac{D}{r}, \tag{4.60}$$

where D is the size of another box B and r is the distance to the center of mass of B. If ϑ is sufficiently small (usually $\vartheta \leq 1$) we can use the center of mass and mass of B to compute the force in A. If $\vartheta > 1$, we need to go to the children of B and do the same test.

It is rather straightforward to show that the time to compute the force per particle scales like the depth of the tree, i.e. $\ln N$. The computation of all N forces is then $O(N \ln N)$.

The fast multipole method (FMM) [38] can be viewed as a tree code but now instead of force we compute the potential first. In addition to expanding the Greens function at the source positions x_A, it also expands it at the sink positions x_B. Multipole expansions of the potential of a box are more accurate than a simple center of mass substitution, but for more computational cost. However, for a given accuracy the FFM is faster than tree code.

Grid-based methods

Instead of solving the integral version of (4.59), as with direct summation and its approximations, the grid-based methods, or Particle-Mesh methods (PM) solve

its differential form

$$\Delta\Phi(x) = 4\pi G\rho(x), \tag{4.61}$$

after discretization on a grid. The box is split into n regular mesh cells of length M. In the next we will denote by $\boldsymbol{x}_p$ the continuous position of a particle and by $\boldsymbol{x}_i$ the discrete position of a gridpoint. For easier implementation of the Fast Fourier Transform (FFT) or adaptive mesh size one uses number of cells in one dimension as powers of 2. The next step is to assign mass of particles to the grid:

$$\rho(\boldsymbol{x}_i) = \frac{1}{M^3}\sum_{p=1}^{N} m_p W(\boldsymbol{x}_i - \boldsymbol{x}_p). \tag{4.62}$$

The assignment function W can be expressed as a product of three one-dimensional functions w of a displacement of a particle from the cell center $\delta\boldsymbol{x}_i = |\boldsymbol{x}_i - \boldsymbol{x}_p|/M$. Three most often used schemes are:

- Nearest gridpoint (NGP) – the whole mass of a particle is assigned to the gridpoint closest to the particle. The assigned mass density is discontinuous as a particles moves across a cell boundary.

$$w = 1, \qquad \delta x \leq \frac{1}{2}.$$

- Cloud in Cell (CIC) – the mass is distributed among eight cells. The assigned mass density is continuous but the first derivative is discontinuous.

$$w = 1 - \delta x, \qquad \delta x \leq 1.$$

- Triangular-shaped Clouds (TCS) – the mass is distributed among 27 cells. Both mass density and first derivative are continuous, but higher derivatives are discontinuous.

$$w = \begin{cases} \frac{3}{4} - \delta x^2, & \delta x \leq \frac{1}{2}, \\ \frac{1}{2}(\frac{3}{2} - \delta x)^2, & \frac{1}{2} \leq \delta x \leq \frac{3}{2}. \end{cases}$$

The assignment function is $w = 0$ outside the given ranges.

It is straightforward to derive higher order schemes but the gain in accuracy is small in comparison with the rapid increase in the number of operations.

Next one needs to solve the potential on a grid. This can be done by either **Fast-Fourier-transform-based methods** or instead of FFT one can also use **multi-grid techniques**. Regardless of the used method one obtains the forces on a grid and needs to interpolate them back on particles

$$\boldsymbol{F}(\boldsymbol{x}_p) = \sum_{i=1}^{n} W(\boldsymbol{x}_i - \boldsymbol{x}_p)\boldsymbol{F}(\boldsymbol{x}_i). \tag{4.63}$$

To avoid any self-forces on the particles and thus to conserve momentum, it is necessary to use the same weighting function W in equations (4.62) and (4.63) [45].

Multi-grid techniques were developed by Brandt [23]. They solve the discretized Poisson equation (large matrix equations) using relaxation methods, such

as Gauss-Seidel iteration. It uses several grids – some courser with faster relaxation and some finer with slower but more accurate relaxation. The distribution of errors (the difference between current approximate solution $\Delta\Phi$ and the true one $4\pi G\rho$) is first smoothed on the finest grid (by Gauss-Seidel iterations). The problem is then transferred to a coarser grid and coarser grids until the convergence is achieved. Then the problem is transferred back to finer and finer grids, each time iterating until convergence.

For cosmological simulations are often used methods based on FFT as naturally incorporates periodic boundary condition. As we are also using a FFT-based method we described the algorithm in more detail.

4.6.3 Mesh Force Calculation

When calculating the mesh forces we first assign the masses of the particles onto the gridpoints to get discretized density distribution as described above. The density distribution is then convolved with the Green's function G appropriate for the required pairwise particle interaction. The obtained potential on a grid is differenced using the operator $\boldsymbol{D}$ to obtain forces at mesh points. And finally the forces are interpolated back to the particles.

The algorithm looks pretty straightforward. Transform the discretized density ρ using FFT, multiply it by a Green's function to get the potential $\hat{\Phi} = \hat{\rho} \cdot \hat{G}$ (hats denote quantities in k-space), performed inverse FFT to get the real-space potential Φ and finally obtain forces by the finite difference $\boldsymbol{F} = -\boldsymbol{D} \cdot \Phi$.

As the differencing operator one can use a classical two- or four-point finite difference approximation. In our algorithm we use a four-point operator

$$\hat{D}_j = i\frac{4}{3}\sin k_i - i\frac{1}{6}\sin 2k_i. \tag{4.64}$$

The first option of a Green's function, one could think of, is the Green's function of the continuous Poisson equation

$$\hat{G}(k) = -\frac{1}{k^2}. \tag{4.65}$$

But this choice does not reflect use of the finite difference approximation $\boldsymbol{D}$ and the smoothing we performed when we assign masses of particles to the grid by $\boldsymbol{W}$. One can compute the optimal Green's function which minimizes the total square deviation between the actual required force $\boldsymbol{R}$ and the approximate mesh force $\boldsymbol{F}$ [64]

$$\hat{G}(k) = \frac{\hat{\boldsymbol{D}}(k) \cdot \sum\limits_n \hat{W}^2(\boldsymbol{k_n})\hat{\boldsymbol{R}}(\boldsymbol{k_n})}{|\hat{\boldsymbol{D}}(k)|^2 \left[\sum\limits_n \hat{W}^2(\boldsymbol{k_n})\right]^2}, \tag{4.66}$$

where summation over n should be preformed over all mesh cells, even the periodic ones. However, the sum $\sum_n \hat{W}^2$ can be computed analytically using trigonometric identities and the sum $\sum_n \hat{W}^2\hat{\boldsymbol{R}}$ decays very quickly. Usually one can the neglect terms where the components of $\boldsymbol{n}$ have magnitudes greater than one or two.

The reference force $\boldsymbol{R}$ should be sufficiently smooth that it can be adequately represented by the discrete mesh. Smoothing is equivalent to prescribing a finite

size to the particles. The often used shape denoted by S_2 is [64]

$$\rho(r) = \begin{cases} \frac{48}{\pi a^4}\left(\frac{a}{2} - r\right) & r < a/2 \\ 0 & r > a/2 \end{cases} \tag{4.67}$$

with mass of unity and a the smoothing length. Since the highest frequency that can be represented by a discrete mesh (the Nyquist frequency) corresponds to a wavelength of two mesh spacings only forces corresponding to S_2 clouds with $a \geq 2M$ can be adequately reproduced. The force corresponding to particles of the S_2 shape is simply

$$\hat{\boldsymbol{R}}(\boldsymbol{k}) = -\frac{i\boldsymbol{k}\hat{S}^2}{k^2}. \tag{4.68}$$

4.6.4 Particle-Particle Particle-Mesh Algorithm

The above PM algorithm produces the mesh force with minimum errors for a given softening. However, on scales $r \lesssim a$ this *long-range force* quickly decays and does not match the true required force F. Particle-Particle Particle-Mesh algorithm ($\mathrm{P^3M}$) improves this force by including a *short-range* force by a direct particle-particle sum. The great advantage over direct PP methods is that now this sum is performed only over small range $r_c \lesssim a$. The short-range force F_{PP} is the difference between the required force and the approximate mesh force

$$F_{PP} = F(r) - R_a(r). \tag{4.69}$$

The empirically found cut-off radius $r_c = 0.7a$ is a compromise between the accuracy and the efficiency of the algorithm. In order to have a fast $\mathrm{P^3M}$ algorithm one must efficiently compute the short-range force for all particles $r < r_c$. This is achieved by creating an extra mesh – the chaining mesh of side $C \geq r_c$. Particles are then numbered and assigned to the chain mesh. When computing the short-range force one goes through the chain mesh of the particle and all 26 neighboring cells and adds the short-range force for particles with separation less than the cut-off radius.

One usually does not want the true required force $F(r)$ to be of the $1/r^2$ form as suggest by the (4.61) for a point source. This would lead to a collisional system of N particles with divergent forces and large-angle deflections during close encounters. This can be avoided by prescribing a shape to the particles as before. One can for simplicity take $F(r) = R_{\tilde{a}}(r)$ with the arbitrary softening length $\tilde{a} < a$ which cannot be appropriately represent on the mesh, i.e. $\tilde{a} < 2M$.

4.6.5 Solution to the Chameleon Field

We now want to use the above FFT algorithm to solve the chameleon equation of motion

$$\Delta\phi = \frac{\beta}{M_{pl}}\rho + V_{,\phi}(\phi) = \frac{\beta}{M_{pl}}\rho - \frac{\beta}{M_{pl}}\rho_\infty \left(\frac{\phi_\infty}{\phi}\right)^{1-n} \tag{4.70}$$

with

$$\phi_{\min}(\rho) = \phi_\infty \left(\frac{\rho_\infty}{\rho}\right)^{1/(1-n)}. \tag{4.71}$$

The problem is obvious – this non-linear equation does not have a Green's function to convolve with the density field and thus we must solve it iteratively. The simplest way is to solve it as a classical Poisson equation with modified right hand, i.e.

$$\Delta\phi_{(i+1)} = \frac{\beta}{M_{pl}}\rho - \frac{\beta}{M_{pl}}\rho_\infty \left(\frac{\phi_\infty}{\phi_{(i)}}\right)^{1-n}. \tag{4.72}$$

What is the appropriate initial value of the field $\phi_{(0)}$? One can start to approximate the solution around the background value and choose $\phi_{(0)} = \phi_\infty$. This results into the normal Poisson equation for the Newtonian potential and after the first iteration one obtain the linear solution $\phi_{(1)} = \phi_\infty + 2\beta M_{pl}\Phi_N$. If we have only small objects with low mass such as $\phi_{(1)} > 0$ everywhere this method works and we obtain the correct **linear** solution.

However, we are mostly interested in the non-linear regime where the condition $\phi_\infty + 2\beta M_{pl}\Phi_N > 0$ does not hold everywhere (and so does $\phi_{(1)} < 0$ somewhere). In such regions we must somehow modify these negative values to get a meaningful solution. We can set $\phi = \phi_{\min}$ to have a positive solution. Such regions then have $V_{\mathrm{eff},\phi} = 0$. The following iteration steps either result into the wrong solution (with large regions of $\phi_{\min}$) or does not converge at all.

Other iteration scheme one can try to use is just the inverse of the first, i.e.

$$\begin{aligned}\Delta\phi_{(i)} &= \frac{\beta}{M_{pl}}\rho - \frac{\beta}{M_{pl}}\rho_\infty \left(\frac{\phi_\infty}{\phi_{(i+1)}}\right)^{1-n} \\ \phi_{(i+1)} &= \phi_\infty \frac{1}{\left(\frac{\rho}{\rho_\infty} - \frac{M_{pl}}{\beta}\frac{\Delta\phi_{(i)}}{\rho_\infty}\right)^{1/(1-n)}}.\end{aligned} \tag{4.73}$$

Note that this scheme is not suited for every case as it does not converge everywhere. This can be easily seen in the linear case where we want our final solution to be $\phi_\infty + 2\beta M_{pl}\Phi_N$. Plugging this linear solution into the iterative scheme we see that the next iteration will be $\phi = \phi_{\min}$. But in principle this scheme can be used in the screened regions to get the right solution and outside the screened regions try some other iteration schemes.

We did try this scheme in an approximate model of stars, i.e. dense spherical objects in a background. Inside the star this works well as the term $\Delta\phi$ is small compared to the density of the object, but it fails near the surface, where the density changes rapidly. Outside the object the solution does not converge as discussed above.

The next iteration scheme we tried is obtained by linearization of the equations around the background value, $\phi_{(i)} = \phi_\infty + \delta\phi_{(i)}$. By the Taylor expansion of $V_{,\phi}$ around ϕ_∞ and the appropriate reconfiguration of the terms one can obtain the iteration scheme

$$\Delta\phi_{(i)} = \frac{\beta}{M_{pl}}\delta\rho + m^2(\phi_{(i-1)})\delta\phi_{(i)}, \tag{4.74}$$

where

$$m^2_{(i)} \equiv \frac{V_{,\phi}(\phi_\infty + \delta\phi_{(i)}) - V_{,\phi}(\phi_\infty)}{\delta\phi_{(i)}}. \tag{4.75}$$

If it was the case $m^2 = const$ we would have the exact Green's function $\hat{G}(k) = -1/(k^2 + m^2)$. This is true for the first iteration where we choose $\delta\phi_{(0)} = 0$

everywhere. In this case $m^2 = V_{,\phi\phi}(\phi_\infty)$ so we have an exact linearized solution with the correct damping term. But in this case the scheme posses the same (bad) behavior as the first scheme (4.72) – in the non-linear case when $\phi_\infty + 2\beta M_{pl}\Phi_N < 0$ somewhere the scheme breaks down. But even in the linearized case we have $m = m(r)$ after the first iteration and we cannot solve (4.74) with the FFT.

4.7 Discussion and Outlook

We have studied the numerical behavior of the chameleon field and successfully applied the shooting method to get results under various conditions. Let us start with a discussion of the accuracy and reliability of our algorithm based on our results from the planar slab in a vacuum.

We saw that even with the exact initial conditions the integration of non-linear differential equations is difficult and unstable. To make the integration possible we needed to achieve really high accuracy ($\ll 10^{-10}$). For this purpose the fourth-order Runge-Kutta algorithm proved to be sufficient. However, as we are dealing with smooth functions using the Bulirsch-Stoer method [95] could provide better results.

The shooting algorithm we have used had great success when matching the boundary conditions. We managed to obtain the proper initial conditions with the required accuracy – the computed errors came from the integration errors on large distances. We also wrote the algorithm generally enough that it can be successfully applied to arbitrary boundary conditions. However, there are issues associated with the instability of the integration at large distances. If we do not choose the initial guess close enough to the true solution, the integration will always fail and we cannot even find the two values of the shooting function which are on two different sides of the root. To overcome this obstacle we came with a solution using sequential integration. We integrated over much smaller ranges than we truly wanted to achieve, where the solution was still stable. Then we used these obtained initial conditions as a new guess when integrating over full range. This idea is implemented in the code only partially and was done mainly manually. This is of course ineffective and it is the next thing we will implement properly into our algorithm.

In the model of stars we focused especially on cases with no analytical solution – cases where neither of commonly used conditions $R_{roll} = 0$ nor $(R_c - R_{roll})/R_c \ll 1$ is satisfied. This was done in order to get an idea of the chameleon behavior which could be generalize to the model of the NFW halo where the condition $(R_c - R_{roll})/R_c \ll 1$ has no purpose as there are no boundaries. However, it would be worth probing the behavior of the chameleon in these limits more closely and compare the numerical results with analytical. One then could get a better idea where these analytical solutions break down and whether e.g. the suppression factor (3.65) is correct even for cases $R_{eq} \sim R_c$.

For the NFW halo we successfully computed the chameleon profile for various parameters of the halo and the chameleon screening potential. From the rotational curves and the effective mass distribution we see that if we want to detect the chameleon field solely with dynamical measurements we need to have a large sample of galaxies with extended and accurate rotational curves. If the screening potential is large and/or the halo is not massive enough we cannot distinguish

between the chameleon and more dense dark matter distribution. On the other hand if the halo is very massive the screening occurs everywhere where we can measure the rotational curves. For the detection of the chameleon effect we need to have very accurate measurements around the transition at $r \sim R_{roll}$. If we do have also non-dynamical measurements from the weak lensing the chameleon effect can be detected, in principal rather easily. The main issue here is the lack of precise spectroscopic measurements (for the velocity information) and at the same time weak lensing measurements.

We are planning to compute the chameleon profile for other models of halos other than NFW, parametrized models described by

$$\delta\rho(r) = \frac{\rho_c}{(r/r_s)^\alpha \left[1 + r/r_s\right]^\beta}, \tag{4.76}$$

or

$$\delta\rho(r) = \frac{\rho_c}{(r/r_s)^\alpha \left[1 + (r/r_s)^\beta\right]}. \tag{4.77}$$

Our main goal for the future is the N-body simulation for the chameleon field. We have already started to work on this project, however, this turns out to be rather difficult. We started with the approach based on the FFT with proposed iterative schemes but this seems to be a wrong way to continue. Next we want to try the multi-grid based method with the Full Approximation Scheme (FAS) [23] which is used for solving non-linear problems. Once we have a working method we will run large cosmological simulations. This tasks will be performed in cooperation with ANL.

Within the DESC, the core of our cooperation with the ANL group is large-scale cosmological simulations for LSST science. In cosmological simulations for the LSST, we wish to include a large number of models, one of which is the Hu-Sawicki $f(R)$ model, which we have studied. After we run these large simulations we can analyze their outcome. This will eventually lead to constraining physics beyond the cosmological standard model once data from the LSST become available.

5. Conclusion

As we do not properly understand 95% of the content of the Universe it would be hasty to draw conclusions about the origin of the cosmic acceleration. In order to understand the physics behind the dark energy we must also study other alternative theories. For this theories we must find their differences compared to the cosmological constant and ways to test them. Even if all of them prove to be wrong it is a way how to make the standard cosmological model more precise and trustworthy.

In the work we described some basic problems concerning the cosmological constants and why it is worth probing the alternative theories. We described the most studied theories – ones that modify gravity itself such as $f(R)$ or ones that introduce a new scalar field such as the quintessence. We also showed the relation between these two types of theories via the conformal transformation.

After the theoretical work will have been done on these alternatives we must have sufficiently accurate data to test them. One of the project designed to study dark energy is the LSST Project. The LSST will be one of the largest telescope in the world. The system will produce a wide-field deep astronomical survey over almost the whole southern sky. The LSST will provide an unprecedented depth from co-added images and unique details of the Universe. The great amount of data produced every night by the LSST will help to characterize the properties of the dark energy. Amongst many other projects and missions the greatest synergy will be between the LSST, Euclid and WFIRST. The scientific opportunity offered by the combination of data from LSST, WFIRST and Euclid goes well beyond the science enabled by any one of the data sets alone. The range in wavelength, angular resolution and redshift coverage that these missions jointly span is remarkable.

The chameleon gravity is one of the alternative theories explaining the accelerated expansion of the Universe. This theory is interesting for the DESC (and for the LSST) as it has rather general behavior. Even though the term chameleon field sounds rather exotic, in a general scalar-field theory (including $f(R)$ theories) with a matter coupling and arbitrary self-interaction potential, there will generically be some values of the field about which the field theory exhibits a chameleon mechanism.

In this work we studied chameleon field in the context of Hu-Sawicki $f(R)$ models. We introduced some basic properties of the chameleon field and derived an expected behavior in and near stars and also its behavior in galaxies described by the NFW halo. We managed to develop an algorithm based on the shooting method to numerically compute the chameleon field for spherically symmetric objects. We then successfully applied our algorithm to specific problems. We computed the modified dynamic in galaxies for non-relativistic particles and its effect on measurements. We specifically showed how the presence of the chameleon field can change the rotational curves and how this can be measured by combining probes of the weak lensing and dynamical measurements obtain e.g. from spectroscopic measurements. These studied cases tested the usefulness of our algorithm.

During the work we came up with other projects where we can apply our

algorithm and these we will pursue. The next goal after spherically symmetric objects is the N-body simulation of the chameleon field and modified evolution of the large scale structures. So far we have started to work on the algorithm based on FFT and found out how difficult this problem is. We want to try different approach than FFT, the multi-grid based method with the Full Approximation Scheme which is more optimized for non-linear problems.

To sum up, we fulfilled the first objective in the study of the chameleon field. We successfully probed the behavior of the chameleon on galactic scales and came up with forecasts for future observations. Our next task is to probe the chameleon behavior on cosmological scales with N-body simulations.

A. Standard Cosmological Model

In this section we just briefly review the modern cosmology. This serves as a summary of important equations not all of which are derived in full detail. For further reading see e.g. [34] (short review) or [46] (full derivation).

A.1 Introduction

A.1.1 Assumptions

The standard cosmological model is based on several assumptions. The most important one is the omnipresent **validity of the Einstein's equations**

$$R_{\mu\nu} - \frac{1}{2}Rg_{\mu\nu} = \frac{1}{M_{pl}^2}T_{\mu\nu}, \tag{A.1}$$

where $R_{\mu\nu}$ is the Ricci tensor, R the Ricci scalar, M_{pl} the reduced Planck mass and $T_{\mu\nu}$ the stress-energy tensor. The stress-energy tensor of a perfect fluid has a form

$$T_{\mu\nu} = (\rho + p)u_\mu u_\nu + pg_{\mu\nu}, \tag{A.2}$$

where ρ is the energy density and p the pressure. The next assumption is **the Copernican principle** (also known as the cosmological principle) which states that we do not live in special place nor time. Observations of isotropy of our Universe on large scales then imply that the whole Universe is spatially homogeneous and isotropic. This homogeneous and isotropic spacetime symmetry is encoded in the FLRW metric

$$\mathrm{d}s^2 = -\mathrm{d}t^2 + a^2(t)\left[\frac{\mathrm{d}r^2}{1-kr^2} + r^2\mathrm{d}\Omega^2\right], \tag{A.3}$$

where $k = 0, +1, -1$ for a flat, closed, or open space respectively. We normalized a in a way that $a = 1$ in the present. The coordinate t measures the time on hypersurfaces of constant density, while the space-coordinate r measures in the flat Universe the comoving distance, i.e. the distance that is constant with respect to the expansion of the universe. The differential solid angle is $\mathrm{d}\Omega = \sin\theta\mathrm{d}\theta\mathrm{d}\phi$ with the spherical coordinates θ and ϕ.

To obtain such homogeneous and isotropic Universe **the cosmic inflation** is needed. During the inflationary era ($t \sim 10^{-36} - 10^{-32}$ s) the Universe increased its size by a factor of 10^{43} and dilutes any initial curvature. Hence next we will consider only flat ($k = 0$) spaces.

To obtain observed structures in the Universe only a baryonic component of the matter is not enough. Hence we need an additional unknown exotic component of matter – **cold dark matter**. The *cold* refers to non-relativistic particles with the equation of state $w = 0$.

To explain the present acceleration of the Universe we need some sort of an exotic fluid with the equation of state $w \equiv p/\rho < -1/3$. The simplest solution is **the cosmological constant** Λ. The Einstein's equations are then modified to

$$R_{\mu\nu} - \frac{1}{2}Rg_{\mu\nu} + \Lambda g_{\mu\nu} = \frac{1}{M_{pl}^2}T_{\mu\nu}. \tag{A.4}$$

More convenient way to treat the cosmological constant is to move it at the right hand side of the equations as a perfect fluid with the equation of state $w = -1$ and the energy density

$$\rho_\Lambda \equiv M_{pl}^2 \Lambda. \tag{A.5}$$

These assumptions about the Universe lead us to the standard cosmological model – the ΛCDM model.

A.1.2 FLRW metric

The FLRW metric for flat spaces simplify as

$$\mathrm{d}s^2 = -\mathrm{d}t^2 + a^2(t)\left[\mathrm{d}r^2 + r^2\mathrm{d}\Omega^2\right]. \tag{A.6}$$

The expansion of the Universe is usually measured through the *redshift* z

$$1 + z \equiv a^{-1} \tag{A.7}$$

From the Einstein's equations is obtained

$$H^2 \equiv \left(\frac{1}{a}\frac{\mathrm{d}a}{\mathrm{d}t}\right)^2 = \frac{1}{3M_{pl}^2}\rho \tag{A.8}$$

$$\frac{1}{a}\frac{\mathrm{d}^2 a}{\mathrm{d}t^2} = -\frac{1}{6M_{pl}^2}(\rho + 3p), \tag{A.9}$$

where H is the Hubble parameter, ρ is the overall density $\rho = \rho_m + \rho_r + \rho_\Lambda$. The former one is usually written as

$$1 = \Omega_r + \Omega_M + \Omega_\Lambda + \Omega_k, \tag{A.10}$$

where $\Omega_i \equiv 8\pi G\rho_i/3H^2$ and $\Omega_\Lambda \equiv \Lambda/3H^2$ are *density parameters*. In this equation we also recover the curvature $\Omega_k \equiv -\frac{k}{a^2H^2}$. From measurements of the overall density of matter and dark energy we can determine the curvature. The ESA's Planck satellite data combined with BAO measurements confirmed the flatness of the space [3]

$$\Omega_k = 0.000 \pm 0.005 \quad (95\%,\ \mathit{Planck}\mathrm{TT}{+}\mathrm{lowP}{+}\mathrm{lensing}{+}\mathrm{BAO}). \tag{A.11}$$

Conservation of the stress-energy tensor yields the continuity equation

$$\frac{\mathrm{d}\rho}{\mathrm{d}t} + 3H(\rho + p) = 0. \tag{A.12}$$

These three equations are not independent (only two them). To solve this system of equations for three unknown variables (a, ρ and p) we need a relation between ρ and p – the equation of state $p \equiv \rho w$. For a constant w we can integrate the equation (A.12) to obtain

$$\rho = \rho_0 a^{-3(1+w)}. \tag{A.13}$$

The early Universe is dominated by the radiation and ultra-relativistic matter with equation of state $w = 1/3$. After the Universe cooled enough masses of the particles eventually dominated over the radiation components at the equality

epoch around $z_{eq} \sim 3200$. From this epoch until recently the Universe is dominated by cold dark matter with the dust equation of state $w = 0$. Around $z \sim 2$ the Universe starts to slowly accelerate and around $z \sim 1/2$ begins to dominate the Universe dark energy with the equation of state $w = -1$.

From $H^2 \approx \frac{1}{3M_{pl}^2}\rho_*$ with ρ_* being the dominant component of the Universe one can easily show that in these epochs the Universe expands as

$$a(t) \propto \begin{cases} t^{\frac{1}{2}} & (w = \frac{1}{3}) \\ t^{\frac{2}{3}} & (w = 0) \\ e^{Ht} & (w = -1) \end{cases} \tag{A.14}$$

A.2 Perturbed Universe

In this section we use assumptions that are not special to GR but can hold in other modified theories as well: 1) spacetime is a 4-dimensional pseudo-Riemannian manifold, 2) special relativity holds locally, and 3) the weak equivalence principal holds (freely-falling bodies follow geodesics).

A.2.1 Newtonian Gauge

The most general perturbed metric can be written as $g_{\mu\nu} = g^{(0)}_{\mu\nu} + \delta g_{\mu\nu}$, where an unperturbed metric $g^{(0)}_{\mu\nu}$ is the FLRW metric

$$\mathrm{d}s^2 = a^2(-\mathrm{d}\eta^2 + \gamma_{ij}\mathrm{d}x^i\mathrm{d}x^j) \tag{A.15}$$

with the conformal time $\eta = \int a^{-1}\mathrm{d}t$ and the three-metric γ_{ij} of constant curvature spaces. Perturbation of the metric is schematically

$$\delta g_{\mu\nu} = a^2 \begin{pmatrix} -2\Phi & w_i \\ w_i & -2\Psi\gamma_{ij} + h_{ij} \end{pmatrix}, \tag{A.16}$$

where Φ and Ψ are scalars (Newton and curvature potential), w_i is a 3-vector and h_{ij} is a traceless 3-tensor. Now, we can decompose the vector w_i into a longitudinal and a transverse component

$$w_i = w_i^{\parallel} + w_i^{\perp}, \tag{A.17}$$

where by construction

$$\epsilon^{ijk}\partial_i w_j^{\parallel} = \partial^i w_i^{\perp} = 0. \tag{A.18}$$

A similar decomposition can be done for traceless part h_{ij}

$$h_{ij} = h_{ij}^{\parallel} + h_{ij}^{\perp} + h_{ij}^{T}, \tag{A.19}$$

where the divergences $\partial^i h_{ij}^{\parallel}, \partial^i h_{ij}^{\perp}$ are longitudinal and transverse vectors and h_{ij}^T is transverse, i.e.

$$\epsilon^{ijk}\partial_i\partial^l h_{lj}^{\parallel} = \partial^i\partial^j h_{ij}^{\perp} = \partial^i h_{ij}^{T} = 0. \tag{A.20}$$

Since $w_i^{\parallel}$ and $\partial^i h_{ij}^{\parallel}$ are curl-free, they can be written in terms of some scalar functions

$$w_i^{\parallel} = \partial_i E, \quad h_{ij}^{\parallel} = \left(\partial_i\partial_j - \frac{1}{3}\gamma_{ij}\partial_k\partial^k\right) B \equiv D_{ij}B, \tag{A.21}$$

where we define the traceless operator D_{ij}. By taking divergence or curl of the Einstein equations we can deal only with longitudinal or transverse terms which therefore completely decouple from each other. Since the density perturbation δ is a scalar it couples only to longitudinal terms, which can be derived from a scalar quantity.

A vector $h_{ij}^{\perp}$ is giving rise to a rotational velocity perturbation while a tensor h_{ij}^{T} is giving rise to gravitational waves. Since transverse terms couple to rotationally or vorticity modes only, which decrease as a^{-1}, vector and tensor perturbations can be neglected. We are therefore left with only four scalars quantities Φ, Ψ, E and B. We can further simplified metric (A.16) by choosing specific gauge. We can impose up to four conditions which are $w_i = 0$ and $B = 0$. The metric in this so-called *Newtonian* or *longitudinal* gauge takes a form

$$g_{\mu\nu} = a^2 \begin{pmatrix} -(1+2\Phi) & 0 \\ 0 & (1-2\Psi)\gamma_{ij} \end{pmatrix}, \tag{A.22}$$

while the inverse metric (keeping only the linear terms in potentials) is

$$g^{\mu\nu} = a^{-2} \begin{pmatrix} -(1-2\Phi) & 0 \\ 0 & (1+2\Psi)\gamma^{ij} \end{pmatrix}. \tag{A.23}$$

Christoffel symbols for this metric are

$$\begin{aligned} \Gamma^0_{00} &= \mathcal{H} + \dot{\Phi}, \\ \Gamma^0_{0i} &= \partial_i \Phi, \\ \Gamma^0_{ij} &= \left[\mathcal{H}(1-2\Phi-2\Psi) - \dot{\Psi}\right]\gamma_{ij} \\ \Gamma^i_{00} &= \partial^i \Phi, \\ \Gamma^i_{j0} &= (\mathcal{H} - \dot{\Psi})\delta^i_j, \\ \Gamma^i_{jk} &= \gamma^i_{jk} + \gamma_{jk}\partial^i\Psi - \delta^i_j\partial_k\Psi - \delta^i_k\partial_j\Psi, \end{aligned} \tag{A.24}$$

where dot means partial derivative with respect to the conformal time, $\mathcal{H} \equiv \dot{a}/a$ is the conformal Hubble parameter and γ^i_{jk} is the spatial connection needed when non-Cartesian coordinates are used.

A.2.2 Kinematics

Let us now examine a motion of particles in the metric (A.22) where the potentials are assumed to be small enough ($\Phi \sim \Psi \sim 10^{-5}$) so we can treat them perturbatively. The proper (physical) 3-velocity v^i measured by a comoving observer, or the peculiar velocity with respect to the uniform Hubble flow, is defined as

$$\frac{\mathrm{d}x^i}{\mathrm{d}\eta} \equiv (1+\Phi+\Psi)v^i, \tag{A.25}$$

which ensures that for the light ($\mathrm{d}^2 s = 0$) the velocity is $v = 1$. The four-velocity $u^\mu \equiv \mathrm{d}x^\mu/\mathrm{d}\tau$ where τ is the proper time, is

$$u^\mu = \frac{\gamma}{a(1+\Phi)}\left[1, (1+\Phi+\Psi)v^i\right], \tag{A.26}$$

while the contravariant components are

$$u_\mu = \gamma a \left[1 + \Phi, (1 - \Psi) v_i\right], \tag{A.27}$$

where $\gamma \equiv (1 - v^2)^{-1/2}$ is the special relativistic Lorentz factor. Freely-falling particles move along geodesics of the metric (A.22) and thus obeying the equation of motion

$$\frac{1}{\gamma a (1 - \Psi)} \frac{\mathrm{d}}{\mathrm{d}\eta} \left[\gamma a (1 - \Psi) v^i\right] = -\partial^i (\Phi + v^2 \Psi) - (1 + \Phi + \Psi) \gamma^i_{jk} v^j v^k. \tag{A.28}$$

This equation simplifies for nonrelativistic particles ($v \to 0$), or on the other hand for massless particles ($v^2 = 1$), as

$$\frac{1}{a} \frac{\mathrm{d}(a v^i)}{\mathrm{d}\eta} = -\partial^i \Phi, \qquad v^2 \ll 1 \tag{A.29}$$

$$\frac{\mathrm{d}v^i}{\mathrm{d}\eta} = -\partial^i_\perp (\Phi + \Psi), \qquad v^2 = 1 \tag{A.30}$$

where the gradient is taken in the plane perpendicular to the photon trajectory

$$\partial^i_\perp \equiv \partial^i - v^i v_j \partial^j \tag{A.31}$$

Another useful relation comes from the redshift of a light. An observer at the rest, with respect to the uniform Hubble flow ($v = 0$), measures the energy of a photon $E = -p_\mu u^\mu_0$. From that and a normalization of a four-momentum $p_\mu p^\mu = 0$ we get

$$p_\mu = a \left[(1 + \Phi) E, (1 - \Psi) \vec{p}\right], \tag{A.32}$$

where we define the three-momentum such that $|\vec{p}| = E$. From the equation of motion along geodesics we get

$$\frac{1}{aE} \frac{\mathrm{d}(aE)}{\mathrm{d}\eta} = \dot{\Psi} - v^i \partial_i \Phi. \tag{A.33}$$

After an integration from a redshift z to the time of the observation we get

$$(1 + z) \frac{E_{obs}}{E_{em}} = 1 + \Phi_{em} - \Phi_{obs} - \int_0^z (\dot{\Phi} + \dot{\Psi}) \frac{\mathrm{d}\eta}{\mathrm{d}z} \mathrm{d}z, \tag{A.34}$$

which is the Sachs-Wolfe effect.

A.3 Methods to Measure the Potentials

We want to measure the three free functions of the metric (A.22) – $a(\eta)$ and potentials $\Phi(\eta, x)$ and $\Psi(\eta, x)$ – to constraint gravity. The simplest way to do it is to use the equations (A.30) and (A.34). However, in practice these direct methods are very inaccurate.

A.3.1 Growth of Structure

The growth of density perturbation is a great way to measure the potential Φ. The stress-energy tensor for scalar perturbations is

$$T_0^0 = -(\bar{\rho} + \delta\rho), \tag{A.35}$$
$$T_i^0 = -(\bar{\rho} + \bar{p})\partial_i u, \tag{A.36}$$
$$T_j^i = \delta_j^i(\bar{p} + \delta p) + \frac{1}{2}(\bar{\rho} + \bar{p})\left(\partial^i\partial_j - \frac{1}{3}\delta_j^i\Delta\right)\pi, \tag{A.37}$$

where $\Delta = \partial_i\partial^i$, $\bar{\rho}$ and $\bar{p}$ are the background density and pressure and u and π are velocity and shear stress potentials, respectively. These perturbations are of course gauge-dependent. However, one can also work with gauge-independent quantities such as the physical number density perturbation in the fluid rest frame, obtained from the conformal Newtonian gauge variables as [20]

$$\nu \equiv \frac{\delta\rho + 3\mathcal{H}u}{\bar{\rho} + \bar{p}}. \tag{A.38}$$

For a non-relativistic fluid on scales much less than the Hubble length with a negligible shear stress, the **linear** perturbations of energy-momentum conservation gives

$$\frac{1}{a}\frac{\partial}{\partial\tau}\left(a\frac{\partial\nu}{\partial\tau}\right) = \Delta\left(\Phi + c_s^2 + \sigma\right), \tag{A.39}$$

where $c_s^2 = \mathrm{d}\rho/\mathrm{d}p$ is the adiabatic sound speed and the dimensionless entropy perturbation is

$$\sigma = \frac{\delta p - c_s^2\delta\rho}{\bar{\rho} + \bar{p}}. \tag{A.40}$$

Through the growth of structures thus one can measure the potential Φ.

A.3.2 Gravitational Lensing

Weak gravitational lensing bends the trajectory of the light according to (A.30). The angular deflection integrated over the past light cone between z and $z + \delta z$ is

$$\delta\vec{\alpha} = -\vec{\nabla}_\perp(\Phi + \Psi)\frac{\mathrm{d}\eta}{\mathrm{d}z}\delta z, \tag{A.41}$$

where α is a (two-dimensional) vector perpendicular to the trajectory of the light. The gravitational lens equation [18]

$$\vec{\beta} = \vec{\theta} - \frac{r_{LS}}{r_S}\delta\vec{\alpha}, \tag{A.42}$$

where θ is the observed direction of a ray and β the direction to the source in the absence of the deflection. The distances are are the comoving angular distances from the lens plane to the source plane, and from the observer to the source plane respectively.

We cannot observe the absolute deflection since we do not know the the true direction of the source. However, the gradient of the deflection results in an image

magnification and shear that are observable. These are described by the inverse magnification matrix

$$\mathbf{M}^{-1}(\vec{\theta}) = \frac{\partial\vec{\beta}}{\partial\vec{\theta}} = \mathbf{1} + \int_0^{z_S} \frac{r_S r_{LS}}{r_S}\vec{\nabla}_\perp\vec{\nabla}_\perp(\Phi+\Psi)\frac{\mathrm{d}\eta}{\mathrm{d}z}\mathrm{d}z. \tag{A.43}$$

This magnification matrix is parametrized by a convergence κ and shear parameters γ_1 and γ_2

$$\mathbf{M}(\vec{\theta}) = \begin{pmatrix} 1+\kappa+\gamma_1 & \gamma_2 \\ \gamma_2 & 1+\kappa-\gamma_1 \end{pmatrix}. \tag{A.44}$$

The weak lensing limit assumes $\kappa^2 \ll 1$ and $\gamma_i^2 \ll 1$. The convergence still cannot be measured directly as the size and flux of the source is generally unknown. However, the shear components can be measured statistically averaging galaxy image distortions over large sample of galaxies since the orientation of galaxies are assumed to be random. Weak lensing thus offers a probe of the sum of the two potentials $(\Phi+\Psi)$.

A.3.3 Current Limits

Using the Shapiro time delay one can obtain strong limits on the *gravitational slip* (combination $\Psi-\Phi$) in the solar system. The round-trip time of signals from the Cassini spacecraft near Saturn as the signals pass close to the sun is longer than one would expect in flat spacetime. This gives tight limit on the slip [19]

$$\frac{|\Psi-\Phi|}{\Phi} = (2.1\pm2.3)\cdot10^{-5} \tag{A.45}$$

within the solar system. Combining stellar dynamics with the strong gravitational lensing on galaxy scales limit the slip [101]

$$\frac{|\Psi-\Phi|}{\Phi} = 0.01\pm0.05 \tag{A.46}$$

on kpc scales. Future surveys such as the LSST and Euclid will improve these limits and provide new one on larger scales.

A.4 Action Principle

To obtain various equations of motion, the well known action principle is used. Since the variation with respect to the metric field $g^{\mu\nu}$ can be tricky, we described here in detail these variations for $f(R)$ gravity as an example, from which equations of motion for other theories can be obtained easily.

Action for $f(R)$ gravity (and in a special case for General Relativity) is

$$S = \int \mathrm{d}^4x\sqrt{-g}\left[\frac{M_{pl}^2}{2}F(R) + \mathcal{L}_M\right], \tag{A.47}$$

where $\mathcal{L}_M$ is the Lagrangian density of matter (or dark energy) and $F(R)\equiv R+f(R)$ is an arbitrary function of the Ricci scalar. According to the action principle a variation of this action with respect to the inverse metric $g^{\mu\nu}$ is zero

$$0 = \delta S = (\delta S)_1 + (\delta S)_2 + (\delta S)_3 + (\delta S)_M, \tag{A.48}$$

where

$$
\begin{aligned}
(\delta S)_1 &= \frac{M_{pl}^2}{2}\int \mathrm{d}^4x F(R)\delta\sqrt{-g},\\
(\delta S)_2 &= \frac{M_{pl}^2}{2}\int \mathrm{d}^4x \sqrt{-g}F_{,R}R_{\mu\nu}\delta g^{\mu\nu},\\
(\delta S)_3 &= \frac{M_{pl}^2}{2}\int \mathrm{d}^4x \sqrt{-g}F_{,R}g^{\mu\nu}\delta R_{\mu\nu},\\
(\delta S)_M &= \int \mathrm{d}^4x \delta\left(\sqrt{-g}\mathcal{L}_M\right),
\end{aligned}
\tag{A.49}
$$

The variation of the determinant $\sqrt{-g}$ in $(\delta S)_1$ is according to the Jacobi's formula given by

$$
\delta\sqrt{-g} = -\frac{1}{2}\frac{1}{\sqrt{-g}}\delta g = \frac{1}{2}\sqrt{-g}(g^{\mu\nu}\delta g_{\mu\nu}) = -\frac{1}{2}\sqrt{-g}g_{\mu\nu}\delta g^{\mu\nu}. \tag{A.50}
$$

In the second term $(\delta S)_2$ is already the variation $\delta g^{\mu\nu}$. To calculate the variation $(\delta S)_3$ we must know the variations of the Riemann tensor and the Ricci tensor. Variation of the Riemann tensor is

$$
\delta R^{\rho}_{\sigma\mu\nu} = \partial_\mu\delta\Gamma^{\rho}_{\sigma\nu} + \delta\Gamma^{\rho}_{\mu\lambda}\Gamma^{\lambda}_{\sigma\nu} + \Gamma^{\rho}_{\mu\lambda}\delta\Gamma^{\lambda}_{\sigma\nu} - (\mu\leftrightarrow\nu). \tag{A.51}
$$

The variation $\delta\Gamma^{\rho}_{\sigma\nu}$ is the difference of two connections and therefore a tensor. Its covariant derivative is

$$
\nabla_\lambda\left(\delta\Gamma^{\rho}_{\sigma\nu}\right) = \partial_\lambda\left(\delta\Gamma^{\rho}_{\sigma\nu}\right) + \Gamma^{\rho}_{\lambda\mu}\delta\Gamma^{\mu}_{\sigma\nu} - \Gamma^{\mu}_{\lambda\sigma}\delta\Gamma^{\rho}_{\mu\nu} - \Gamma^{\mu}_{\lambda\nu}\delta\Gamma^{\rho}_{\sigma\mu}. \tag{A.52}
$$

From equations (A.51) and (A.52) it can be seen that the variation of the Riemann tensor is equal to the difference of two covariant derivative of connections. The variation of the Ricci tensor is given by the contraction of the Riemann tensor

$$
\delta R_{\mu\nu} = \delta R^{\rho}_{\mu\rho\nu} = \nabla_\rho\left(\delta\Gamma^{\rho}_{\mu\nu}\right) - \nabla_\nu\left(\delta\Gamma^{\rho}_{\rho\mu}\right). \tag{A.53}
$$

We can replace $\delta\Gamma^{\rho}_{\mu\nu}$ in terms of $\delta g^{\mu\nu}$ throughout the Christoffel symbols

$$
\delta\Gamma^{\rho}_{\mu\nu} = -\frac{1}{2}\left[g_{\lambda\mu}\nabla_\nu(\delta g^{\lambda\rho}) + g_{\lambda\nu}\nabla_\mu(\delta g^{\lambda\rho}) - g_{\mu\alpha}g_{\nu\beta}\nabla^\rho(\delta g^{\alpha\beta})\right]. \tag{A.54}
$$

Therefore, the variation $(\delta S)_3$ is

$$
(\delta S)_3 = \frac{M_{pl}^2}{2}\int \mathrm{d}^4x\sqrt{-g}F_{,R}\nabla_\sigma\left[g_{\mu\nu}\nabla^\sigma(\delta g^{\mu\nu}) - \nabla_\lambda(\delta g^{\sigma\lambda})\right]. \tag{A.55}
$$

Now, for any four-vector holds equivalency between its derivative and covariant derivative [120]

$$
\nabla_\mu A^\mu = \frac{1}{\sqrt{-g}}\partial_\mu(\sqrt{-g}V^\mu), \tag{A.56}
$$

which we can use together with the Stoke's theorem to integrate the action $(\delta S)_3$ per partes. If we assume that the variations of the metric and its derivative vanish at the surface, after two integrations we get

$$
(\delta S)_3 = \frac{M_{pl}^2}{2}\int \mathrm{d}^4x\sqrt{-g}\left[g_{\mu\nu}\Box F_{,R} - \nabla_\mu\nabla_\nu F_{,R}\right]\delta g^{\mu\nu}. \tag{A.57}
$$

To calculate $(\delta S)_M$ we use the definition of the stress-energy tensor

$$T_{\mu\nu} \equiv \frac{-2}{\sqrt{-g}} \frac{\delta(\sqrt{-g}\mathcal{L}_M)}{\delta g^{\mu\nu}}. \tag{A.58}$$

Putting all four parts of the action together we get

$$\delta S = \frac{M_{pl}^2}{2} \int \mathrm{d}^4x\sqrt{-g} \left[F_{,R}R_{\mu\nu} - \frac{1}{2}Fg_{\mu\nu} + g_{\mu\nu}\Box F_{,R} - \nabla_\mu\nabla_\nu F_{,R} - \frac{1}{M_{pl}^2}T_{\mu\nu} \right] \delta g^{\mu\nu}. \tag{A.59}$$

Restoring $F(R) = R + f(R)$ this gives the equation of motion

$$G_{\mu\nu} + f_{,R}R_{\mu\nu} - \frac{1}{2}fg_{\mu\nu} + g_{\mu\nu}\Box f_{,R} - \nabla_\mu\nabla_\nu f_{,R} = \frac{1}{M_{pl}^2}T_{\mu\nu}, \tag{A.60}$$

where $G_{\mu\nu} \equiv R_{\mu\nu} - \frac{1}{2}Rg_{\mu\nu}$ is the Einstein tensor.

B. C++ Implementation

Here we describe the implementation of used methods in C++ language with extended comments. We present here only the most relevant parts of the code, e.g. we omit overloaded versions of the functions and some auxiliary functions. The whole code can be found on an enclosed CD or by sending me an email at vrastil@fzu.cz.

In our program we are using following libraries,

```
#include "stdafx.h" // standard pre-compiled headers
#include <math.h> // common mathematical operations
#include "limits.h" // fundamental constants
#include <iostream> // standard input/output stream objects
#include <fstream> // provides file stream classes
#include <stdlib.h> // C Standard General Utilities Library
#include <functional> // function-like objects
```

and the namespace

```
using namespace std;
```

We are often dealing with the functions (scalar or vector) of the form $f(t, \boldsymbol{x})$, so we define a `type`

```
typedef function<double(double, double*)> t_function;
```

B.1 Runge-Kutta Method with Adaptive Stepsize

The Runge-Kutta method[1] includes two main functions – the `Runge_Kutta_step` for the Runge-Kutta algorithm and the `Runge_Kutta_adap_step` for the adaptive stepsize. It also includes two smaller functions `shift` and `fce` which we separated from the main functions to increase clarification of the program.

Function `shift` is an equivalence of the sum of vectors $\boldsymbol{y}_0$ and $h \cdot \boldsymbol{shift}$, the outcome is stored in the vector $\boldsymbol{y} = \boldsymbol{y}_0 + h \cdot \boldsymbol{shift}$. The function `fce` evaluates the vector function $\boldsymbol{f}$ and stores the outcome in $\boldsymbol{y} = \boldsymbol{f}(t_0, \boldsymbol{x}_0)$.

```
void shift(double *y, double *y_0, double *shift, double h,
    int dim){
 for (int i = 0; i < dim; i++){
  y[i] = y_0[i] + h*shift[i];
 }
}

void fce(double *y, t_function *f, double t_0, double *x_0,
    int dim){
```

[1] These parts of the code are from the header file `runge_integ_root.h`.

```
 for (int i = 0; i < dim; i++){
  y[i] = f[i](t_0, x_0);
 }
}
```

Function `Runge_Kutta_step` performs one step of the length h in the integration of ordinary differential equations $\dot{\boldsymbol{y}} = \boldsymbol{f}(t, \boldsymbol{y})$.

```
void Runge_Kutta_step(double &t_0, double *y_0, double h,
   t_function *f, int dim){

 double *k1 = new double[dim];
 double *k2 = new double[dim];
 double *k3 = new double[dim];
 double *k4 = new double[dim];
 double *y_h = new double[dim];

 fce(k1, f, t_0, y_0, dim);

 shift(y_h, y_0, k1, h / 2, dim);
 fce(k2, f, t_0 + h / 2, y_h, dim);

 shift(y_h, y_0, k2, h / 2, dim);
 fce(k3, f, t_0 + h / 2, y_h, dim);

 shift(y_h, y_0, k3, h, dim);
 fce(k4, f, t_0 + h, y_h, dim);

 t_0 += h;
 shift(y_0, y_0, k1, h / 6, dim);
 shift(y_0, y_0, k2, h / 3, dim);
 shift(y_0, y_0, k3, h / 3, dim);
 shift(y_0, y_0, k4, h / 6, dim);

 delete[] k1;
 delete[] k2;
 delete[] k3;
 delete[] k4;
 delete[] y_h;
}
```

Function `Runge_Kutta_adap_step` controls the size of the step h_{in}. One can also require some lower and/or upper limit on size of the step. The function counts number of rejected steps to prevent an infinite reiteration in case of ill-defined problems.

```
void Runge_Kutta_adap_step(double &t_0, double *y_0, double
   &h_in, double h_min, double h_max, double atol, double
   rtol, t_function *f, int dim, int &N_iter){
 if (N_iter>30) Runge_Kutta_step(t_0, y_0, h_in, f, dim);
```

```
    // prevents from an infinite loop, h_out = h_in *1e-21
  else {
   if ((h_in > h_max) && h_max != 0) h_in = h_max;
   if (h_in < h_min) h_in = h_min;

   double err_h = 0;
   double scale;
   double dh;
   double * yh = new double[dim];
   double * y1 = new double[dim];
   for (int i = 0; i < dim; i++){
    yh[i] = y_0[i];
    y1[i] = y_0[i];
   }

   Runge_Kutta_step(t_0, y1, h_in, f, dim);
     // one step of h
   t_0 -= h_in;
   Runge_Kutta_step(t_0, y_0, h_in / 2, f, dim);
   Runge_Kutta_step(t_0, y_0, h_in / 2, f, dim);
     // two steps of h/2

   for (int i = 0; i < dim; i++){
    scale = atol + rtol*abs(y_0[i]);
    err_h += pow((y_0[i] - y1[i]) / scale, 2);
   }
   err_h = sqrt(err_h / dim);
   if (err_h == 0) dh = 10;
   else dh = 0.9*pow(1 / err_h, 1.0 / 5);
   if (dh > 10) dh = 10;
     // maximal increase of the stepsize by a factor 10 or
   if (dh < 1 / 5.0) dh = 1 / 5.0;
     // decrease by a factor 5
   if (err_h < 1){
    if (N_iter == 0) h_in *= dh;
     // no increase if previous step fails
   }
   else{
    t_0 -= h_in; // go back
    for (int i = 0; i < dim; i++){
     y_0[i] = yh[i];
    }
    delete[] y1;
    delete[] yh;
    h_in *= dh; // adjust h
    N_iter++;
    Runge_Kutta_adap_step(t_0, y_0, h_in, h_min, h_max,
       atol, rtol, f, dim, N_iter); // reiterate
   }
  }
}
```

B.2 Shooting Method

The shooting method algorithm[2] consists of two parts. First part is the classical root-finder algorithm and the other one is how to convert an integration of ordinary differential equations into a function of one variable.

Function `root_finder` takes two initial guesses of equation $fce(x) - f_{eq} = 0$ which satisfy $(fce(x_1) - f_{eq})(fce(x_2) - f_{eq}) < 0$. It returns the root with given relative and absolute tolerances in variable x_1.

```
void root_finder(double &x1, double &x2,
   function<double(double)> fce_x, double f_eq, double
   x_rtol, double x_atol, double f_atol){
 double f1, f2, fh, xh;
 bool f_acc = true;
 bool x_acc = true;
 double scale;
 f1 = fce_x(x1) - f_eq;
 f2 = fce_x(x2) - f_eq;
 while ((f_acc) && (x_acc)){
  fh = f2;
  xh = x2;
  x2 = (x2 + x1) / 2;
  f2 = fce_x(x2) - f_eq;
  if (f1*f2 > 0){
   x1 = xh;
   f1 = fh;
  }
  scale = x_atol + x2*x_rtol;
  x_acc = (abs(x1 - x2) / scale) > 1;
  scale = f_atol;
  f_acc = abs(f2 / scale) > 1;
 }
 if (abs(f1) > abs(f2)){
  xh = x2;
  x2 = x1; // x1 <=> |f1| < |f2|
  x1 = xh;
 }
}
```

The demand for the knowledge of two guesses in `root_finder` can be a bit problematic in the shooting method. One usually has at best one guess and an estimation in which direction should lie the other one. The function `get_x1_x2` is finding the other guess based on the first guess and given multiplier which defines the direction. If the sign does not change after 100 multiplications the function tries to find the root in the opposite direction.

```
void get_x1_x2(double &x1, double &x2,
   function<double(double)> fce, double f_eq, double mlt){
 double xh = x1;
```

[2]These parts of the code are from the header file `runge_integ_root.h`.

```
 int N_h = 0;
 double f1, f2;

 x2 = x1;
 f2 = fce(x2) - f_eq;
 do {
  x1 = x2;
  x2 *= mlt;
  f1 = f2;
  f2 = fce(x2) - f_eq;
  N_h++;
 } while ((f1*f2 > 0) && (N_h < 100));
 if (N_h < 100) return;

 x2 = xh;
 f2 = fce(x2) - f_eq;
 mlt = 1 / mlt;
 N_h = 0;
 do {
  x1 = x2;
  x2 *= mlt;
  f1 = f2;
  f2 = fce(x2) - f_eq;
  N_h++;
 } while ((f1*f2 > 0) && (N_h < 100));
}
```

Function `integrate` integrates a differential equation with initial conditions specified in $fce_{min}(s, t, \boldsymbol{y})$. It integrates the equations till $t_{max} =$ `true`. The function $t_{max}(t, \boldsymbol{y})$ can be simply of the form $t < t_1$ but in principle it can contain arbitrary condition, e.g. we are often using the condition $\delta\phi/\phi_{inf} < \epsilon$ as discussed in Chapter 4. Function `integrate_fmax` in addition to `integrate` returns a boundary condition at the end of the integration. Boundary conditions (whether Dirichlet, Neumann or Robin b.c.) are specified in $fce_{max}(t, \boldsymbol{y})$.

```
void integrate(double s, double &t, double *y,
   function<bool(double, double*)>t_max,
   function<void(double, double &, double*)>fce_min, double
   err, t_function *f_diff, int dim){
 double h = 1;
 fce_min(s, t, y);
 while (t_max(t, y)){
  Runge_Kutta_adap_step(t, y, h, err, f_diff, dim);
 }
}

double integrate_fmax(double s, function<bool(double,
   double*)>t_max, function<void(double, double &,
   double*)>fce_min, t_function fce_max, double err,
   t_function *f_diff, int dim){
 double *y = (double*)malloc(dim*sizeof(double));
```

```
 double t = 0;
 integrate(s, t, y, t_max, fce_min, err, f_diff, dim);
 return fce_max(t, y);
}
```

Next we need to convert initial conditions and the integration into a function of one variable to feed functions `get_x1_x2` and `root_finder`. This is done using the function template `std::bind` defined in the header `<functional>`. In `shoot_meth` we create a function $fce(s)$ of one variable from `integrate_fmax` by filling all of its arguments but the first.

```
double shoot_meth(double s1, double mlt,
   function<bool(double, double*)>t_max,
   function<void(double, double &, double*)>fce_min,
 t_function fce_max, double err, t_function *f_diff, int
    dim, double scale){
 // s1, mlt -- first guess and a multiplier to obtain other
    guesses
 // initial conditions is specified in fce_min with
    parameter s
 // integrate till t_max is true
 // boundary conditions at t=t_max are specified in
    fce_max, return 0 if achieved
 double s2 = 0;

 auto fce_s = bind(integrate_fmax, placeholders::_1, t_max,
    fce_min, fce_max, err, f_diff, dim);
 get_x1_x2(s1, s2, fce_s, mlt);
 root_finder(s1, s2, fce_s, scale);
 return s1;
}
```

B.3 Planar Slab

Here we presented the code[3] for solving the chameleon field in a planar slab. It is the application of the previous methods in a concrete case. We have used constants

```
const double M_L = 2.4e-3;
const double n_pl = 3.0;
const double gamma = 1;
const double rho_pl = 1e-11;
const double phi_min = M_L*sgn(1 - n_pl)*
   pow(B*rho_pl/(abs(n_pl)*gamma*pow(M_L,3)*Mp),1/(1-n_pl));
const double phi_s = phi_min*(1 - 1 / n_pl);
const double K = sqrt((n_pl - 2)*(n_pl - 2)*gamma*pow(M_L,
   4 - n_pl)*pow(abs(phi_s), n_pl - 2) / 2);
```

[3]These parts of the code are from the header file `planar_slab.h`.

The main routine `slv_planar_slab` takes as an argument maximal `z` till which integrate and a desired accuracy `err` (relative and absolute tolerance). Into the array `phi` are stored values of the field with z separation `step` and an integer variable `N_i` counts the total number of stored values.

```
void slv_planar_slab(double r_max, double err, double
   **phi, double step, int &N_i){
 t_function phi_vec_eq[] = { phi_0_der, phi_pl_1_der };
 double h = 1;
 int i = -1;

 double phi_der_0 = get_phi_pl_der(r_max, err);
 double phi_vec[2] = { phi_s, phi_der_0 };

 double r = 0;
 auto integrate_pl = bind(is_integrate_pl,
    placeholders::_1, placeholders::_2, r_max);
 integrate_cout(r, phi_vec, integrate_pl, err, phi_vec_eq,
    2, phi, step, 1, 0, i);
 N_i = i;
}
```

`phi_vec_eq` defines the differential equation we want to integrate, i.e. two equations of the first order with $\mathrm{d}\phi_0/\mathrm{d}z = \phi_1$ and $\mathrm{d}\phi_1/\mathrm{d}z = V_{,\phi}(\phi_0)$.

```
double phi_0_der(double r, double *phi){
 return phi[1];
}

double phi_pl_1_der(double r, double *phi){
 double tmp = V_pl_der(phi[0]);
 if (tmp != tmp){
  return 0;
 }
 return tmp;
}

double V_pl_der(double phi){
 if (phi > 0) return n_pl*gamma*pow(M_L, 4 - n_pl)*
    pow(phi, n_pl - 1);
 else return -n_pl*gamma*pow(M_L, 4 - n_pl)*pow(-phi, n_pl
    - 1);
}
```

The function `get_phi_pl_der` returns the derivative $\mathrm{d}\phi/\mathrm{d}z(0)$ via the shooting method.

```
double get_phi_pl_der(double r_max, double err){
 double h = 1;
 double s1;
```

```
 t_function phi_vec_eq[] = { phi_0_der, phi_pl_1_der };
 double r_mlt = 1;
 double f1;

 if (n_pl > 2) s1 = -K*phi_s * 2 / (n_pl - 2);
   // exact initial condition
 else {
  s1 = K*phi_s; // first guess is phi(0)/z_c
  do{
   auto integrate_pl = bind(is_integrate_pl,
      placeholders::_1, placeholders::_2, r_max*r_mlt);
   s1 = shoot_meth(s1, 0.9, integrate_pl, fce_min_phi_0,
      fce_max_pl, err, phi_vec_eq, 2, phi_s / r_max);
   f1 = integrate_fmax(s1, integrate_pl, fce_min_phi_0,
      fce_max_pl, err, phi_vec_eq, 2);
   r_mlt *= 0.9;
  } while ((abs(f1 / (phi_s / r_max)) > 1) && (r_mlt >
     0.1)); // if the integration fails
 }
 return s1;
}
```

The function `integrate_pl` tells the routine `integrate` or `shoot_meth` described in previous section when to stop the integration (in this case just till $z < r_{max}$), `fce_min_phi_0` specifies initial conditions (in this case the shooting parameter s_1 is directly the derivative $\mathrm{d}\phi/\mathrm{d}z(0)$) and the function `fce_max_pl` returns Robin boundary condition (0 if achieved).

The routine `integrate_cout`[4] is similar to the routine `integrate` while now it also stores the values of the chameleon field (`reg = 0`) or its derivative (`reg = 1`) into the field `chi`.

```
void integrate_cout(double &t, double *y,
   function<bool(double, double*)>t_max, double err,
   t_function *f_diff, int dim, double **chi, double step,
   double mlt, int reg, int &i){
 double h = step;
 double h_max = step;
 i++;
 chi[0][i] = t;
 chi[1][i] = y[reg] * mlt;
 while (t_max(t, y)){
  Runge_Kutta_adap_step(t, y, h, 0,h_max, err, f_diff, dim);
  if (t > R) {
   h_max = R200;
  }
  if (t > R200) {
   h_max = 0;
  }
```

[4]The routine `integrate_cout` and also the next subroutine `if_low_memory` are from the header file `runge_integ_root.h`.

```
  if ((t - chi[0][i]) >= step){
   if(t>R) step *= 1.5;
   i++;
   if_low_memory(i, h_N, h_re, chi,2);
   chi[0][i] = t;
   chi[1][i] = y[reg] * mlt;
  }
 }
}
```

The subroutine `if_low_memory` checks if there is enough allocated space for the field `chi`. In a case that did not it reallocates the allocated memory with an additional one.

```
void if_low_memory(int i, int &i_max, int i_re, double
   **chi, int dim){
 if (i >= i_max){
  for (int j = 0; j < dim; j++){
   chi[j] = (double*)realloc(chi[j], (i_max +
      i_re)*sizeof(double));
  }
  i_max += i_re;
 }
}
```

B.4 Stars

The structure of the code[5] in case of the stars is different than in the case of a planar slab. We now have to deal with linear and non-linear case separately (which means two completely different ways of determining initial conditions) and since $r \sim 1/m_\infty$ we also have to treat the solution analytically rather than using a brute force and a numerical solution.

The main routine `slv_Chameleon_star` takes as arguments similar variables as in a case of planar slab – max radius `r_max`, desired accuracy `err`, array `chi` for storing values with r-separation `step` and an integer variable `N_i` for counting the total number of stored values. The procedure stores values of the field or its derivative based on an integer variable `reg` (0 for potential, 1 for force).

The procedure first determines whether the solution is in the linear or non-linear regime base on the value r_{eq} and then computes the initial conditions via the shooting method. Note that in the linear regime the integration starts at $r = 0$ whereas in the non-linear regime at $r = R_{roll}$ (at the code this value is denoted by `r2`). Next the equations are integrated till we enters the exponentially damped phase. In this phase we integrate only one-dimensional differential equation where we use the analytical (linearized) solution for the derivative of the field with an amplitude based on previous numerical solution. This ensures the continuity of the field and its derivative.

[5] These parts of the code are from the header file `stars_NFW.h`.

```
void slv_Chameleon_star(double r_max, double err, double
   **chi, double &step, int &N_i, int reg){
 double h = step;
 double eps = 1e-2;
 t_function chi_vec_eq[] = { chi_0_der, chi_1_der };
 double chi_pot_0;
 if ((pot_new(0) + Ys) <= 0) chi_pot_0 = chi_B;
   // non-linear regime
 else chi_pot_0 = get_chi_0_star(err, eps); // linear regime
 double chi_der_0 = 0;
 double r = 0;
 int i = 0;
 double chi_vec[2] = { chi_pot_0, chi_der_0 };

 if (abs(chi_pot_0 - chi_B) / chi_B < eps){
   // non-linear regime
  double m = sqrt(V_eff_2nd_derr(chi_B));
  double r2;
  if (r_eq>0){
   r2 = shoot_meth_star(err, eps);
   chi[0][i] = 0;
   chi[1][i] = (1 - reg)*chi_B*(1 + eps*m*r2 / sinh(m*r2));
  }
  else{
   r2 = 0;
   chi[0][i] = 0;
   chi[1][i] = (1-reg)*chi_B*(1 + eps);
  }

  double shr_d_shr2, chr_d_shr2;
    // sinh(r) / sinhr(r2), cosh(r) / sinhr(r2)

  for (r = step; r < r2; r += step){
   i++;
   chi[0][i] = r;

   if (m*r>30){
    shr_d_shr2 = exp(m*(r - r2));
      // approximation 2*sinh(x)=e^x
    chr_d_shr2 = shr_d_shr2;
   }
   else{
    shr_d_shr2 = sinh(m*r) / sinh(m*r2);
    chr_d_shr2 = cosh(m*r) / sinh(m*r2);
   }

   if (reg == 0) chi[1][i] = chi_B*(1 + eps*r2 / r *
      shr_d_shr2);
   else chi[1][i] = -B / Mp*chi_B*eps * r2 /
      (r*r)*(m*r*chr_d_shr2 - shr_d_shr2);
  }
```

```
  if ((R - r2) / R < 1e-6){ // no-shell solution
   r = R;
   chi_vec[0] = chi_B + (chi_0 - chi_B) / (m*R)*tanh(m*R);
   chi_vec[1] = (chi_0 - chi_B)*(m_inf*R + 1) / (R*R)*(R -
      tanh(m*R) / (m*R));
  }
  else{
   r = r2;
   chi_vec[0] = chi_B*(1 + eps);
   chi_vec[1] = chi_B*eps / r2*(m*r2 / tanh(m*r2) - 1);
  }
 }
 else i--;
 auto integrate_star = bind(is_integrate, placeholders::_1,
    placeholders::_2, 1 / m_inf);
 double mlt = 1;
 if (reg == 1) mlt *= -B / Mp;
   // F_\phi = -\beta/\Mpl * \dd\phi / \dd r

 integrate_cout(r, chi_vec, integrate_star, err,
    chi_vec_eq, 2, chi, step, mlt, reg, i);

 double a = chi_vec[1] * r*r*exp(m_inf*r) / (m_inf*r + 1);
 chi_vec_eq[0] = bind(chi_0_der_lin, placeholders::_1,
    placeholders::_2, a);
 while (r < r_max){
  Runge_Kutta_adap_step(r, chi_vec, h, err, chi_vec_eq, 1);
  chi_vec[1] = a*exp(-m_inf*r) / (r*r)*(m_inf*r + 1);
  if ((r - chi[0][i]) >= step){
   step *= 2;
   i++;
   chi[0][i] = r;
   chi[1][i] = chi_vec[reg] * mlt;
  }
 }
 N_i = i;
}
```

Some of the smaller functions used previously and in the next code.

```
bool is_integrate(double r, double *y, double r_max){
 if ((r_max != 0) && (r > r_max)) return false;
 if (r < R200) return true;
 return abs(chi_0 - y[0]) / chi_0 > 1e-2;
}

double V_eff_der(double r, double chi){
 double v = B / Mp*(rho_r(r) - rho_0*pow(chi_0 / abs(chi),
    1 - n));
 if ((v != v) || (isinf(v))){
  return 0;
```

```
 }
 return v;
}

double V_eff_2nd_derr(double chi){
 return B / Mp*rho_0*(1 - n)*pow(chi / chi_0, n)*chi_0 /
    (chi*chi);
}

double chi_0_der(double r, double *chi){
 return chi[1];
}

double chi_0_der_lin(double r, double *chi, double a){
 return a*exp(-m_inf*r) / (r*r)*(m_inf*r + 1);
}

double chi_1_der(double r, double *chi){
 if (r == 0) return V_eff_der(r, chi[0]) / 3;
 else return V_eff_der(r, chi[0]) - 2 / r*chi[1];
}

void fce_min_r2(double s, double &t_0, double *y_0, double
   eps, double m){
 switch (mod){
 case 0:{ // stars
      t_0 = s;
      y_0[0] = chi_B*(1 + eps);
      y_0[1] = chi_B*eps / s*(m*s / tanh(m*s) - 1);
 }
 case 1:{ // NFW halo
      t_0 = s;
      m = sqrt(V_eff_2nd_derr(chi_bulk_r(t_0)));
      y_0[0] = chi_bulk_r(s)*(1 + eps);
      y_0[1] = chi_bulk_der(s)*(1 + eps) +
         chi_bulk_r(s)*eps / s*(m*s / tanh(m*s) - 1);

 }
 }
}

void fce_min_chi_0(double s, double &t_0, double *y_0){
 switch (mod){
 case 0:{ // stars
      t_0 = 0;
      y_0[0] = s;
      y_0[1] = 0;
 }
 case 1:{ // NFW halo
      t_0 = 0;
      y_0[0] = s;
```

```
      y_0[1] = -(s - chi_0) / (2 * R)*(c + 1) / c;
        // Newtonian relationship between potential and
           derivative for NFW halo
 }
 }
}
double fce_max(double r, double *y){
 double dchi = y[0] - chi_0;
 if (dchi < 0) return (y[1] * r + dchi*(m_inf*r + 1));
 else return 10 * (y[1] * r + dchi*(m_inf*r + 1));
}
```

Two shooting routines `shoot_meth_star` (non-linear regime) and `get_chi_0_star` (linear regime) return parameter R_{roll} and $\phi(0)$ respectively.

```
double shoot_meth_star(double err, double eps){
 double m = sqrt(V_eff_2nd_derr(chi_B));
 double h = 1;
 double r2a = R - Mp*(chi_0 - chi_B) / (B*rho_c*R*R)*R;
  // analytical value of r2
 double s1;
 if (r_eq<r2a) s1 = r_eq;
 else s1 = r2a;
 if (s1 > R) return R;
 auto fce_min_star = bind(fce_min_r2, placeholders::_1,
    placeholders::_2, placeholders::_3, eps, m);
 auto integrate_star = bind(is_integrate, placeholders::_1,
    placeholders::_2, 1 / m_inf);
 t_function f_diff[] = { chi_0_der, chi_1_der };

 return shoot_meth(s1, 0.7, integrate_star, fce_min_star,
    fce_max, err, f_diff, 2, chi_0*eps);
}

double get_chi_0_star(double err, double eps){
 double h = 1;
 double s1 = chi_0 + 1 * 2 * B*Mp*pot_star(0);
  // guess from the analytical solution
 auto integrate_star = bind(is_integrate, placeholders::_1,
    placeholders::_2, 1 / m_inf);
 t_function f_diff[] = { chi_0_der, chi_1_der };

 return shoot_meth(s1, 0.95, integrate_star, fce_min_chi_0,
    fce_max, err, f_diff, 2, chi_0*eps);
}
```

B.5 NFW Halo

The structure of the code[6] in case of the NFW halo is rather similar to the case of stars. At first, the main routine `slv_Chameleon_NFW` determines which regime we are in. Then it computes the initial conditions via the shooting method, integrate the equations till we are near the background and finally integrate one-dimensional differential equation with derivative obtained from the analytical solution till `r_max`.

```
void slv_Chameleon_NFW(double r_max, double err, double
   **chi, double &step, int &N_i, int reg){
 double h = step;
 double eps = 1e-2;
 t_function chi_vec_eq[] = { chi_0_der, chi_1_der };
 double s;
 if ((pot_NFW(0) + Ys) <= 0) s = 0;
 else s = get_chi_0_NFW(err, eps);
 double r;
 int i = 0;
 double chi_vec[2];
 fce_min_chi_0(s, r, chi_vec);

 if (s == 0){ // screening regime
  double m;
  double r2 = shoot_meth_NFW(err, eps);
  chi[0][i] = 0;
  chi[1][i] = 0;
  double shr_d_shr2, chr_d_shr2;
  for (r = step; r < r2; r += step){
   i++;
   if_low_memory(i, h_N, h_re, chi, 2);
   m = sqrt(V_eff_2nd_derr(chi_bulk_r(r)));
   chi[0][i] = r;

   if (m*r>30){ // approximation for m*r>>1
    shr_d_shr2 = exp(m*(r - r2));
      // approximation 2*sinh(x)=e^x
    chr_d_shr2 = shr_d_shr2;
   }
   else{
    shr_d_shr2 = sinh(m*r) / sinh(m*r2);
    chr_d_shr2 = cosh(m*r) / sinh(m*r2);
   }

   if (reg == 0) chi[1][i] = chi_bulk_r(r)*(1 + eps*r2 / r
      * shr_d_shr2);
   else chi[1][i] = -B / Mp*(chi_bulk_der(r)*(1 + eps*r2 /
      r * shr_d_shr2) + chi_bulk_r(r)*eps * r2 /
      (r*r)*(m*r*chr_d_shr2 - shr_d_shr2));
```

[6] These parts of the code are from the header file `stars_NFW.h`.

```
  }
  r = r2;
  m = sqrt(V_eff_2nd_derr(chi_bulk_r(r)));
  chi_vec[0] = chi_bulk_r(r)*(1 + eps);
  chi_vec[1] = chi_bulk_der(r)*(1 + eps) +
     chi_bulk_r(r)*eps / r*(m*r / tanh(m*r) - 1);
 }
 else i--;

 auto integrate_star = bind(is_integrate, placeholders::_1,
    placeholders::_2, 1 / (1 * m_inf));
 double mlt = 1;
 if (reg == 1) mlt *= -B / Mp;

 integrate_cout(r, chi_vec, integrate_star, err,
    chi_vec_eq, 2, chi, step, mlt, reg, i);

 double a = chi_vec[1] * r*r*exp(m_inf*r) / (m_inf*r + 1);
 chi_vec_eq[0] = bind(chi_0_der_lin, placeholders::_1,
    placeholders::_2, a);

 while (r < r_max){
  Runge_Kutta_adap_step(r, chi_vec, h, err, chi_vec_eq, 1);
  chi_vec[1] = a*exp(-m_inf*r) / (r*r)*(m_inf*r + 1);
  if ((r - chi[0][i]) >= step){
   step *= 2;
   i++;
   if_low_memory(i, h_N, h_re, chi, 2);
   chi[0][i] = r;
   chi[1][i] = chi_vec[reg] * mlt;
  }
 }

 N_i = i;
}
```

We are also using some smaller functions.

```
double chi_bulk(double rho){
 return chi_0*pow(rho_0 / rho, 1 / (1 - n));
}

double chi_bulk_der(double r){
 double x = r / R;
 switch (mod){
 case 0:return 0;
 case 1:return 1 / R*chi_0*pow(rho_0 / rho_c, 1 / (1 - n))
    / (1 - n)*pow(x*(1 + x)*(1 + x), n / (1 - n))*((1 +
    x)*(1 + x) + 2 * x*(1 + x));
 }
}
```

```
double chi_bulk_r(double r){
 return chi_0*pow(rho_0 / rho_r(r), 1 / (1 - n));
}
```

Two shootings method for determining initial values.

```
double shoot_meth_NFW(double err, double eps){
 double h = 1;
 double s1 = r_eq;
 auto fce_min_star = bind(fce_min_r2, placeholders::_1,
    placeholders::_2, placeholders::_3, eps, 0);
 auto integrate_star = bind(is_integrate, placeholders::_1,
    placeholders::_2, 1 / m_inf);
 t_function f_diff[] = { chi_0_der, chi_1_der };

 return shoot_meth(s1, 0.5, integrate_star, fce_min_star,
    fce_max, err, f_diff, 2, chi_0*eps);
}

double get_chi_0_NFW(double err, double eps){
 double h = 1;
 double s1 = chi_0 + 2 * B*Mp*pot_NFW(0);
   // guess from the analytical solution
 auto integrate_star = bind(is_integrate, placeholders::_1,
    placeholders::_2, 1 / (1 * m_inf));
 t_function f_diff[] = { chi_0_der, chi_1_der };

 return shoot_meth(s1, 0.95, integrate_star, fce_min_chi_0,
    fce_max, err, f_diff, 2, eps*chi_0*m_inf*1e3);
}
```

B.6 N-body simulations

We present here part of the N-body algorithm[7], namely the computation of the forces. We focused on this part as for the chameleon gravity the set up of the initial condition as well as the integration of equations of motion remains the same as for standard N-body simulation. These parts are completely separate from previous section. In this part we are using following libraries

```
#include "stdafx.h" // standard pre-compiled headers
#include <math.h> // common mathematical operations
#include <iostream> // standard input/output stream objects
#include <fstream> // provides file stream classes
#include <stdlib.h> // C Standard General Utilities Library
#include <fftsg.c> // 1-D FFT
#include <fftsg2d.c> // 2-D FFT
```

[7]These parts of the code are from the source file `FFT_Poisson.cpp`.

```
#include <fftsg3d.c> // 3-D FFT
```

Libraries for Fourier transforms are publicly available at [89]. We are using the namespace

```
using namespace std;
```

For particles we define a (public) class and for widely used arrays types

```
typedef int tVector_I[3];
typedef double tVector_D[3];
struct particle {
 double x;
 double y;
 double z;
 double mass;
 double vx;
 double vy;
 double vz;
};
```

As we are dealing (for now) only with the force computation and not the equations integration, the velocity parameters are not used. We are using two public constants: cubic grid of length of `N` points (total $\mathtt{N}^3$ grid points) with grid size `h`.

The algorithm is organized according to steps described in § 4.6:

1. Assign masses of particles onto the grid.
2. Convolve the density with appropriate Green's function to get the mesh potential.
3. Differentiate the potential to get mesh forces.
4. Interpolate mesh forces back to particles.
5. Add the short-range part of the force to particles.

Mass Assignment

For mass assignment one uses a weighting scheme. In one dimension the weighting function of order `order` in a particle point `x` and a mesh point `y` is

```
double wgh_sch(double *x, int *y, int order){
 double dx, w = 1;

 switch (order){
 case 0: { // NGP: Nearest grid point
    for (int i = 0; i < 3; i++){
     if ((int)(x[i] + 0.5) % N != (y[i] + N) % N) w *= 0;
    }
    return w;
```

```
 }
 case 1: { // CIC: Cloud in cells
    for (int i = 0; i < 3; i++){
     dx = fmin(abs(x[i] - (y[i] + N) % N),x[i] + N - (y[i]
        + N) % N);
     if (dx > 1) w *= 0;
     else w *= 1 - dx;
    }
    return w;
 }
 case 2: { // TSC: Triangular shaped clouds
    for (int i = 0; i < 3; i++){
     dx = fmin(abs(x[i] - (y[i] + N) % N), x[i] + N - (y[i]
        + N) % N);
     if (dx > 1.5) w *= 0;
     else if (dx > 0.5) w *= (1.5 - dx)*(1.5 - dx) / 2.0;
     else w *= 3 / 4.0 - dx*dx;
    }
    return w;
 }
 }
}
```

For assigning values to or from the 3-D mesh we use

```
void assign_fc(double ***data, double *x, double &value,
   int order, bool asgn){
 switch (order){
 case 0: { // NGP: Nearest grid point, 1 cell involved
    if (asgn) data[(int)(x[0] + 0.5) % N][(int)(x[1] + 0.5)
       % N][(int)(x[2] + 0.5) % N] += value;
    else value += data[(int)(x[0] + 0.5) % N][(int)(x[1] +
       0.5) % N][(int)(x[2] + 0.5) % N];
    break;
 }
 default:{
    tVector_I y, z;
    for (int i = 0; i < 3; i++){
     z[i] = (int)(x[i] - 0.5*(order - 1));
    }
    for (y[0] = z[0]; y[0] < z[0] + 1 + order; y[0]++){
     for (y[1] = z[1]; y[1] < z[1] + 1 + order; y[1]++){
      for (y[2] = z[2]; y[2] < z[2] + 1 + order; y[2]++){
       if (asgn) data[(y[0] + N) % N][(y[1] + N) % N][(y[2]
          + N) % N] += value*wgh_sch(x, y, order);
       else value += data[(y[0] + N) % N][(y[1] + N) %
          N][(y[2] + N) % N] * wgh_sch(x, y, order);
      }
     }
    }
    break;
```

```
 }
 }
}
```

In case of `asgn = true` the `value` in point `x` is added to the mesh `data` – case when we assign a mass of a particle to the mesh. In case of `asgn = false`, on the contrary, the value stored on a grid is assign to the `value` in point `x` – case when interpolating forces from the mesh to particles. The mass assignment for all `p_num` particles is then done by the routine `add_density`

```
void add_density(double ***data, particle *particles, int
   order, int p_num, double mod){
 tVector_D x;
 double m;
 for (int p = 0; p < p_num; p++){
  x[0] = particles[p].x;
  x[1] = particles[p].y;
  x[2] = particles[p].z;
  m = mod*particles[p].mass;
  assign_fc(data, x, m, order, true);
 }
}
```

The modifier `mod` is simply 1 for classical N-body simulation with standard Green's function, but differs for the chameleon simulation while still using the same Green's function.

Potential calculation

For potential calculation we need an optimized Green's function. Here we present an algorithm for the Green's function optimized for the TSC weighting scheme, particles of $S_2(a)$ shape with the reference force

$$\hat{\boldsymbol{R}}(\boldsymbol{k}) = -\frac{i\boldsymbol{k}\hat{S}^2}{k^2+\lambda^2}, \tag{B.1}$$

and 4-point finite difference.

```
double green_fc(int i, int j, int k, double a, double
   pre_fc, double lambda_2){
 if (a == 0) return green_fc(i, j, k, pre_fc, lambda_2);
 if (((i*i + j*j + k*k)*4*PI*PI/(N*N) + lambda_2) == 0)
    return 0;
 else {
  const int n_max = 1;
  double U2 = 1, Gr = 0, D2 = 0;
  double U2_n, G_n, k2;
  tVector_D k3, D, R_n;
  k3[0] = 2 * PI / N*i;
  k3[1] = 2 * PI / N*j;
  k3[2] = 2 * PI / N*k;
```

```
  for (int n = 0; n < 3; n++){
   D[n] = 4 / 3.0*sin(k3[n]) - 1 / 6.0*sin(2 * k3[n]);
   D2 += D[n] * D[n];
   U2 *= 1 - pow(sin(k3[n] / 2), 2) + 2 * pow(sin(k3[n] /
      2), 4) / 15;
  }
  if (D2*U2*U2 == 0) return 0;
  for (int n1 = -n_max; n1 < n_max + 1; n1++){
   k3[0] = 2 * PI / N*i + 2 * PI*n1;
   for (int n2 = -n_max; n2 < n_max + 1; n2++){
    k3[1] = 2 * PI / N*j + 2 * PI*n2;
    for (int n3 = -n_max; n3 < n_max + 1; n3++){
     k3[2] = 2 * PI / N*k + 2 * PI*n3;
     k2 = k3[0] * k3[0] + k3[1] * k3[1] + k3[2] * k3[2];
     U2_n = 1;
     G_n = 0;
     for (int n = 0; n < 3; n++){
      if (k3[n] != 0) U2_n *= sin(k3[n] / 2) / (k3[n] / 2);
      R_n[n] = k3[n] * pow(S2_shape(sqrt(k2), a), 2) / (k2
         + lambda_2);
      G_n += D[n] * R_n[n];
     }
     Gr += G_n*pow(U2_n, 6);
    }
   }
  }

  return -pre_fc*Gr / (D2*U2*U2);
 }
}
```

Standard gravity is restored for `pre_fc` $= 4\pi G$ and `lambda_2` $= 0$. $S_2(a)$ shape in Fourier space is

```
double S2_shape(double k, double a){
 double t = k*a / 2;
 return 12 / pow(t, 4)*(2 - 2 * cos(t) - t*sin(t));
}
```

Note that evaluation of the Green's function is performed only once in whole simulation. The convolution of the Green's function with density is than rather straightforward

```
void slvPoisson(double ***data, double *t, int *ip, double
   *w, double ***green){
 rdft3d(N, N, N, 1, data, t, ip, w);
 rdft3dsort(N, N, N, 1, data);

 double g;
 for (int i = 0; i < N; i++){
  for (int j = 0; j < N; j++){
```

```
   for (int k = 0; k <= N/2 ; k++){
    g = green[i][j][k] * 2 / (N*N*N);
    // Green's function and normalization in case of IRDFT
    data[i][j][2*k] *= g;
    // Real part of the potential in Fourier space
    data[i][j][2 * k+1] *= g;
    // Imaginary part
   }
  }
 }
 rdft3dsort(N, N, N, -1, data);
 rdft3d(N, N, N, -1, data, t, ip, w);
}
```

Routines `rdft3d` and `rdft3dsort` are from the library `fftsg3d.c`. Arrays `t, ip` and `w` are working space for the routine `rdft3d`.

The finite differentiation of the potential to get forces and then interpolating them back to particle positions using the routine `assign_fc` is simple and straightforward so we will not present these parts here.

Short-range Force

In order to efficiently treat nearby particles a chain mesh with *linked-list* is created. The 3-D integer chain mesh `HOC` has `M` grid points with grid size `Hc` $> r_c$. The linked-list is an integer array `[0..p_num]`. Particles are numbered in the same fashion. i.e. `0..p_num`. The idea with the chain mesh is following: If the chain cell contains no particles, assign it value -1. If it contains some particles, assign it value of the last particle. The linked-list then points to the next particle in the cell, that one points to another, etc. until one hits -1. When evaluating the short-range force one goes through the 27 chain cells and quickly finds every particle.

```
void get_LL(int ***HOC, int *LL, particle *particles, int
   M, double Hc, int p_num){
 for (int i = 0; i < M; i++){
  for (int j = 0; j < M; j++){
   for (int k = 0; k < M; k++){
    HOC[i][j][k] = -1;
   }
  }
 }
 int x,y,z;
 for (int i = 0; i < p_num; i++){
  x = (int)(particles[i].x / Hc);
  y = (int)(particles[i].y / Hc);
  z = (int)(particles[i].z / Hc);
  LL[i] = HOC[x][y][z];
  HOC[x][y][z] = i;
 }
}
```

```
void force_short(particle *particles, int ***HOC, int *LL,
   double *x, double *f, double Hc, double rc, double a,
   int M){
 // Calculate short range force in point x, force is added
    to vector *f
 int p;
 double dr;
 for (int i = (int)(x[0] / Hc) - 1; i < (int)(x[0] / Hc) +
    2; i++){
  for (int j = (int)(x[1] / Hc) - 1; j < (int)(x[1] / Hc) +
     2; j++){
   for (int k = (int)(x[2] / Hc) - 1; k < (int)(x[2] / Hc)
      + 2; k++){
    p = HOC[(i + M) % M][(j + M) % M][(k + M) % M];
    while (p != -1){
     dr = dst(particles[p], x);
     if (dr < rc){ // Short range force is set 0 for
        separation larger than rc
      f[0] += particles[p].mass* G*(force_tot(dr) -
         force_ref(dr, a))*dst_per(particles[p].x, x[0]) /
         dr;
      f[1] += particles[p].mass*G*(force_tot(dr) -
         force_ref(dr, a))*dst_per(particles[p].y, x[1]) /
         dr;
      f[2] += particles[p].mass*G*(force_tot(dr) -
         force_ref(dr, a))*dst_per(particles[p].z, x[2]) /
         dr;
     }
     p = LL[p];
    }
   }
  }
 }
}
```

Auxiliary functions `dst` and `dst_per` simply return the distance (with periodicity included). The `force_tot` is desired total force and `force_ref` is the reference (mesh) force. For $S_2(a)$ shape particle

```
double force_ref(double r, double a){
 double z = 2 * r / a;
 if (z > 2) return 1 / (r*r);
 else if (z > 1) return (12 / (z*z) - 224 + 896 * z - 840 *
    z*z + 224 * pow(z, 3) + 70 * pow(z, 4) - 48 * pow(z, 5)
    + 7 * pow(z, 6)) / (35 * a*a);
 else return (224 * z - 224 * pow(z, 3) + 70 * pow(z, 4) +
    48 * pow(z, 5) - 21 * pow(z, 7)) / (35 * a*a);
}
```

Bibliography

[1] Abate, A., et al. (LSST Dark Energy Science Collaboration) *Large Synoptic Survey Telescope: Dark Energy Science Collaboration.* eprint arXiv:1211.0310v1 (2012)

[2] Abbott, T., et al. (DES Collaboration) *The Dark Energy Survey.* eprint arXiv:astro-ph/0510346v1 (2005)

[3] Ade, P., et al. (Planck Collaboration) *Planck 2015 results. XIII. Cosmological parameters.* eprint arXiv:1502.01589v2 (2015)

[4] Amanullah, R., et al. (Supernova Cosmology Project) *Spectra and Light Curves of Six Type Ia Supernovae at 0.511 < z < 1.12 and the Union2 Compilation.* eprint arXiv:1004.1711v1 (2010)

[5] Alnes, H., Amarzguioui, M. *CMB Anisotropies Seen by an off-center Observer in a Spherically Symmetric Inhomogeneous Universe.* eprint arXiv:astro-ph/0607334 (2006)

[6] Alnes, H., et al. *An Inhomogeneous Alternative to Dark Energy?.* eprint arXiv:astro-ph/0512006 (2005)

[7] Amendola, L. *Coupled Quintessence.* eprint arXiv:astro-ph/9908023 (1999)

[8] Amendola, L., et al. *Are $f(R)$Dark Energy Models Cosmologically Viable?.* eprint arXiv:astro-ph/0603703 (2006)

[9] Amendola, L., et al. *Conditions for the Cosmological Viability of $f(R)$Dark Energy Models.* eprint arXiv:gr-qc/0612180 (2006)

[10] Amendola, L., Quercellini, C. *Tracking and Coupled Dark Energy as Seen by the Wilkinson Microwave Anisotropy Probe.* Phys. Rev. D, 68, 023514 (2003)

[11] Amendola, L., Tsujikawa, S. *Dark Energy – Theory and Observations.* Cambridge University Press (2010), New York

[12] Anselmi, A. *Euclids Assesment Study – Executive Summary.* Thales Alenia Space. (2009)

[13] Armendariz-Picon, C., et al. *k-Inflation.* eprint arXiv:hep-th/9904075 (2008)

[14] Aubourg, E., et al. (BOSS Collaboration) *Cosmological Implications of Baryon Acoustic Oscillation (BAO) Measurements.* eprint arXiv:1411.1074v2 (2014)

[15] Babichev, E., Deffayet, C. *An introduction to the Vainshtein mechanism.* eprint arXiv:1304.7240 (2013)

[16] Barden, S., et al. *Gemini WFMOS Feasibility Study Report.* `http://www.gemini.edu/files/docman/science/aspen/WFMOS_feasibility_report_public.pdf` (2005)

[17] Barnes, J., Hut, P. *A Hierarchical $O(NlogN)$ Force-calculation Algorithm.* Nature 324, 446 – 449 (1986)

[18] Bartelmann, M., Schneider, P. *Weak Gravitational Lensing.* eprint arXiv:astro-ph/9912508v1 (1999)

[19] Bertotti, B., et al. *A Test of General Relativity Using Radio Links with the Cassini Spacecraft.*. Nature 425, 374 – 376 (2003)

[20] Bertschinger, E. *One Gravitational Potential or Two?Forecasts and Tests.* eprint arXiv:1111.4659 (2011)

[21] Binetruy, P. *Models of Dynamical Supersymmetry Breaking and Quintessence.* eprint arXiv:hep-ph/9810553 (1998)

[22] Binney, J., Tremaine, S. *Galactic Dynamics.* Princeton University Press (1994), Princeton

[23] Brandt, A. *Multi-level Adaptive Solutions to Boundary-value Problems.* IEEE Antennas Propag. Mag. 35, 7 – 12(1993)

[24] Brans, C., Dicke, R. *Mach's Principle and a Relativistic Theory of Gravitation.* Math. Comp. 31, 333 – 390 (1977)

[25] Brax, P., et al. *Nonlinear Structure Formation with the Environmentally Dependent Dilaton.* eprint arXiv:1102.3692 (2011)

[26] Brax, P., Martin, J. *Quintessence and Supergravity.* eprint arXiv:astro-ph/9905040 (1999)

[27] Caldwell, R., et al. *Cosmological Imprint of an Energy Component with General Equation of State.* Phys. Rev. Lett. 80, 1582 – 1585 (1998)

[28] Caldwell, R., Linder, E. *The Limits of Quintessence.* eprint arXiv:astro-ph/0505494 (2005)

[29] Capozziello, S., et al. *Gauss-Bonnet Dark Energy by Lagrange Multipliers.* eprint arXiv:1302.0093 (2013)

[30] Capozziello, S., Laurentis, M. *Extended Theories of Gravity.* eprint arXiv:1108.6266 (2011)

[31] Carloni, S., et al. *Conformal Transformations in Cosmology of Modified Gravity: the Covariant Approach Perspective.* eprint arXiv:0907.3941 (2009)

[32] Carroll, S. *Spacetime and geometry. An introduction to general relativity.* Pearson Education, Inc. (2004), San Francisco

[33] Carroll, S., et al. *The Cosmology of Generalized Modified Gravity Models.* eprint arXiv:astro-ph/0410031 (2004)

[34] Cervantes-Cota, J.,Smoot, G. *Cosmology today – A brief review.* eprint arXiv:1107.1789v2 (2011)

[35] Chang, C., et al. *Wide-Field Lensing Mass Maps from DES Science Verification Data.* eprint arXiv:1505.01871v1 (2015)

[36] Chernoff, D., Tye, H. *Inflation, string theory and cosmic strings.* eprint arXiv:1412.0579 (2015)

[37] Clarkson, C., Regis, M. *The Cosmic Microwave Background in an Inhomogeneous Universe.* eprint arXiv:1007.3443 (2010)

[38] Coifman, R., et al. *The Fast Multipole Method for the Wave Equation: A Pedestrian Prescription.* IEEE Antennas Propag. Mag. 35, 7 – 12(1993)

[39] Damour, T., Polyakov, A. *The String Dilaton and a Least Coupling Principle.* eprint arXiv:hep-th/9401069 (1994)

[40] *Dark Energy Science Collaboration* [online]. [cited 28/06/2015]. <`http://www.lsst-desc.org/`>

[41] Dawson, K., et al. (BOSS Collaboration) *The Baryon Oscillation Spectroscopic Survey of SDSS-III.* eprint arXiv:1208.0022v3 (2012)

[42] Dehnen, W., Read, J. *N-body simulations of Gravitational Dynamics.* eprint arXiv:1105.1082v1 (2011)

[43] Dutta, S., Scherrer, R. *Hilltop Quintessence.* eprint arXiv:0809.4441 (2008)

[44] Dvali, G., et al. *4D Gravity on a Brane in 5D Minkowski Space.* eprint arXiv:hep-th/0005016 (2000)

[45] Efstathiou, G., et al. *Numerical Techniques for Large Cosmological N-body Simulations.* ApJS 57, 241 – 260 (1985)

[46] Ellis, G., et al. *Relativistic Cosmology.* Cambridge University Press (2012), Cambridge

[47] *European Space Agency - Euclid* [online]. [cited 18/03/2015]. <`http://sci.esa.int/euclid/`>

[48] *European Space Agency - Gaia* [online]. [cited 07/07/2015]. <`http://sci.esa.int/gaia/`>

[49] *European Space Agency - Planck* [online]. [cited 30/06/2015]. <`http://sci.esa.int/planck/`>

[50] Ewald, P. *Die Berechnung optischer und elektrostatischer Gitterpotentiale.* AnP 369, 253 – 287 (1921)

[51] Faraoni, V., et al. *Conformal Transformations in Classical Gravitational Theories and in Cosmology.* eprint arXiv:gr-qc/9811047 (1998)

[52] Faraoni, V., Gunzig, E. *Einstein frame or Jordan frame?*. eprint arXiv:astro-ph/9910176 (1999)

[53] Felice, A., et al. *Ghosts, Instabilities, and Superluminal Propagation in Modified Gravity Models*. eprint arXiv:astro-ph/0604154 (2006)

[54] Fierz, M., Pauli, W. *On Relativistic Wave Equations for Particles of Arbitrary Spin in an Electromagnetic Field,*. Proc. Roy. Soc. Lond. A173, 211 -– 232 (1939)

[55] Frieman, J., et al. *Cosmology with Ultra-light Pseudo-Nambu-Goldstone Bosons*. Phys. Rev. Lett. 75, 2077 – 2080 (1995)

[56] Gasperini, M., Veneziano, G. *The Pre-Big Bang Scenario in String Cosmology*. eprint arXiv:hep-th/0207130 (2002)

[57] Gonzalo, O. *Post-Newtonian Constraints on $f(R)$Cosmologies in Palatini Formalism*. eprint arXiv:gr-qc/0505136 (2005)

[58] Filippenko, A. *Optical Spectra of Supernovae*. ARA&A., 35, 309 – 355 (1997)

[59] *Hobby-Eberly Telescope Dark Energy Experiment* [online]. [cited 30/06/2015]. <`http://sci.esa.int/euclid/`>

[60] Hernquist, L., et al. *Application of the Ewald method to cosmological N-body simulations*. ApJS 75, 231 – 240 (1991)

[61] Hinshaw, G., et al. *Nine-Year Wilkinson Microwave Anisotropy Probe (WMAP) Observations: Cosmological Parameter Results*. eprint arXiv:1212.5226v3 (2013)

[62] Hinterbichler, K. *Theoretical Aspects of Massive Gravity*. eprint arXiv:1105.3735 (2011)

[63] Hinterbichler, K., Khoury, J. *Symmetron Fields: Screening Long-Range Forces Through Local Symmetry Restoration*. eprint arXiv:1001.4525 (2010)

[64] Hockney, R., Eastwood, J. *Computer Simulation Using Particles*. Adam Hilger, Bristol and New York (1989), New York

[65] Horndeski, G. *Second-order scalar-tensor field equations in a four-dimensional space*. Int. J. Theor. Phys. 10, 363 – 384 (1974)

[66] Hu, W., Sawicki, I. *Models of $f(R)$Cosmic Acceleration that Evade Solar-System Tests*. eprint arXiv:0705.1158 (2007)

[67] Gott, III, R., et al. *An unbound universe?*. ApJ 194, 543 – 553 (1974)

[68] Ivezic, Z., et al. (LSST Science Collaboration) *Science Requirements Document*. LPM-17, (2011)

[69] Ivezic, Z., et al. (LSST Science Collaboration) *LSST: from Science Drivers to Reference Design and Anticipated Data Products*. eprint arXiv:0805.2366v4 (2014)

[70] Jain, B., et al. *Novel Probes of Gravity and Dark Energy*. eprint arXiv:1309.5389v2 (2013)

[71] Joyce, A., et al. *Beyond the Cosmological Standard Model*. eprint arXiv:1407.0059 (2014)

[72] Jullo, E., et al. *Cosmological Constraints from Strong Gravitational Lensing in Galaxy Clusters*. eprint arXiv:1008.4802 (2010)

[73] Kamenshchik, A., Moschella, U., Pasquier, V. *An Alternative to Quintessence*. eprint arXiv:gr-qc/0103004 (2001)

[74] Kessler, R., et al. *First-year Sloan Digital Sky Survey-II (SDSS-II) Supernova Results: Hubble Diagram and Cosmological Parameters*. eprint arXiv:0908.4274v1 (2009)

[75] Laureijs, R., et al. *Euclid Definition Study Report*. eprint arXiv:1110.3193v1 (2011)

[76] Lidsey, J., et al. *Superstring Cosmology*. eprint arXiv:hep-th/9909061 (1999)

[77] LSST Science Collaborations. *LSST Science book*. LSST Corporation (2009), Tuscon

[78] *Large Synoptic Survey Telescope* [online]. [cited 28/06/2015]. <`http://www.lsst.org/lsst/`>

[79] Magnanano, G., Sokolowski, L. *On Physical Equivalence between Nonlinear Gravity Theories*. eprint arXiv:gr-qc/9312008 (1993)

[80] Martineau, P., Brandenberger, R. *The Effects of Gravitational Back-Reaction on Cosmological Perturbations*. eprint arXiv:astro-ph/0505236 (2005)

[81] Mota, D., Shaw, D. *Evading Equivalence Principle Violations, Cosmological, and Other Experimental Constraints in Scalar Field Theories with a Strong Coupling to Matter*. Phys. Rev. D, 75, 063501 (2007)

[82] Moyassari, P., Setare, M. *Quintom Dark Energy in DGP Braneworld Cosmology*. eprint arXiv:0806.2418 (2008)

[83] Muller, V., et al. *The stability of the de Sitter Space-Time in Fourth Order Gravity*. Phys. Lett. B 202, 198 – 200 (1988)

[84] Navarro, J., et al. *The Structure of Cold Dark Matter Halos*. eprint arXiv:astro-ph/9508025v1 (1996)

[85] Neupane, I., Carter, B. *Towards Inflation and Dark Energy Cosmologies from Modified Gauss-Bonnet Theory*. eprint arXiv:hep-th/0512262 (2005)

[86] Nicolis A., et al. *The Galileon as a Local Modification of Gravity.* eprint arXiv:0811.2197 (2008)

[87] Nishizawa, A. *Integrated Sachs Wolfe Effect and Rees Sciama Effect.* eprint arXiv:1404.5102v1 (2014)

[88] Nojiri, S., et al. *Gauss-Bonnet Dark Energy.* eprint arXiv:hep-th/0504052 (2005)

[89] Ooura, T. *Fast Fourier/Cosine/Sine Transform Packages.* `http://www.kurims.kyoto-u.ac.jp/~ooura/fft.html` (2006)

[90] *Pan-STARRS* [online]. [cited 07/07/2015]. <`http://pan-starrs.ifa.hawaii.edu/`>

[91] Peebles, P. *The Large-scale Structure of the Universe.* Princeton University Press (1980), Princeton

[92] Phillips, M. *The absolute magnitudes of Type IA supernovae.* ApJ., 413, L105–L108 (1993)

[93] Piazza, F., Tsujikawa, S. *Dilatonic Ghost Condensate as Dark Energy.* eprint arXiv:hep-th/0405054 (2004)

[94] Postma, M., Volponi, M. *Equivalence of the Einstein and Jordan Frames.* eprint arXiv:1407.6874 (2014)

[95] Press, W., et al. *Numerical Recipes.* Cambridge University Press (2007), New York

[96] Putter, R., et al. *Testing LTB Void Models Without the Cosmic Microwave Background or Large Scale Structure: New Constraints from Galaxy Ages.* eprint arXiv:1208.4534 (2012)

[97] Rasanen, S. *Dark Energy from Backreaction.* eprint arXiv:astro-ph/0311257 (2004)

[98] Refregier, A., et al. (Euclid Imaging Consortium) *Euclid Imaging Consortium Science Book.* eprint arXiv:1001.0061v1 (2010)

[99] Riess, A., et al. *Observational Evidence from Supernovae for an Accelerating Universe and a Cosmological Constant.* AJ., 116, 1009 – 1038 (1998)

[100] Sandvik, H., et al. *The End of Unified Dark Matter?.* eprint arXiv:astro-ph/0212114 (2002)

[101] Schwab, J., et al. *Galaxy-Scale Strong Lensing Tests of Gravity and Geometric Cosmology: Constraints and Systematic Limitations.* eprint arXiv:0907.4992v2 (2009)

[102] Seo, H.-J., Eisenstein, D. *Improved Forecasts for the Baryon Acoustic Oscillations and Cosmological Distance Scale.* eprint arXiv:astro-ph/0701079v1 (2007)

[103] *Research School of Astronomy & Astrophysics - SkyMapper* [online]. [cited 07/07/2015]. <http://rsaa.anu.edu.au/observatories/telescopes/skymapper-telescope>

[104] *Sloan Digital Sky Survey* [online]. [cited 30/06/2015]. <http://www.sdss.org/>

[105] Song, Y., et al. *The Large Scale Structure of $f(R)$Gravity.* eprint arXiv:astro-ph/0610532 (2007)

[106] Spergel, D., et al. (Science Definition Team and WFIRST Study Office) *Wide-Field InfrarRed Survey Telescope-Astrophysics Focused Telescope Assets WFIRST-AFTA 2015 Report.* eprint arXiv:1503.03757v2 (2015)

[107] Sussman, R. *Back-reaction and Effective Acceleration in Generic LTB Dust Models.* eprint arXiv:1102.2663 (2011)

[108] Tamaki, T., Tsujikawa, S. *Revisiting Chameleon Gravity – Thin-shells and No-shells with Appropriate Boundary Conditions.* eprint arXiv:0808.2284 (2008)

[109] Tancred, L. *N-body algorithms.* Seminar presentation, http://www.cs.hut.fi/~ctl/NBody.pdf (1999)

[110] Tsujikawa, S. *Matter Density Perturbations and Effective Gravitational Constant in Modified Gravity Models of Dark Energy.* eprint arXiv:0705.1032 (2007)

[111] Tsujikawa, S. *Observational Signatures of $f(R)$Dark Energy Models that Satisfy Cosmological and Local Gravity Constraints.* eprint arXiv:0709.1391 (2007)

[112] Upadhye, A. *Dark Energy Fifth Forces in Torsion Pendulum Experiments.* eprint arXiv:1209.0211 (2012)

[113] Upadhye, A. *Notes – $f(R)$ Gravity in the Einstein Frame.* Unpublished (2012)

[114] Upadhye, A., Steffen, J. *Monopole Radiation in Modified Gravity.* eprint arXiv:1306.6113 (2013)

[115] *Wide-Field Infrared Survey Telescope* [online]. [cited 28/06/2015]. <http://wfirst.gsfc.nasa.gov/>

[116] Yoo, J., Watanabe, Y. *Theoretical Models of Dark Energy.* eprint arXiv:1212.4726 (2012)

[117] Vainshtein, A. *To the Problem of Nonvanishing Gravitation Mass.* Phys. Lett. B 39, 393 – 394 (1972)

[118] Waterhouse, T. *An Introduction to Chameleon Gravity.* eprint arXiv:astro-ph/0611816 (2006)

[119] Weinberg, D., et al. *Observational Probes of Cosmic Acceleration.* eprint arXiv:1201.2434v2 (2013)

[120] Weinberg, S. *Gravitation and Cosmology: Principles and Application of the General Theory of Relativity.* John Willey & Sons, Inc. (1972), New York

[121] White, S., et al. *The Amplitude of mass fluctuations in the universe.* MNRAS, 262, 1023 – 1028 (1993)

[122] *Wilkinson Microwave Anisotropy Probe* [online]. [cited 30/06/2015]. <http://map.gsfc.nasa.gov/>

[123] Woodard, R. *Avoiding Dark Energy with 1/R Modifications of Gravity.* Lect. Notes Phys., 720, 403 – 433 (2007)

[124] Zlatev, I., et al. *Quintessence, Cosmic Coincidence, and the Cosmological Constant.* eprint arXiv:astro-ph/9807002 (1998)

[125] Zwicky, F. *Die Rotverschiebung von extragalaktischen Nebeln.* Helvetica Physica Acta 6, 110 – 127 (1933)